UiO : Institute of Theoretical Astrophysics
University of Oslo

Being a Bat in Space

Measuring Distances Inside Active Galactic Nuclei Using Reverberation Mapping

Natalia Eiré Sommer

Master's Thesis

Spring 2016

Acknowledgements

There are many people who deserve an acknowledgement as I am writing my thesis. Naming them all would be difficult, and stating why and how they have had an impact on my life – both privately and professionally – would require a number of pages which would start approaching the number of pages of my thesis. I would, however, like to extend a special thank-you to a few of them.

First of all, I would like to thank my primary supervisor, Tamara M. Davis. You are such an inspiration in so many different ways. Although space has fascinated me for about as long as I can remember, you were the one who inspired me to follow that dream. As a child, adults often ask them what they want to be when they grow up. When starting university, I did not know what my answer for that question would be anymore. However, after meeting you, the answer was crystal clear; "I want to become someone like Tamara". You are so intelligent, so passionate, so full of life, and although I cannot fathom how you manage to do it all, you are such a real person, human being. You look out to the end of the universe, and yet you manage to be present in even the smallest of my problems on this speck of dust called Earth. I cannot thank you enough for being you. You are awesome.

I want to thank Anthea L. King for all the help she has provided me with. I started constantly knocking on your door while you were still in the process of finishing off your PhD, and when you moved away to start your PostDoc, I continued asking you for help. You gave me some code to use for my project, so I didn't have to start from scratch, you helped me understand the physics behind the AGN we both have been working on, and you have helped me with everything in between. Thank you for that.

Another thank-you should be given to Paul Martini. You have been available when I needed you, discussed my problems when I have gotten stuck, and helped deciding in which direction my major steps should be taken. Getting your feedback has been very valuable, especially when you have put focus on things the rest of us did not consider.

Signe Riemer-Sørensen, my Danish supervisor in Norway, you have fascinated me from the very start. Meeting you in Sydney for the very first time was almost surreal. Not only was the meeting almost completely random, but it also gave me an idea about what it is like in academia; you simply have to jump into things, make contact, take chances and create opportunities. Thank you for taking me on as your student. I can only say I am happy I decided to chose you to be my supervisor, and I am grateful for the time you have invested in me. You have shown me how I can do just about anything, provided I at least give it a go.

I would like to thank Sarah L. Thomson, Carolyn E. Wood and Iulia Popa-Mateiu for supporting me so much this year. I do not know how many times I have broken down, how

many anxiety attacks I have had, how many times things which only existed inside my head got a hold of me to a point where I was not even in control over my own body. You guys have been there through all of it. You have been patient, kind, and you have done just the right things at the right times. I cannot imagine going through this year without you.

I also find it necessary to give a shout out to one of my former lecturers, Hans Kristian K. Eriksen. The one course I did with you gave me incredibly much, and I am grateful for all the times I could pop by your office to ask for help, in relation to my projects as well as about personal matters. I was always fascinated by your teaching, and your talking about your work. You clearly have a strong passion for it, and I can only hope to one time become as cool as you are.

Finally, I would like to thank all the amazing academics I have interacted with this year, who in many ways have helped me reach my goal. Feeling small and unimportant I sent some of you emails, and asked you questions. You responded, treated me like an equal, and invested time in me, barely even knowing my name. Some other I have visited, or have had visit me, and you have sat next to me as I have been trying to swallow my nervousness, complete my sentences, and explain the messy plots on my computer screen. You have been available for me to bounce ideas off you, helped me think, and corrected me in my misunderstandings. Thank you for helping out a struggling Master's student, and for seeing the aspiring astrophysicist.

Abstract

Active galactic nuclei (AGN) are the extremely luminous hearts of a subset of galaxies we call active galaxies. It is commonly accepted that they contain supermassive black holes (SMBHs) at their centres, surrounded by a luminous accretion disk and extended gas regions at various radii from the black hole. One such region is the broad-line region (BLR), which contains high velocity clouds that produce the Doppler shifted emission lines. In this Thesis we present new developments in the field of studying AGN with a method called reverberation mapping. Reverberation mapping compares the variations in the accretion disk flux with the variations in the line flux of certain lines of the BLR, allowing to find an AGN's BLR size; the distance between a SMBH and its BLR.

We simulate light curves for the central regions of AGN based on measurements we expect to obtain from the photometric Dark Energy Survey (DES), and the Australian spectroscopic counterpart, OzDES, to predict how well we can perform the reverberation mapping analysis using this dataset. We use a Markov Chain Monte Carlo (MCMC) based software (JAVELIN; Zu, Kochanek & Peterson, 2011) to obtain estimates for these distances, and test reliability when the emission line responds to changes in the accretion disk flux in a different way than that expected by the program. We find that JAVELIN reliably recovers the BLR size regardless of the inferred emission line response. This is important, as the true emission line response is unknown.

It has been observed that AGN with similar luminosities tend to recover similar BLR sizes, which is consistent with theoretical predictions. We take advantage of this behaviour, and use the output from JAVELIN in a Bayesian stacking analysis in order to obtain BLR size estimates for groups of AGN whose individual BLR size recoveries are not reliable. We find that the Bayesian stacking method is a more precise and accurate way of estimating the BLR size when compared to BLR size estimates from individual objects. In order to apply this method to the real survey and optimise the binning of the AGN into groups of similar luminosity, we simulated AGN with redshift and absolute magnitude distributions consistent with the DES/OzDES sample. We then apply the stacking analysis on simulated Mg II light curves to find the optimal grouping of the sample. We find that approximately 95% of the AGN where Mg II can be used for reverberation mapping can contribute to obtaining time lag estimates for AGN when using stacking.

Contents

List of Figures

Glossary

AGN Active Galactic Nucleus, or Active Galactic Nuclei.
An actively accreting supermassive black hole at the heart of a galaxy, resulting in characteristic qualities for the galaxy.

BH Black hole.
A celestial object whose escape velocity exceeds the speed of lights.

BLR Broad-line region.
Area around supermassive black hole in active galactic nuclei where gas clouds are distant enough not to be fully ionised, but close enough to be strongly influenced by the gravitational pull of the black hole, resulting in broad emission lines in the spectrum.

C IV Carbon IV λ1549 Å.

damped random walk A random walk whose step size is "damped" according to its distance from a given value, such that the variations do not deviate far from this value.

DES Dark Energy Survey.
Five year (plus a zeroth science verification year) long photometric survey monitoring for instance supernovae and active galactic nuclei.

`emcee` "The MCMC Hammer".
A variation of Markov chain Monte Carlo algorithms implemented in Python. It is used in the reverberation mapping software JAVELIN.

Hβ Hydrogen beta λ4861 Å.

JAVELIN Just Another Vehicle for Estimating Lags In Nuclei.
`emcee` Markov chain Monte Carlo based software developed for determining lags between the continuum source and the broad-line emission region in active galactic nuclei.

MCMC Markov chain Monte Carlo.
Algorithm originating from the field of Bayesian statistics, used for sampling from an unknown probability distribution.

Mg II Magnesium II λ2798 Å.

NLR Narrow line region.
Area around supermassive black hole in active galactic nuclei where gas clouds are partially ionised, and distant enough for Doppler broadening not to affect the emission lines significantly.

OzDES Australian Dark Energy Survey, or Optical redshifts for the Dark Energy Survey.
Six year long spectroscopic survey, complementing the Dark Energy Survey. Monitors for instance supernovae and active galactic nuclei.

Pan-STARRS1 Panoramic Survey Telescope & Rapid Response System 1.
A wide-field imaging facility primarily used for searching for moving objects over a large area of the sky, but is also used for a variety of deep-sky investigations..

QSO Quasi-stellar object.
Active galactic nuclei where the remaining galaxy is not visible due to the large distance to the object. The radio source may or may not be strong for these objects. Another commonly used term, "quasar", technically refers only to radio loud QSOs, but the term is often used interchangeably with QSO, and AGN in general.

$R - L$ **relationship** Radius-luminosity relationship.
Relationship between the broad-line region radius and luminosity for active galactic nuclei. Expected to follow $R \propto \sqrt{L}$ from theory.

RM Reverberation mapping.
Technique where the variation in accretion disk and and broad-line region emission line flux for an active black hole are compared to determine the distance between the accretion disk and the broad-line region.

SDSS-RM Sloan Digital Sky Survey Reverberation Mapping.
Reverberation mapping project conducted by the Sloan Digital Sky Survey, targeting 849 active galactic nuclei with redshifts $0.1 < z < 4.5$.

SMBH Supermassive black hole.
A black hole with mass of a million or more times the mass of a stellar black hole.

transfer function Function used to describe the emission line response to, or the smoothing impact of the broad-line region on, the continuum emission. The emission line light curve is given by a convolution of the continuum light curve with the transfer function.

UV Ultra violet 1000 Å $< \lambda <$ 4000 Å.

To Nate.
You made me happy.

1 Introduction

Active galactic nuclei (AGN) are the central, extremely luminous parts of active galaxies. According to the unified model, AGN have a supermassive black hole at their centre. The black hole is surrounded by a luminous accretion disk, which is the cause of the extreme luminosity of the AGN. At a certain distance outside the accretion disk is the broad-line region (BLR), which contains partially ionised gas. The neutral BLR gas is photoionised by the light emitted by the AGN accretion disk, after which the electrons are recaptured by the atoms, and emit the charachteristic emission line light when cascading down the energy levels of the atoms. When the continuum light originating at the accretion disk changes over time, similar changes can be observed coming from the BLR, only delayed by the travel time needed for light to reach these areas. By measuring the delay between the continuum and BLR emission we use a method akin to that used by bats for navigation; namely translating time into distance by a known speed. This method, named reverberation mapping, has been used for decades to learn more about the innermost regions around supermassive black holes (SMBHs), which cannot be resolved visually. Kaspi et al. (2000), and, more recently, Bentz et al. (2013), showed that the size of the BLR and the luminosity of AGN seem to follow a trend, suggesting that the luminosity of AGN may be inferred from properties other than the observed flux, which again opens up for the possibility of using AGN as standard candles (Watson et al., 2011). This would be excellent, because AGN are persistently luminous, in contrast to different standard candles, namely type Ia supernovae. The luminosity of AGN is also much larger than any other standard candle currently in use, something which would allow to probe the Universe at distances much greater than ever before. This opens up for the possibility of investigating how cosmological parameters have changed over time, which would teach us more about the evolution of the Universe as a whole, and consequently about its contents, and our theory of gravity.

Reverberation mapping calls for a comparison of the light curves originating very close to the SMBH and in the BLR. Assuming that the BLR light curve is a kind of echo of the light

curve originating closer to the SMBH, measuring the time lag between the signals allows us to find the distance between a SMBH and its BLR. Learning about such a property of AGN is interesting, not only because it allows us to study central parts of AGN close to the black holes, but also because it teaches us about black hole evolution, the role of black holes in galaxy evolution, and even about the history of our Universe. While the reverberation mapping field has existed for several decades, the progress has been somewhat slow, partly due to the long observation time needed to collect data for reverberation mapping purposes. Individual estimates of AGN lags can also be noisy and unreliable. We have made use of already existing software and theory to further develop a more effective method of estimating the lags of AGN. As we expect AGN of similar luminosities to have similar lags, we expect that it is possible to stack the individual lag estimates for similar AGN to obtain one clearer time lag estimate for the group as a whole. We find that by stacking individual estimates of AGN time lags a larger fraction of observational data may be used for successful time lag estimation. This will allow us to extract lag information from AGN whose individual reverberation mapping results would be inconclusive, and to obtain physical information about AGN at earlier stages in observational surveys.

In the rest of this Chapter we provide the necessary knowledge about AGN, reverberation mapping, standard candles, and the DES/OzDES surveys, which provide necessary data for our research, before outlining the remainder of the Thesis. For more information about AGN and the lowest steps of the cosmic distance ladder, please refer to Ryden & Peterson (2010) and Peterson (1997).

1.1 The Cosmic Distance Ladder & Standard Candles

Being able to measure distances in space is crucial for learning about our Universe. The measuring tools we use on Earth become useless when considering the great distances in the universe, making it necessary to find alternative methods. In order to determine distances to objects outside the solar system, we are required to be creative, sometimes even making use of basic geometry. Several methods have been developed, but each method is generally only practical for a small range of distances, and has to be calibrated to another method. This forces us to create the so-called cosmic distance ladder, in which each measurement method is a "step" on the ladder, and is required to get to the next "step". The term distance ladder may be somewhat misleading, as there often are more than one type of measurement available for determining distances of a given scale, however, a calibration between given methods is always necessary, especially when moving into new distance scales.

The way we measure distances is not the only thing in need of a change when moving to celestial scales. At some point, metres and kilometres also become meaningless, and we start stating differences in terms of far larger units. One example of this is the light year, a very intuitive distance measure, given the constant speed of light. Its constancy implies that light will always travel an equal amount of space during a given amount of time. A light year is the distance covered by a photon over a period of a year. Some simple maths leads to finding that a light year equals to $9.46 \cdot 10^{12}$ km, a distance corresponding to travelling around the Earth just above 236 million times. Such a long distance is somewhat difficult to grasp on Earth, yet it is not particularly significant in the grand scheme of things. Indeed,

when moving to celestial distances we quickly realise that time measurement ambiguity also arises. To combat this we tend to not describe distances to objects directly, but relate these properties to an object's relative line-of-sight velocity with respect to us.

Doppler (1843) showed that waves are affected when the observer or source emitting the observer are in motion relative to each other (see Eden, 1992, for English translation), an effect we now refer to as the Doppler effect. In his derivation, Doppler showed that the frequency of a wave emitted by a moving object will change when observed by a stationary observer, depending on the relative velocity between them. If the observer and emitter are moving towards each other, the waves will be "compressed", resulting in a higher frequency, and for motion away from each other, the waves are "stretched", resulting in lower frequency. For light, this implies that light is shifted towards the blue side of the electromagnetic spectrum if the observer and source are getting closer, and towards the red side if the motion is away from each other. This led to the terms blueshift and redshift, respectively. The blueshift or redshift of celestial objects are possible to measure, provided a spectroscopic observation can be made. The redshift z of any object is given (Ryden & Peterson, 2010, Eq. 23.61) by

$$z = \frac{\lambda_0 - \lambda_e}{\lambda_e}, \tag{1.1}$$

where λ_0 is the wavelength observed, and λ_e is the emitted wavelength. This has proven to be very helpful, because the expansion of the universe implies the stretching of waves as light travels through it. The longer a photon travels through the universe, the more stretched the waves become, allowing us to use redshift as a distance indicator – and, through the speed of light, a time indicator.

One of the first steps of the cosmic distance ladder is parallax, and this technique has been used since the time of the ancient Greeks. It utilises geometrical arguments for determining the distance to an object, provided an object can be perceived as moving relative to a fixed background when being observed from different places. We can see this effect in day to day life, when a close object, such as our thumb at the end of our extended arm, appears to shift in position relative to the background when observing using one eye at at time. By extending this principle to the sky, we can measure the distance to a nearby star by observing it from two different locations, which we may translate into two different points in time, such as morning and evening (diurnal parallax), or summer and winter (annual parallax). By measuring the apparent angular shift in position relative to more distant, and thus apparently fixed background stars or galaxies, and combining it with the known distance of movement (radius of the Earth, or distance to the Sun), we can use simple trigonometry to calculate the distance to the star. Figure 1.1 illustrates the geometry of a parallax system. Parallax can, however, only be used to distances up to kiloparsec scales (see e.g. Docobo & Andrade, 2015; Kim et al., 2016) due to the limitations in angular resolution. Therefore, other measurement methods are required to obtain distances outside our Galaxy.

One popular measurement method is to use a standard candle. A standard candle is an object whose luminosity may be inferred, and compared to the observed flux of the same object. Since light follows the inverse square law, the so-called luminosity distance D_L may

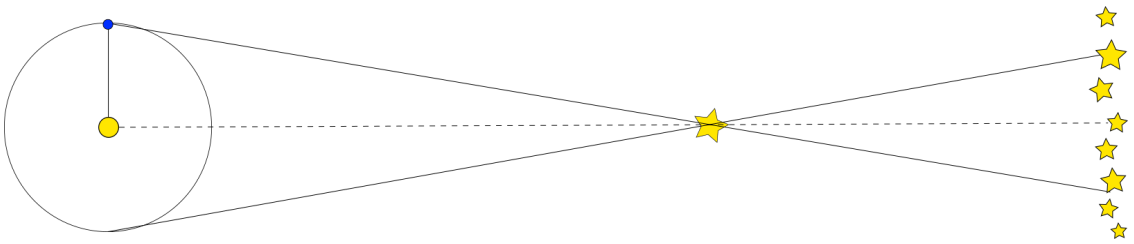

FIGURE 1.1: We have here illustrated an annual parallax system. Given the known radius of the Earth's orbit and the measured angle by which the nearby star moves relative to the background stars, it is possible to use trigonometry to infer the distance to the nearby star.

then be calculated by inverting the luminosity-flux relationship,

$$F = \frac{L}{4\pi D_L^2}, \tag{1.2}$$

where F is the flux and L is the luminosity of the object. One type of standard candles is found in Cepheid variable stars. Leavitt (1908); Leavitt & Pickering (1912) discovered a relationship between the period of Cepheid variables and their luminosity, now referred to as the Cepheid period-luminosity relationship. Cepheid variables have been important in the history of astrophysics, in particular by contributing to the proof of an expanding universe, derived by Lemaître (1927) (English: Lemaître, 1931), and proven by Hubble (1929). They still play an important role in the calibration of the cosmic distance ladder (see e.g. Soszynski et al., 2008; Ngeow et al., 2015), required in the calculation of the Hubble constant, H_0 (see e.g. Tammann, Sandage & Reindl, 2008; Freedman & Madore, 2010), however, their low luminosity only allows to use them for distance measurements in the local universe, of order of a few tens of megaparsecs (see e.g. Riess et al., 2009).

Type Ia supernovae form another important group of standard candles. Not only are supernovae the established standard candles we currently observe at the highest redshifts, but they have also been important in significantly adding to our knowledge about the universe. Only about two decades ago, the universe's expansion was believed to be decelerating. However, with the effort of two independent supernova surveys, the universe was found by Riess et al. (1998) and Perlmutter et al. (1999) to be undergoing accelerated, not decelerated, expansion. While this discovery certainly has been extremely important, and led to a Nobel Prize in Physics in 2011, supernovae are also limited as distance measurement tools, and can only be observed to redshifts of $z \lesssim 2$ (Jones et al., 2013). Therefore, there is a large amount of the universe in which the distances can only be approximated using redshifts.

Due to the presence of AGN both in the local universe and spread throughout to redshifts of $z > 7$ (Mortlock et al., 2011), there has been an ongoing hope that these objects may be used as standard candles. While most attempts have been unsuccessful (see e.g. Baldwin, 1977; Marziani et al., 2003), advances in technology and understanding have allowed progress in the work of finding a way of using AGN as standard candles. We will now familiarise ourselves with AGN, and later with the process of reverberation mapping, a method we hope will lead to the establishment of AGN as the new high redshift standard candles.

1.2 Active Galactic Nuclei

It is commonly accepted that every large galaxy has a SMBH at its centre. While each black hole is different, one subset of them, namely those accreting large amounts of matter, are responsible for the classification of so-called active galaxies (Ryden & Peterson, 2010, Chap. 21). Active galaxies can also be sub-categorised depending on their features, however, the most characteristic feature separating them from quiescent (normal, "inactive") galaxies is that they exhibit a large amount of non-stellar emission, some of which originates in non-thermal, violent processes. It is exactly this energetic activity that gives active galaxies their name. Active galaxies are sub-categorised according to their observed luminosity, the amount of radio signal they are producing, and the shape of the emission lines. This results in classifications such as Seyfert 1 galaxies, Seyfert 2 galaxies, quasi-stellar objects (QSOs) and radio galaxies, or blazars. For our work we make study Type 1 quasi-stellar objects and Seyfert 1 galaxies, which are galaxies where the central regions of the AGN can be seen by the observer. Please refer to Peterson (1997, Chap. 1) or Ryden & Peterson (2010, Chap. 21) for more details about the various active galaxies, as the classification details are otherwise not crucial to the background information for this Thesis. The light from active galaxies is often concentrated in the central parts of the galaxy, the active galactic nucleus AGN, the luminosity of which can be over 100 times larger than that of the rest of the galaxy combined. A unified model suggest that AGN are somewhat flattened, and the observed differences between the "different" types of active galaxies is simply and orientation effect. Figure 1.2 shows how the association between the different active galaxy types and the viewing angle.

AGN are complicated regions of a galaxy with a number of components, as indicated in Figure 1.2. It is believed that the bulk of an AGN's luminosity originates from the accretion disk of its central SMBH. If we assume that a mass m falls from a radius r much larger than the Schwarzchild radius of the black hole (BH), $r_{\rm Sch} = 2GM_{\rm BH}/c^2$, (Peterson, 1997, Eq. 3.9) the reduction in its potential energy is

$$\Delta E = -\frac{GM_{\rm BH}m}{r} - \left(-\frac{GM_{\rm BH}m}{r_{\rm Sch}}\right) \approx \frac{GM_{\rm BH}m}{r_{\rm Sch}} = \frac{1}{2}mc^2. \tag{1.3}$$

If the mass were to fall directly into the BH, this energy would add to the total energy of the BH. A more realistic scenario, however, is that the mass will interact with other particles orbiting the BH in the accretion disk, thus converting the energy to thermal energy, some of which we may observe as the strong source of emission from the AGN. We can assign an efficiency η of the energy transfer, such that the photons carrying away the energy of a mass m have a total energy of

$$\Delta E_\gamma = \eta mc^2. \tag{1.4}$$

Since luminosity is the amount of emitted energy per unit time, the AGN luminosity becomes

$$L = \eta \dot{M} c^2, \tag{1.5}$$

where $\dot{M}$ is the accretion rate of the BH. According to theory for a thin accretion disk, there is a maximum accretion rate $\dot{M}_{\rm E}$ at which a non-rotating black hole can grow (see

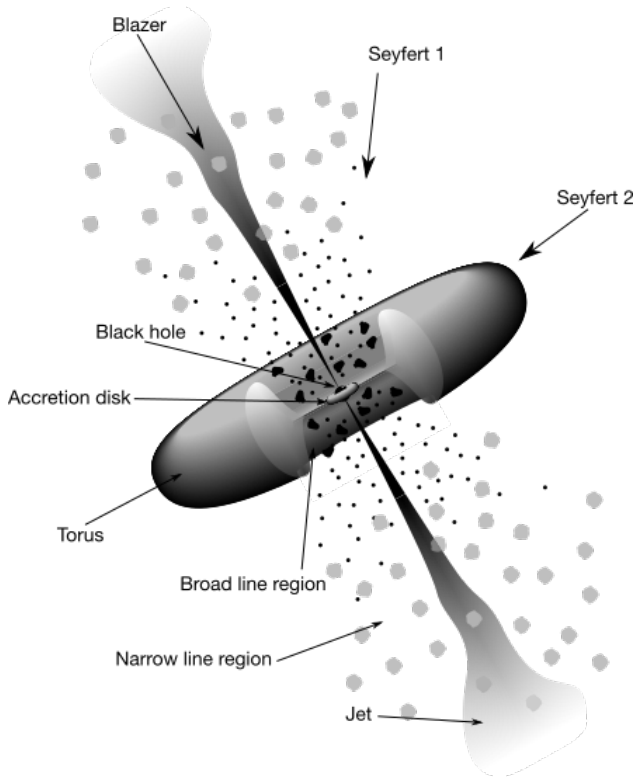

FIGURE 1.2: A schematic view of an AGN based on a unified model. The figure shows the elements of the AGN, as well as the angles which correspond to different active galaxy classifications. The figure is adapted from Urry & Padovani (1995).

e.g. Paczyński & Wiita, 1980; Abramowicz, Calvani & Nobili, 1980). The ratio between the accretion rate of the BH and of the maximum accretion rate, $\dot{m} = \dot{M}/\dot{M}_{\rm E}$, is referred to as the Eddington ratio. Despite the theoretical impossibility of accretion above this ratio, there are observations pointing to the existence of BH with super-Eddington accretion (see e.g. Fan et al., 2001; Okuda, 2002; Kollmeier et al., 2006; Reid et al., 2014). BH growth is a research area still to be explored, and RM is one potential way of investigating BHs at different stages of their lives, thus allowing to study their growth.

The accretion disk is also likely to be the starting point of an AGN's jets. If magnetic fields are present, they are likely to rip away parts of the ionised gas from the accretion disk, and forcing it to move according to the field. The matter particles are flung out in space to large distances, such that the jets can extend past the rest of the galaxy. The jets also become the area for the strongest radio emission.

Somewhat outside the accretion disk, though long before the end of the jets, are clouds of gas that are dynamically strongly affected by the BH. While the radio jets easily can extend beyond the rest of the galaxy, the gas clouds in question are within light days to light years from the BH (see e.g. Peterson, 1988; King et al., 2015). The energetic photons streaming from the accretion disk ionise the clouds, and the strong gravitational pull forces the clouds to move at high speeds to maintain their orbits. At a certain distance from the BH, the flux is small enough for neutral regions to exist. Photons reaching these regions may partially

photonionise the clouds, resulting in a cascade of recombination lines. The velocities of the clouds are still large at these radii, resulting in Doppler broadening of the emission lines from these region, thus giving the name to the area; the broad-line region (BLR).

Dust particles such as graphite cannot survive in regions with strong ultraviolet (UV) radiation; they evaporate if in a place where the equilibrium blackbody temperature above ∼1500 K. The radius at which graphite can exist is called the dust sublimation radius, and it is considered to be the starting point of the so-called obscuring, or dusty, torus. The presence of dust is significant in AGN, as it is in other areas of astronomy. In the unified AGN model it provides the opacity needed to hide the central parts of the AGN if observed at the right angle, leading us to observe seemingly different active galaxies.

The narrow line region (NLR) is made up of interstellar gas, which is less dense than that of the BLR. The region is also larger, and extends much further from the BH. As the name suggests, the emission lines from this area are more narrow than those from the BLR, which is a consequence of the larger distance from the BH. Both permitted and forbidden emission lines are observed to arise from this region. Permitted emission lines are emission lines occurring readily on Earth and other high density environments. Forbidden emission lines correspond to low probability transitions from metastable energy levels in atoms. The low probability leads to a long lifetime for the transitions, and in sufficiently high density regions the energy is carried away by atom collisions before the low probability transition may occur. The term "forbidden" is thus somewhat misleading, as the transitions can occur, if given the right conditions. In space, the atom density may become low enough for such transitions to occur, thus allowing them to be observed (Allen, 1987). With a larger distance to the BH, the broadening of the emission lines is not equally strong in the narrow line region, resulting in narrow emission lines for both the permitted and forbidden types.

1.3 Reverberation Mapping

Over the lifetime of an AGN, the accretion disk of a black hole in an AGN is a rough approximation to a continuous, ionising light source. However, it has been found to vary in flux over time, on time scales of days to many weeks, and sometimes even longer (Peterson, 1993). Moreover, the emission lines originating from the BLR have also been observed to have flux variations roughly corresponding to the flux variations of the continuum source, shifted in time by days, weeks or months (see e.g. Peterson, 1988 for an overview over early observations). From this behaviour we can conclude the following:

1. The BLR is optically thick at the ionising wavelengths, and the emission lines originating there respond to changes in the accretion disk flux, and

2. The distance between the accretion disk and BLR is small, of the order of a light year or less.

It is worth noting that the emission lines from the BLR are created when atoms are photoionised, and an electron is captured and cascades down to its lowest energy state. For this reason, the most important wavelengths are those with sufficient energy for photoionisation to occur; $\lambda < 912$ Å. These wavelengths cannot be used for reverberation mapping due to

absorption by neutral hydrogen in our Galaxy, so we make use of longer wavelengths as a proxy for the ionising continuum.

Reverberation mapping (RM) is the technique of inferring physical properties of a black hole and its BLR from measurements of the time lag between variations in the black hole's continuum and emission line fluxes. Reverberation mapping can be performed despite the fact that the true shape of the BLR is not known; in fact, the method of reverberation mapping was partly developed in an attempt to learn more about this region of AGN. By measuring the time lag between the flux variations originating at the accretion disk and in the BLR of a black hole we obtain an estimate of the BLR size. For reverberation mapping to be applicable, a set of assumptions must be made about the system (see e.g. Peterson, 1993; Peterson & Horne, 2004). We assume the following:

1. The continuum emission originates in a single, central source, much smaller than the BLR;

2. The continuum source and emission clouds only make up a small fraction of the total BLR volume;

3. There is a simple – although not necessarily linear or instantaneous – relationship between the observed and ionising continuum, the latter of which is responsible for the emission lines;

4. The light travel time across the BLR, $\tau_0 = r_{\rm BLR}/c$, which we will now refer to as the lag of the AGN, is the most important time scale. Other time scales, for which we also make assumptions, are also present:

   (a) The recombination time scale, which is the amount of time required for the emission line gas to re-establish photoionisation equilibrium for a change in continuum luminosity, is practically instantaneous relative to the AGN lag;

   (b) The dynamical time scale, $\tau_{\rm dyn} \approx r_{\rm BLR}/\Delta V$; the time it takes for the gas clouds to have moved a significant amount to impact the observations, must be longer than the RM campaign.

The time scale of light travel across the BLR ranges between days at the shortest to a few years at the longest. In comparison, the recombination time scale is of the order of minutes for typical BLR densities, thus being practically instantaneous compared to the AGN lags. The dynamical time scale is of order $c/\Delta V$ times the AGN lag, where ΔV is the velocity dispersion of the BLR clouds (Peterson & Horne, 2004). The velocity dispersions are usually of order 5000-10 000 km/s (Véron-Cetty & Véron, 2000). Assuming a velocity dispersion of 10 000 km/s, we obtain a dynamical time scale of ∼2.5 years for an AGN with one month lag in the observer frame. In order to avoid smearing effects from the cloud dynamics, reverberation mapping campaigns should be kept short compared to the dynamical time scale. The length of the DES/OzDES surveys, for which the analysis in this Thesis is performed, is five years. The length of the surveys can therefore be a point of concern. However, the majority of the AGN in the DES/OzDES sample are expected to have observed time lags longer than a month, so only a small fraction of the AGN would be

impacted by the survey length. The most fragile of the reverberation mapping assumptions is likely to be about the relationship between the optical and ionising continuum, as they should be varying in sync for best reverberation mapping results. Kilerci Eser et al. (2015) have investigated the relationship between the optical and UV continuum luminosities, and found a strong, though non-linear, relationship between the two.

There are several ways of determining the lag of an AGN. Gaskell & Sparke (1986) proposed using cross-correlation for determining AGN time lags, based on Cherepashchuk & Lyutyi (1973). Due to its simplicity and good results, the method of cross-correlation is still in use, and is even being applied in more advanced scenarios (see e.g. Fine et al., 2012, 2013). Kelly, Bechtold & Siemiginowska (2009) showed that a damped random walk describes the optical flux variability of AGN well, opening up for a new, non-analytic way of determining AGN lags. This has made it possible to utilise the method of Markov chain Monte Carlo (MCMC) to simulate continuum light curves simply by adding in a self-correcting term to the random walk, which ensures the damping; that the fluctuation happens around a given mean value. By assuming that the emission line light curves can be obtained by smoothing the continuum light curve in a particular way, this also opens up for the possibility of time lag estimation by MCMC processes. The damped random walk method has been applied in the development of Javelin (Just Another Vehicle for Estimating Lags In Nuclei), previously known as Spear (Stochastic Process Estimation for AGN Reverberations), by Zu, Kochanek & Peterson (2011). Javelin is specially designed to compute the lags for AGN, as suggested by the name, and has been used for that purpose throughout this project. More specifics will follow in Section 2.2.

Woltjer (1959) was the first to estimate the masses of AGN utilising the distances between the accretion disks of supermassive black holes and their BLRs, and RM has proved useful in estimating the masses of supermassive black holes by assuming virialisation of the BLR gas clouds (see e.g. Peterson et al., 2004; Denney et al., 2010). The black hole mass is then given by

$$M_{\mathrm{BH}} = f\,\frac{r_{\mathrm{BLR}}(\Delta V)^2}{G}, \tag{1.6}$$

where r_{BLR} is the radius of the BLR, estimated by RM, ΔV is the BLR velocity dispersion, estimated by the Doppler width of the emission line, G is the gravitational constant, and f is a factor of the order of unity, depending on the kinematics, structure, and inclination of the BLR. An estimation of the numerical value of f was made by Onken et al. (2004), yielding $f = 5.5 \pm 1.9$.

Kaspi et al. (2000) found a strong correlation between an AGN's luminosity and its BLR size, a relationship which since has been confirmed (see e.g. Bentz et al., 2009; Denney et al., 2010). Based on the photoionisation model of an AGN the photoionisation may be described by the photoionisation parameter U, given by

$$U = \frac{Q(H)}{4\pi r_{\mathrm{BLR}}^2 c n_e}, \tag{1.7}$$

where $Q(H)$ is the rate of production of the hydrogen-ionising photons by the central source, and n_e is the free electron density (e.g. Peterson, 1988, 1993). The photoionisation parameter

characterises the equilibrium state of the gas, and for pure hydrogen gas photoionisation equilibrium, meaning that the rates of photoionisation and recombination are equal, occurs when $U = 1$. From Equation (1.7) we see that if U and n_e are constant in all AGN, $r_{\rm BLR} \propto \sqrt{Q(H)}$. Based on the similarity of spectra obtained from various AGN we can expect the conditions in the BLR of different AGN to be similar, meaning the assumption of constant U and n_e is realistic to first order. Baldwin et al. (1995) also argue that there are strong selection effects in BLR emission, such that the emission of specific lines is dominated by regions of the BLR with similar U and n_e values, even if vastly different gas conditions exist elsewhere in the BLR. With this in mind, and knowing that the production rate of hydrogen ionising photons should be proportional to the luminosity, it follows that the relationship between the luminosity and BLR size, called the $R-L$ relationship, is given by $r_{\rm BLR} \propto \sqrt{L}$. Kilerci Eser et al. (2015) show that observations seem to point to a relationship somewhat different to, or maybe more complicated than, this simple proportionality. An important reason for this is that optical wavelengths often are used as a proxy for the ionising flux for RM purposes, and the optical flux does not map to the ionising flux linearly. If continuum flux from UV wavelengths is used instead, the relationship is closer to that predicted by theory. However, with a known $R - L$ relationship, regardless of its exact form, the luminosity of an AGN may be inferred if the BLR radius has been measured using reverberation mapping, which means that it should be possible to use AGN as standard candles.

As a consequence of the observed $R-L$ relationship an AGN with a higher luminosity will have longer time lags, since a more luminous source can ionise a larger volume. To observe AGN at greater distances from the observer with the same amount of flux the luminosities of the AGN must increase, thus implying longer time lags for more distant AGN. In addition, due to the expansion of the universe, the AGN lag is perceived to be longer by the observer than it's intrinsic length, scaling with a factor of $1+z$ according to the rules of time dilation. Our ability to recover an AGN time lag reliably is highly dependent on the survey compared to the lag time Horne et al. (2004). This implies that the more distant the AGN one wishes to determine a lag for, the longer the survey needs to be.

Redshift not only contributes to making the observed time lag of an AGN longer than they intrinsically are in the frame of reference of the AGN; it also causes a shift in the observed spectrum. This leads to different emission lines being present at different redshifts. The three most popular lines for RM are the Hβ, Mg II and C IV lines, and they can be observed in different redshift windows. Based on the wavelength range of AAOmega spectrograph (3750-8900 Å, Saunders et al., 2004; Smith et al., 2004), used for the data collection this Thesis is based upon, the windows of choice are as follows: Objects with redshift $z < 0.69$ are measured by the Hβ line. This line, together with the Mg II line, can be used for redshifts $0.69 < z < 0.74$, after which Mg II is the only available emission line in the redshift range $0.74 < z < 1.58$. Between $1.58 < z < 1.94$, Mg II can be used together with C IV, and C IV is the emission line to use for redshifts $z > 1.94$ (King et al., 2015, priv. comm.).

We have already stated that RM allows to determine the BLR size. Generalising this idea, RM could be used to probe the shape of the BLR by studying the properties of the "echo" (Peterson, 1993; Horne et al., 2004). This is easy to realise by the following, simple thought experiment: Assume the BLR is an infinitesimally thin ring around the continuum

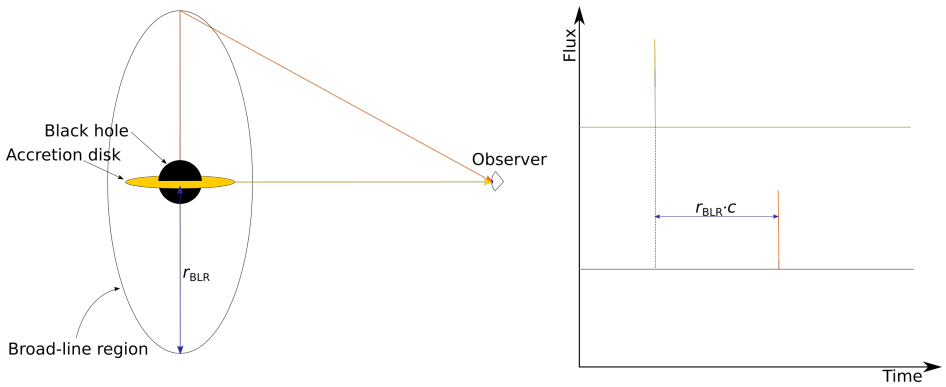

FIGURE 1.3: Illustration of an overly simplistic reverberation mapping scenario. One burst of light originating at the accretion disk of an AGN is observed at a given time. A certain amount of time later, a similar burst is observed from the BLR. The time difference between the two observations corresponds directly to the light travel time between the accretion disk and the BLR if the accretion disk-observer and BLR-observer distances can be approximated to be equal.

source which is face-on to the observer. Next, let there be one burst of light at the central black hole. Some of the light from the continuum source will then travel directly towards the observer. Some, however, will travel towards the BLR ring and reach all points on the ring simultaneously. This scenario is represented in Figure 1.3. Using that the recombination time is practically instantaneous, all points at the ring will emit the light at the same time, and all the light from the BLR will reach the observer simultaneously. The observer will then see two bursts of light, one from the continuum source, and one from the BLR, where the latter is delayed by the time it takes the light to travel the extra distance. Of course, if the ring is edge on to the observer, some of the light from the BLR will follow the same path as the continuum light to the observer, and hence not be delayed, while some light will have to travel to the back end of the BLR before travelling to the observer, resulting in a distinctly longer time lag. By considering various geometric scenarios and comparing them to observations one may attempt to find the true shape of the BLR. A more extended discussion on this topic will be presented in Chapter 3.

1.4 DES & OzDES

The Dark Energy Survey (DES) was proposed by the Dark Energy Survey Collaboration (Flaugher, 2005) with the aim of using four distinct probes to investigate dark energy; type 1a supernovae, weak lensing, baryon acoustic oscillations, and galaxy cluster counts. The collaboration were to provide a new instrument for the CTIO Blanco 4 m telescope in northern Chile in exchange for up to 30% observing time over the course of five years. The chosen instrument came to be the 570 megapixel Dark Energy Camera (DECam), allowing for excellent photometric measurements (Flaugher et al., 2012). DES required spectroscopic follow-up for many of their science goals, so OzDES (Australian Dark Energy Survey[1]) was

[1]Or, Optical redshifts for the Dark Energy Survey.

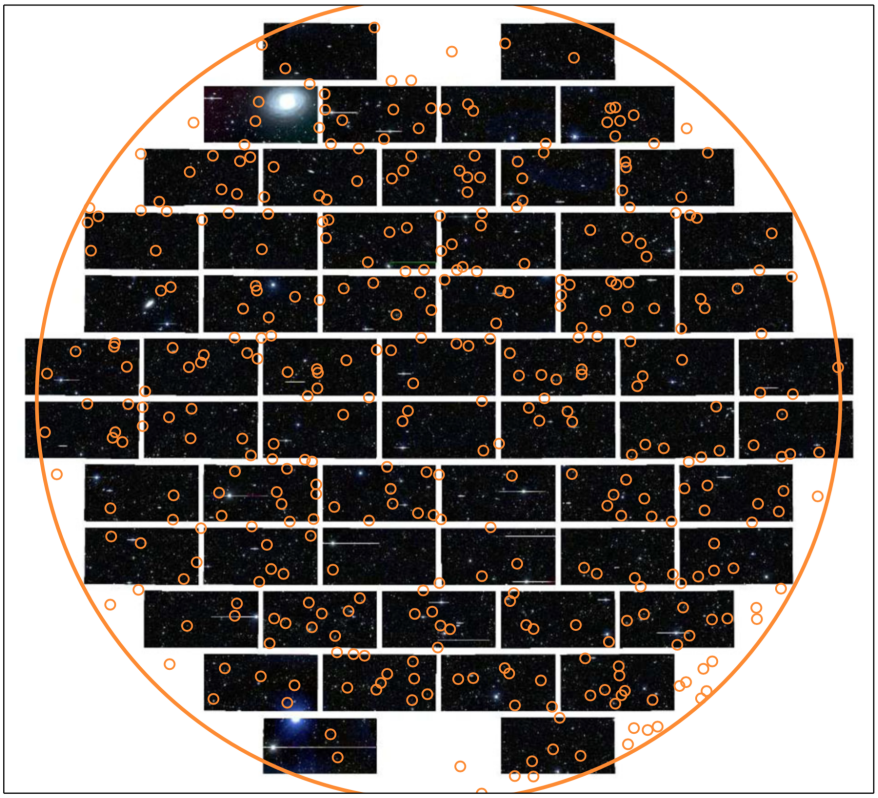

FIGURE 1.4: The DES and OzDES fields of view. The large orange circle represents the field of view of the AAO, with the 400 fibres of the 2dF represented by the smaller orange circles for one configuration of the AAT. The DECam has a very similar field of view, symbolised by the mosaic image background.

created. OzDES makes use of the 3.9 m Anglo-Australian Telescope (AAT), together with its new AAOmega spectrograph and the Two Degree Field (2dF) 400-fibre multi-object fibre-positioning system (Yuan et al., 2015). The two telescopes both have a 2 deg diameter field of view, as shown in figure 1.4, which allows for very effective spectroscopic follow-up of DES by OzDES.

Today, the main scientific goals of DES and OzDES still include targeting type Ia supernovae, but RM of AGN has become another important goal. Fortuitously, the observing program designed for type Ia supernovae is also ideal for RM. We observe AGN at redshifts $0 < z < 4$, with r-band apparent magnitudes $18.0 < m_r < 20.5$ (King et al., 2015). This is done by targeting ten fields, covering a total area of $30\,\mathrm{deg}^2$, with a cadence of approximately 6 days for the photometric measurements over the course of each observation season, lasting from August to January the following year (Diehl et al., 2014; Yuan et al., 2015). The high cadence is to ensure the discovery of transient objects, and monitoring of variable objects like AGN. The spectroscopic measurements are fewer, with 100 nights spread over five years, as opposed to 525 nights for the photometry, spread out over the same time, thus resulting in rarer observations[2]. Because DES will have accumulated a larger number of interesting

[2]An application for a change for the OzDES survey has recently been submitted and accepted. While the total number of observation nights is to remain the same, four nights will now be moved from the fourth

targets for spectroscopic follow-up over time, the number of observations per season increases in time for OzDES. The surveys started their official collection of data in 2013, ending their third year (Y3) of observations in January 2016. At this point in time we expect there to be sufficient data for RM to be successful for a subset of the monitored AGN ($\geq 10\%$, King, priv. comm.).

While RM has been a field progressing over the last decades, the AGN monitored have been few, and at low redshifts. Currently, only 64 AGN have succesful RM measurements, of which the vast majority are located in the local universe ($z < 0.1$), with very few exceptions (Bentz & Katz, 2015). The highest redshift AGN with a tentative RM measurement is S5 0836+71, with a redshift of $z = 2.172$ (Kaspi et al., 2007). The Sloan Digital Sky Survey Reverberation Mapping (SDSS-RM) project will contribute to expanding the RM catalogue, targeting 849 AGN in a redshift range of $0.1 < z < 4.5$ (Shen et al., 2015). With a six month program in the first half of 2014, however, SDSS-RM is only expected a success rate of ∼10%. Due to the short observing period of this survey is is also expected that the fraction of AGN with recovered time lags will be biased towards lower redshift values, due to the effects discussed in Section 1.3. The program has been extended for an additional year, and will continue attempting to extend the observations, but with no guarantees of telescope time. (Shen et al., 2016). DES and OzDES will contribute to increasing the number of AGN with successful RM further. The surveys target ∼700 AGN, which King et al. (2015) predict a ∼35-45% RM success rate at the end of the five years, implying a significant increase in number of AGN with successful RM. Moreover, because the targeted AGN are distributed in redshifts $0 < z < 4$, and the survey length is over several years, the AGN observed by DES and OzDES will be an important contribution to the catalogue, providing RM data for substantially higher redshifts than before.

1.5 Thesis Outline

This Thesis investigates reverberation mapping with simulations based on the expected type of data from DES/OzDES. In Chapter 2 we present the various parameters needed for this research, and summarise the result of an analysis of optimal parameters for running Javelin on DES/OzDES data. A more thorough discussion on this topic is to be found in Appendix A. We move on to discussing the transfer function in Chapter 3, deriving its shape based on a few idealistic BLR distributions, and testing how Javelin is affected by receiving data which have been obtained using a transfer function different from its expectations. We introduce the idea of stacking analysis for reverberation mapping in Chapter 4, going through the maths of the Bayesian method we have chosen to use in our analysis. The Bayesian method is applied to several idealistic scenarios in Chapter 5 to test its reliability. Obtaining promising results, we apply the stacking analysis to more realistic DES/OzDES data in Chapter 6, optimising time lag estimation for DES/OzDES AGN samples for the Mg II emission line based on three

year, and eight from the fifth year, to a sixth year of observations. The reason for this is that it allows for further follow-up of supernova hosts discovered towards the end of DES, without it impacting the expected outcome for the reverberation mapping project. DES is not expected to extend the observational time, but we are able to use data from science verification period the year before the survey officially started. This extends the total photometric measurement period to six years.

years worth of observational data. In Chapter 7 we summarise our work, and restate the major results of this project.

I use the first person plural throughout this Thesis to stress the DES/OzDES reverberation mapping group involvement in the decisions made for the direction of the analysis. The analysis has, however, unless otherwise specified, been performed by myself under the guidance of my supervisors; Tamara M. Davis, Anthea L. King, Paul Martini, and Signe Riemer-Sørensen.

2 Parameters

Reverberation mapping has traditionally used cross-correlation techniques to estimate time lags (see e.g. Peterson, 1993; Fine et al., 2012, 2013). However, as the field of RM progresses, newer, more scientifically based methods for estimation of AGN lags have been developed. One example of this is the software package JAVELIN[1]. JAVELIN has been found to give results consistent with the cross-correlation method (see e.g. Zu, Kochanek & Peterson, 2011; Grier et al., 2012a,b); however, we are aware that inconsistencies between the methods may be, and already have been, found (Peterson et al., 2014). For that reason, and because we are aware of the pitfalls of using black box software, we decided to properly investigate JAVELIN, and decide on the optimal settings for the program for our purposes.

2.1 Describing AGN in Terms of Parameters

Any object may be described in a number of ways, by a number of parameters; its mass, size, position, or the forces acting upon it, to mention a few. The important question will always be: Which parameters are useful for describing the object we are interested in, for the purposes we are interested in? For reverberation mapping, the obvious answer is "the time lag of an AGN". However, in order to establish this value, and put it in perspective, other parameter values are also important. In this Section, we give a very quick overview over the most important parameters by which the AGN in our project and simulations are described. It should be noted that this is a non-exhaustive list of AGN parameters used in the full simulations.

[1]See Zu, Kochanek & Peterson (2011) and https://bitbucket.org/nye17/javelin for more information.

2.1.1 DES/OzDES Parameters

The direct observables in the DES/OzDES surveys are the redshift z and apparent magnitude m of an object. The apparent magnitude is a measure of the brightness of a celestial object, originally introduced by Hipparchus, and further developed by Norman Pogson (Ryden & Peterson, 2010, Chap. 13.2). While there are several ways of defining apparent magnitude, they all are on the same form;

$$m = -2.5 \log_{10} \frac{F}{F_C}, \tag{2.1}$$

where F_C is a reference flux of a known object, and F is the flux of the object of interest (Ryden & Peterson, 2010, Eq. (13.16)). The apparent magnitude, m, is closely related to a similar measure of brightness, the absolute magnitude, M. The absolute magnitude of an object is the value we would measure for the apparent magnitude if we observed the object at a distance of 10 parsec (∼32.6 light years). Using the relationship between flux and luminosity,

$$F = \frac{L}{4\pi r^2}, \tag{2.2}$$

where F is the flux of an object with luminosity L at a distance r, the absolute magnitude may be related to the apparent magnitude by

$$M = m - 5 \log \frac{d}{10 \text{ pc}}, \tag{2.3}$$

where d is the distance to the object measured in parsecs. Thus, the absolute magnitude is to luminosity what apparent magnitude is to flux.

The magnitudes of the AGN by DES/OzDES are measured through four filters; g, r, i, and z. Specific magnitudes, the magnitudes measured through filters will, of course, only account for a part of the total, or bolometric, magnitude of the object. Additionally, as distant objects are redshifted, the part of the spectrum each filter probes changes for each object. A K-correction is needed to correct for this, and to find the true, rest-frame specific magnitude of the object (Hubble, 1936; Hogg et al., 2002). For this, we make use of the DES filter response curves, which tell us how much light we are capable to observe for each wave length, and an object template, which describes the amount of light we expect to measure for each wavelength if the object was at redshift $z = 0$. To perform the K-correction, we redshift the template to the redshift of the object, and scale the template so that its observer-frame specific magnitude equals the magnitude of the object. Once we have scaled the template, we return to its rest frame state, and measure its magnitude using the specific filter of interest. In the same way, the total bolometric magnitude of the object may be estimated by integrating over the scaled spectra. K-corrections are important for our simulations, and will also be necessary to apply to DES/OzDES data to obtain successful reverberation mapping results.

2.1.2 Parameters for AGN Light Curve Simulation

We simulate our AGN based on the values of redshifts and apparent magnitudes expected from DES/OzDES. We assume a ΛCDM cosmological model with $\Omega_M = 0.30$, $\Omega_\Lambda = 0.70$, and $H_0 = 70$ km/s/Mpc (the same as used by MacLeod et al. (2010), for reasons to be explained later), to determine the absolute magnitude, and thus the luminosity, of the AGN using Equations (2.1) and (2.3). The $R - L$ relationship for each of the emission lines Hβ, Mg II and C IV are then needed to determine the lag of the AGN. King et al. (2015) summarise the research performed on the $R - L$ relation for each of the mentioned emission lines. Bentz et al. (2013) found the $R - L$ relationship

$$\log_{10}\left[\frac{R_{\mathrm{H}\beta}}{\text{light days}}\right] = (1.554 \pm 0.024) + (0.546^{+0.027}_{-0.028}) \log_{10}\left[\frac{\lambda L_\lambda(5100\ \text{Å})}{10^{44}\ \text{erg s}^{-1}}\right], \tag{2.4}$$

to provide the most precise estimate for Hβ. Hβ is the line that has been observed the most out of the three emission lines we consider, and therefore this relationship is the strongest constrained. The $R-L$ realtionship for Mg II has not been studied very well, and in contrast to the Hβ and C IV lines, it is not based on direct Mg II lag measurements. Instead, it has been estimated by Trakhtenbrot & Netzer (2012) by utilising the similarities between Hβ and Mg II, yielding

$$\log_{10}\left[\frac{R_{\text{Mg II}}}{\text{light days}}\right] = (1.340 \pm 0.019) + (0.615 \pm 0.014) \log_{10}\left[\frac{\lambda L_\lambda(3000\ \text{Å})}{10^{44}\ \text{erg s}^{-1}}\right]. \tag{2.5}$$

Finally, the $R - L$ relationship for C IV,

$$\log_{10}\left[\frac{R_{\text{C IV}}}{\text{light days}}\right] = (0.93 \pm 0.14) + (0.55 \pm 0.04) \log_{10}\left[\frac{\lambda L_\lambda(1350\ \text{Å})}{10^{44}\ \text{erg s}^{-1}}\right], \tag{2.6}$$

is based on the work of Kaspi et al. (2007). This relationship is not constrained as well as the relationship for Hβ, but, unlike the Mg II relationship, it is based on direct measurements. We make use of these formulae to create lags for our simulated AGN.

In order to recover an AGN time lag from observations, its continuum and emission line light curves are required. To simulate the reverberation mapping results of the DES/OzDES surveys, we hence need to simulate realistic AGN light curves. According to the findings of Kelly, Bechtold & Siemiginowska (2009), the continuum light curves of AGN can be modelled by a damped random walk, which can be characterised by the parameters[2] τ_D and SF_∞. The parameter τ_D represents a characteristic time scale of luminosity changes for an AGN. The amplitude of the change is described by the structure function SF, which is defined as the root mean squared magnitude difference between two subsequent measurements as a function of the time difference Δt between the measurements. SF_∞ is the asymptotic amplitude as the time difference grows large, and thus represents the degree to which an AGN's luminosity tends to change. MacLeod et al. (2010) found that the values of τ_D and

[2] MacLeod et al. (2010) use τ for one of the damped random walk parameters. We follow Zu, Kochanek & Peterson (2011); King et al. (2015) in using τ_D for this parameter, and reserve τ as a general symbol for the time lag, not to be confused with τ_0, which denotes a true time lag value.

SF_∞ depend on the central black hole mass, and the luminosity of the AGN. Therefore, to create realistic continuum light curves for our AGN, we implemented all the dependencies found by MacLeod et al. (2010). To be able to do this accurately, we need to adopt the same cosmology as MacLeod et al. (2010)[3].

The degree of damped in the damped random walk depends strongly on the definition of the structure function. The structure function for any time difference between measurements Δt is given by MacLeod et al. (2010);

$$SF(\Delta t) = SF_\infty \left\{1 - e^{-\frac{|\Delta t|}{\tau_D}}\right\}^{1/2}, \tag{2.7}$$

where $e^{-|\Delta t|/\tau_D}$ is the autocorrelation function for the DRW (Kelly, Bechtold & Siemiginowska, 2009). It is interesting to notice the limiting cases where Δt approaches zero and infinity for these functions (see e.g. Hughes, Aller & Aller, 1992, for discussion);

$$SF(\Delta t \gg \tau_D) = \sqrt{2}\sigma \equiv SF_\infty, \tag{2.8}$$

$$SF(\Delta t \ll \tau_D) = \sigma\sqrt{\frac{2\,|\Delta t|}{\tau_D}} = SF_\infty\sqrt{\frac{|\Delta t|}{\tau_D}}. \tag{2.9}$$

This shows SF_∞'s strong relationship to the change in luminosity. Specifically, SF_∞ describes how much the luminosity on average is likely to change, given a long enough period of time. Keeping in mind Equation (2.7) and it's limiting cases, we move to the continuum light curve itself. We follow Kozłowski et al. (2010) and King et al. (2015), and express the light curve by

$$C(t) = E\{C\} + \Delta C(t), \tag{2.10}$$

where $C(t)$ is the continuum light curve magnitude at time t, $E\{C\}$ is the mean value of the continuum magnitude, around which the magnitude fluctuates, and $\Delta C(t)$ is the deviation from the mean value $E\{C\}$. The deviation is given by

$$\Delta C(t + \Delta t) = \Delta C(t) e^{-\frac{\Delta t}{\tau_D}} + \sigma \left\{1 - e^{-\frac{2\Delta t}{\tau_D}}\right\}^{1/2} G(1), \tag{2.11}$$

where σ contains the SF_∞ variability as given by Equation (2.8), and $G(1)$ is a Gaussian random deviate of unit dispersion.

[3] MacLeod et al. (2010) make use of a ΛCDM cosmology with $\Omega_M = 0.30$, $\Omega_\Lambda = 0.70$, and $H_0 = 70$ km/s/Mpc to determine the i-band absolute magnitudes needed for their calculations. However, an $\Omega_M = 0.26$, $\Omega_\Lambda = 0.74$, and $H_0 = 71$ km/s/Mpc cosmology is used to find black holes mass estimates. They estimate the difference in cosmologies to correspond to a 1% effect for the best-fit coefficients for τ_D and SF_∞. We make use of the second cosmology only indirectly, by using the black hole mass distribution in terms of solar masses

$$p(\log_{10} M_{\rm BH}|M_i) = \frac{1}{\sqrt{2\pi\sigma^2}} \exp\left\{-\frac{(\log_{10} M_{\rm BH} - \mu)^2}{2\sigma^2}\right\},$$

where $M_{\rm BH}$ is the black hole mass, M_i is the i-band absolute magnitude of the AGN, and $\mu = 2.0 - 0.27M_i$ and $\sigma = 0.58 + 0.011M_i$ are the mean and standard deviation of the black hole masses, respectively, to create our simulated AGN.

Following Blandford & McKee (1982), we assume that the emission line light curve simply is the BLR response to the continuum light curve. This was also outlined in the assumptions stated in Section 1.3. If the emission from the BLR is indeed driven by the continuum source, it should be possible to express the former in terms of the latter. We define a transfer function $\Psi(\tau)$ that relates the emission line flux variations to the continuum variations by

$$\Delta L_f(t) = \int \Psi(\tau)\ \Delta C_f(t-\tau)\ \mathrm{d}\tau, \tag{2.12}$$

where $\Delta L_f(t)$ is the change in flux of the emission line light curve relative to its mean value, and similarly, $\Delta C_f(t)$ is the change in flux for the continuum light curve relative to the mean flux of the continuum light curve. It should be noted that the transfer function is defined with the continuum and emission line brightness measured in terms of flux, not magnitude, as in Equation (2.10). Based on Equation (2.12) we see that the transfer function is responsible for the smoothing and shifting of the continuum light curve we observe when looking at the emission line light curve. Specifically, the transfer function describes the response of the BLR to a δ-function flare from the continuum source.

For simplicity, we create light curves based on daily measurements for the total length of the survey. We then pick out a subset of the data, corresponding to the observation dates we expect for the survey. We also add random Gaussian error to the data, to mimic the uncertainty in measurements we expect for DES/OzDES. This way, we can make use of the same intrinsic light curve to compare various effects, such as adding a higher measurement uncertainty to the data, or using a higher sampling rate.

2.2 Parameters in Javelin

Javelin is based on the assumption that AGN can be modelled by a damped random walk, as described in Section 2.1.2. Javelin attempts to fit the continuum light curve with a damped random walk in between the measurements to obtain a continuous light curve. The emission line light curve is then computed by convolving the fitted continuum light curve with a transfer function, which in Javelin is assumed to be a top-hat function (more information and discussion of this topic in Section 3.1). The program then utilises the `emcee` MCMC method, developed by Foreman-Mackey et al. (2013), based on Goodman & Weare (2010), for simultaneous fitting of desired parameters by calculating a combined likelihood for all parameters at each MCMC step. The `emcee` algorithm has certain advantages to the standard Metropolis-Hastings MCMC algorithm (Metropolis et al., 1953; Hastings, 1970), including fewer parameters to tweak, and faster convergence of the chains, as described by Foreman-Mackey et al. (2013). When running Javelin, the program estimates five parameters; the continuum variability parameters τ_D and SF_∞, the width and height of the top-hat transfer function, and the AGN lag τ_0.

In addition to the parameters Javelin is estimating, the program obviously also contains a number of other, internal parameters. While the knowledge of many such parameters is unimportant for the user of the software, certain parameters can be tweaked in order for Javelin to process the data and find parameter estimates in an optimal way for the data set. We invested some time in testing out these parameters to obtain our estimates in the most

effective way possible. We will state the results of our findings below, but for the interested reader please refer to Appendix A for a more thorough discussion of the parameter choices. JAVELIN was originally developed to fit less noisy and higher cadence data than is expected from DES/OzDES. As a consequence it was necessary for us to tweak the source code of JAVELIN. Otherwise, the MCMC chains became divergent and an unrealistic parameter space was explored. See Appendix A for more details. JAVELIN estimates for the time lag may initially appear unreliable due to poor parameter estimation in the damped random walk and transfer function parameters (see Section A.2). However, these concerns may be disregarded due to the physical meaning of the parameters, which allow their estimates to deviate from their underlying values if the light curves are short or poorly sampled, both of which can be the case for our dataset.

As an MCMC based program, JAVELIN has a number of walkers, each of them forming a chain with a certain number of steps. Each walker is placed randomly in the permitted parameter space to wander. After some time the chain starts converging towards the equilibrium, or region of highest probability. Usually, the initial steps, which do not represent the system, are disregarded afterwards. It is common to set a fixed number of initial steps, called the burn-in period, to be disregarded for all walkers. The number of walkers, the burn-in period, and the number of steps to be taken by each walker after the burn-in period are all quantities which can be adjusted to the needs of the user. The default values of these parameters are 100, 50, and 50, respectively, but users are encouraged to use larger values (Zu, priv. comm). Based on the analysis in Appendix A we chose to use 100 walkers, 500 burn-in steps, and 1000 steps in the chain after the burn-in period.

JAVELIN also gives the user the option of controlling certain aspects about the characteristics of the lag parameter space. For instance, it is possible to specify the range of lags for JAVELIN to consider in the MCMC process. We have chosen to only look for positive values of the lag, since a negative lag would imply that the continuum behaviour follows the emission line behaviour, which contradicts our initial assumptions. We have also chosen to create a conditional maximum lag up to which JAVELIN is allowed to search. The maximum lag value to be considered is either 1000 days, or three times the true lag, whichever one is the largest. Note that when we simulate AGN, we do know their true lags, which will not be the case for real data. However, a lag can be estimated for real data using the existing $R - L$ relationships, and we can use that value to constrain the searchable lag parameter space. JAVELIN also has an option to logarithmically penalise lag values larger than a certain fraction of the total baseline, or survey time. We have chosen not to make use of this feature, and let JAVELIN explore all lags within the allowed region equally.

3

The Impact of the Transfer Function

We introduced the transfer function in Section 2.1. However, Equation (2.12) is really a special case of the more general transfer equation,

$$\Delta L_f(t, V_z) = \int \Psi(\tau, V_z)\ \Delta C_f(t - \tau)\ \mathrm{d}\tau, \tag{3.1}$$

where V_z denotes the line-of-sight velocity of the BLR clouds (Peterson, 2001). In other words, the emission line light curve is not only dependent on the BLR size and distribution, but also on the motion of the clouds in the BLR. In the general case, the transfer function $\Psi(\tau, V_z)$ is also referred to as the velocity-delay map. There have been some attempts on solving Equation (3.1), and thus recovering the velocity-delay maps of AGN (see e.g. Peterson & Horne, 2004; Peterson, 2014). However, most analyses have instead focused on solving Equation (2.12). The idea behind the transfer function is to determine how the light from the ionising continuum is affected when interfering with the BLR. If sufficiently good measurements of the continuum and emission line light curves can be made, the transfer function can potentially be inferred, which could be used to infer the distribution of the BLR clouds. Learning about the BLR shape would provide new insight in the central areas of AGN, as their geometry and kinematics are still unknown (Vestergaard, Wilkes & Barthel, 2000; Kollatschny & Bischoff, 2002; Peterson, 2006; Liu, Feng & Bai, 2015). Constraints on the BLR distribution has been attempted by for instance Pozo Nuñez et al. (2013) and Pancoast, Brewer & Treu (2014), however, work still remains to be done in this field.

The transfer function describes the smoothing and shift of the continuum light curve by the BLR. Thus, in the unrealistic, but instructive case where the continuum light curve is described by a delta function, the transfer function will effectively show the emission line light curve. Because we assume that the smoothing is due to physical properties of the system, the transfer function is expected to be dependent on, and possible to derive from, the geometry of the BLR. If this is the case, the simplest transfer functions will be those based on simple systems, such as distributions of no width. We have considered such

idealistic systems, and derived their transfer functions. In addition, we have also considered two other possible transfer functions, namely the Gauss and Gamma distributions, which previously have been considered by for instance Skielboe et al. (2015). For the purposes of this analysis we make the assumption that the AGN are at large distances, such that the small angle approximation may be used. We also assume that the central source, as well as all points on the BLR, emit light isotropically.

3.1 Transfer Functions

The simplest possible transfer function is based on a BLR distribution creating an infinitesimally thin, face-on ring around the black hole (BH). If the width of the ring is infinitesimal, all points on the BLR are at the same distance from the BH, as well as to the observer. Using small angle approximation, the emission line light is then only delayed by

$$\tau_0 = \frac{r_{\mathrm{BLR}}}{c}, \tag{3.2}$$

where r_{BLR} is the radius from the BH to the BLR. The transfer function for a face-on ring of infinitesimal width will thus be a delta function centred at time lag $\tau = \tau_0$;

$$\Psi(\tau) = \delta(\tau - \tau_0). \tag{3.3}$$

Such a δ-function has been illustrated by a blue curve in Figure 3.1.

A slight increase in the complexity may be achieved by giving the face-on ring a small width $2\mathrm{d}r$. In that case, the time lags will vary between $\tau = (r_{\mathrm{BLR}} - \mathrm{d}r)/c$ and $\tau = (r_{\mathrm{BLR}} + \mathrm{d}r)/c$. The assumption of an isotropic system will, however, make sure that the amount of light seen by the observer remains the same for all times within $\tau \in (r_{\mathrm{BLR}} \pm \mathrm{d}r)/c$, resulting in a top-hat function centred at τ_0, with width $2\mathrm{d}\tau$, where we remind that $\tau_0 \equiv r_{\mathrm{BLR}}/c$, and $\mathrm{d}\tau = \mathrm{d}r/c$. A top-hat transfer function is shown in Figure 3.2. Figure 3.3 shows an example of light curves originating at the continuum source and a BLR of this sort. To generate the emission line light curve, Equation (2.12) was used with a top-hat transfer function with a width of 20% of the time lag τ_0. Figure 3.3 illustrates the impact of the transfer function; as expected, the emission line light curve looks like a smooth and shifted version of the continuum light curve. However, because the transfer function was chosen to be narrow for this example, the light curves remain similar in shape, which allows for easy estimation of the time lag τ_0.

Assuming now that the BLR is distributed as an infinitesimally thin, edge-on ring, the δ-function luminosity flare at the continuum will result in a light distribution from the BLR which is a function of the BLR's distance distribution relative to the observer. This may be described as a function of the angle,

$$\tau = \tau_0(1 - \cos\theta), \tag{3.4}$$

where the system is shown in Figure 3.4, and the distance has already been transformed into delay by dividing by the speed of light c. Following the BLR ring in Figure 3.4, we realise that small changes in θ close to $\theta = 0$ and $\theta = \pi$ will result in a lot of light reaching the

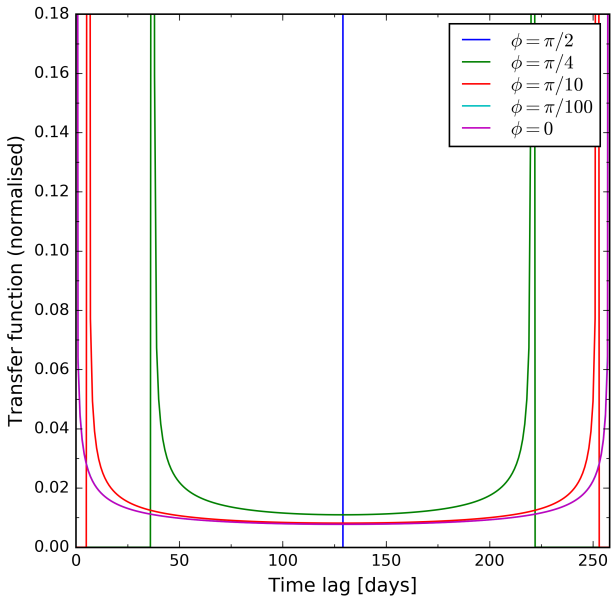

Figure 3.1: Transfer functions for five different BLRs, distributed as infinitesimally thin rings around the BH at a distance corresponding to a lag of $\tau_0 = 129$ days. The different colours represent different inclinations of the ring, where $\phi = 0$ represents a ring viewed edge-on by the observer, and $\phi = \pi/2$ a ring which is face-on. Due to the similarity in the shape of the transfer function for a ring with inclination $\phi = \pi/100$ with that of an edge-on ring, the transfer function for the $\phi = \pi/100$ ring is not visible in this figure.

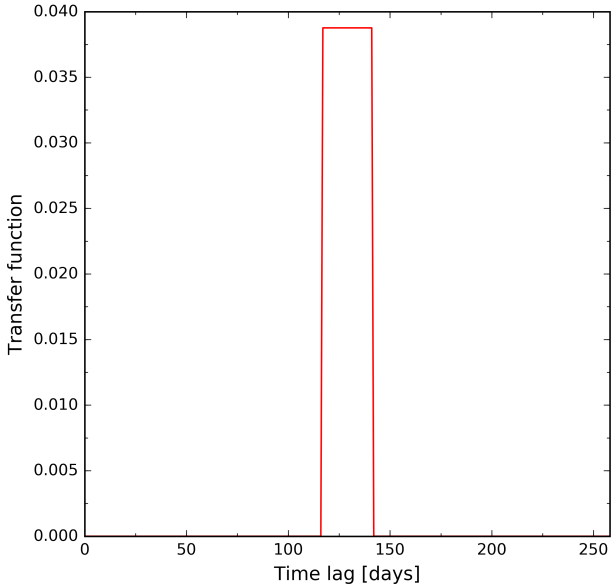

Figure 3.2: A top-hat transfer function, which the the transfer function we obtain for a face-on ring with a final width around the central BH. In this case, the BLR is located at a distance corresponding to a lag of $\tau = 129$ days from the BH, extending to a distance of 10% of the 129 day distance on each side of the 129 day mark.

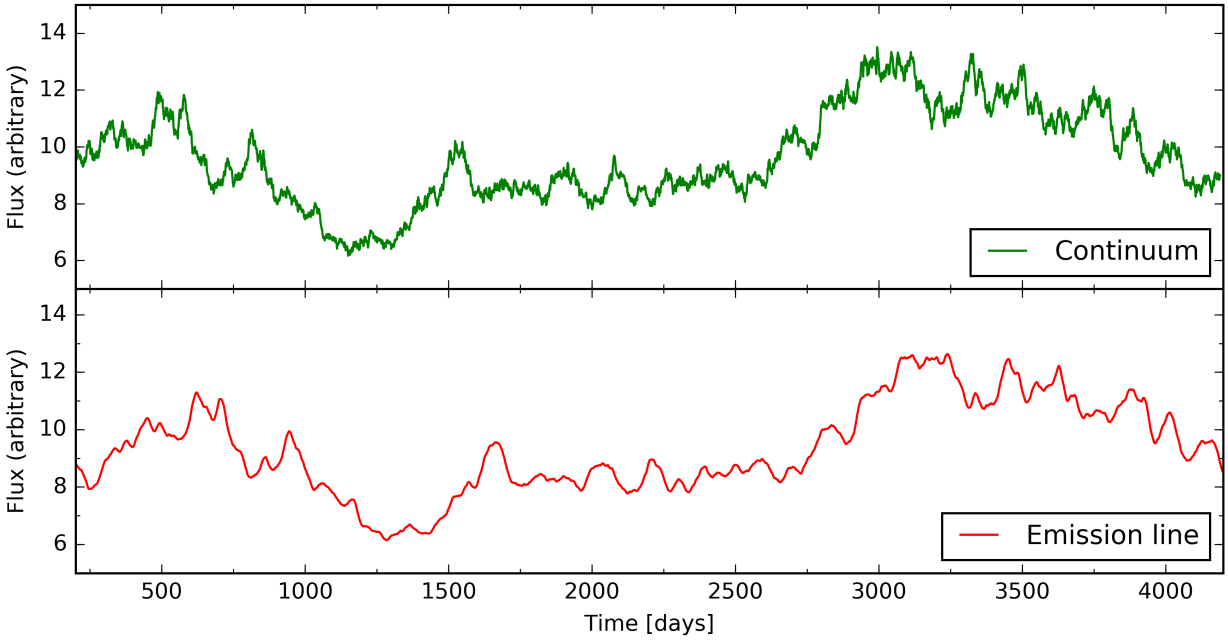

FIGURE 3.3: One possible light curve for an AGN where the transfer function is assumed to be the same as in Figure 3.2, namely located at a distance of $\tau_0 = 129$ days, with a width of $0.2\tau_0$.

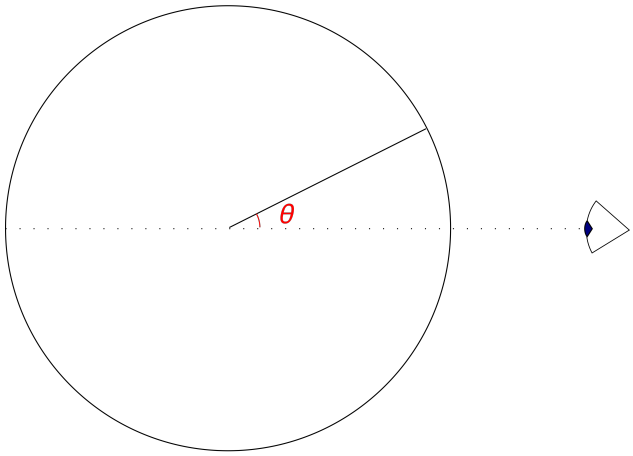

FIGURE 3.4: Geometry of a ring viewed edge-on by the observer. Any point on the ring may be given as a function of the viewing angle θ.

observer within a small amount of time, due to the small changes in line-of-sight distance between adjacent points on the ring. Conversely, around $\theta = \pi/2$ the change in line-of-sight distance for two adjacent points is larger, resulting in less light to be observed. A more rigorous way of stating this is that the transfer function in this case simply is the derivative of θ with respect to τ. Thus, by inverting and taking the derivative of Equation (3.4) we obtain

$$\begin{aligned}\Psi(\tau) = \frac{\mathrm{d}\theta}{\mathrm{d}\tau} &= \frac{\mathrm{d}}{\mathrm{d}\tau}\arccos\left(1-\frac{\tau}{\tau_0}\right)\\ &= -\frac{1}{\sqrt{1-\left(1-\frac{\tau}{\tau_0}\right)^2}}\cdot\left(0-\frac{1}{\tau_0}\right)\\ &= \frac{1}{\tau_0\sqrt{1-\left(1-\frac{2\tau}{\tau_0}+\frac{\tau^2}{\tau_0^2}\right)}}\\ &= \frac{1}{\sqrt{\tau(2\tau_0-\tau)}}\end{aligned} \tag{3.5}$$

for an edge-on ring. This function is shown in Figure 3.1 by the magenta curve.

One may easily extend the scenario of the edge-on ring to an infinitesimally thin ring with any inclination. The geometry of such a scenario is presented in Figure 3.5. In this case, the inclination of the ring is given by the angle ϕ, ranging between 0 and π, where $\phi = 0$ is equivalent to the edge-on ring, and $\phi = \pi/2$ to the face-on ring. The time delay in this scenario given by

$$\tau = \tau_0(1-\cos\phi\cos\theta), \tag{3.6}$$

where $\tau \in \tau_0(1\pm\cos\phi)$. In order to obtain the transfer function, we again take the derivative of θ with respect to τ;

$$\begin{aligned}\Psi(\tau) = \frac{\mathrm{d}\theta}{\mathrm{d}\tau} &= \frac{\mathrm{d}}{\mathrm{d}\tau}\arccos\left\{\frac{1-\tau/\tau_0}{\cos\phi}\right\}\\ &= -\frac{1}{\sqrt{1-\left(\frac{1-\tau/\tau_0}{\cos\phi}\right)^2}}\cdot\left(0-\frac{1}{\tau_0\cos\phi}\right)\\ &= \frac{1}{\tau_0\cos\phi\sqrt{1-\frac{1}{\cos^2\phi}+\frac{2\tau}{\tau_0\cos^2\phi}-\frac{\tau^2}{\tau_0^2\cos^2\phi}}}\\ &= \frac{1}{\sqrt{\tau_0^2(\cos^2\phi-1)+2\tau\tau_0-\tau^2}}\\ &= \frac{1}{\sqrt{-\tau_0^2\sin^2\phi+\tau(2\tau_0-\tau)}}.\end{aligned} \tag{3.7}$$

Of course, this is simply a more general version of Equation (3.5), with Equation (3.7) reducing to Equation (3.5) when $\phi = 0$. In Figure 3.1, the transfer functions for five different inclinations are plotted, including the face-on and edge-on rings discussed previously.

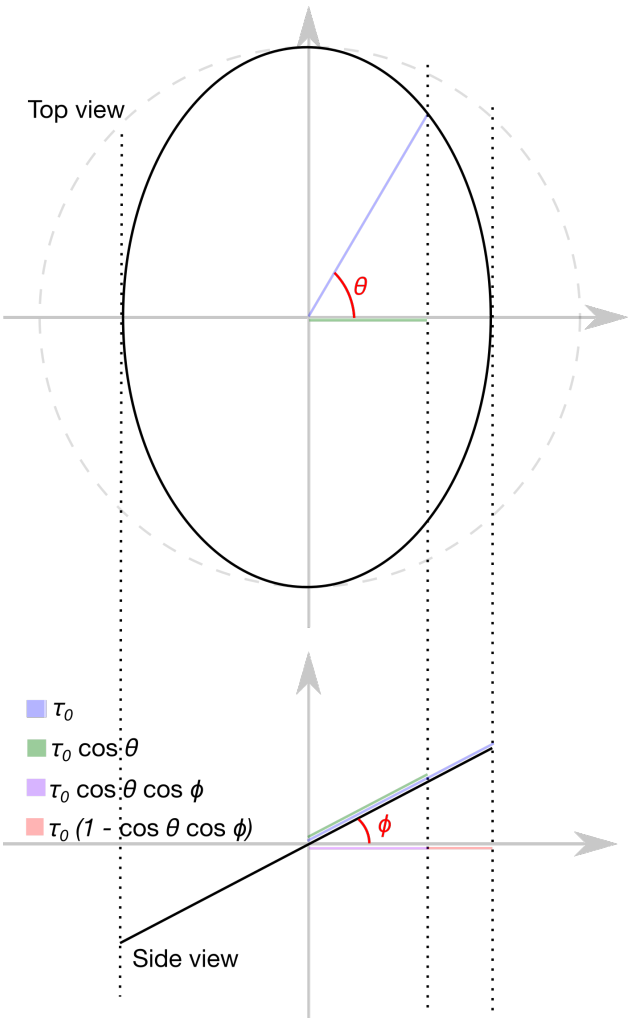

FIGURE 3.5: Geometry of a ring viewed on an inclination ϕ by the observer. Any point on the ring may be given as a function of two angles θ and ϕ.

The observant reader will notice that Equation (3.7) diverges to infinity at the boundaries $\tau = \tau_0(1 \pm \cos\phi)$. This does not imply a physical problem, as the implied infinite emission only occurs for an infinitesimal amount of time. For numerical purposes this only leads to minor complications. We keep in mind that the transfer function will be convolved with the continuum light curve, as described by Equation (2.12). The integration bounds should be defined for all times – or at least from zero to a very large number corresponding to a point in time at which the response from the BLR has stopped. We do, however, know that the transfer functions for our infinitesimally thin rings equal to zero outside of $\tau \in \tau_0(1 \pm \cos\theta)$, allowing to reduce the integral to be within these τ values. We split the integral such that

the majority of the emission line light curve and the boundaries are calculated separately;

$$\begin{aligned}\Delta L_f(t) = &\int_{\tau_0(1-\cos\theta)+\epsilon}^{\tau_0(1+\cos\theta)-\epsilon} \Psi(\tau)\ \Delta C_f(t-\tau)\ \mathrm{d}\tau \\ &+ \int_{\tau_0(1-\cos\theta)}^{\tau_0(1-\cos\theta)+\epsilon} \Psi(\tau)\ \Delta C_f(t-\tau)\ \mathrm{d}\tau + \int_{\tau_0(1+\cos\theta)-\epsilon}^{\tau_0(1+\cos\theta)} \Psi(\tau)\ \Delta C_f(t-\tau)\ \mathrm{d}\tau, \end{aligned} \tag{3.8}$$

where we require ϵ to be very small. There are two things to note about ϵ and Equation (3.8); first, $\epsilon \ll \tau_0(1 \pm \cos\theta)$ must hold, and second, if ϵ indeed is small, then $\Delta C_f(t)$ will be approximately constant over the interval, allowing to pull it out in front of the integral. It then remains to know how the behaviour of $\Psi(\tau)$ as $\tau \to \tau_0(1 \pm \cos\theta) \mp \epsilon$. Inserting this limit in Equation (3.7) yields

$$\Psi(\tau = \tau_0[1 \pm \cos\theta] \mp \epsilon) = \frac{1}{\sqrt{2\tau_0\epsilon\cos\phi - \epsilon^2}} \tag{3.9}$$

after cancelling out identical terms. We note that the second term in the square root is negligible due to the smallness of ϵ. Integrating Equation (3.9) is analytically possible, yielding a finite result. However, for the sake of simplicity we have chosen simply to set all infinite values of the transfer function to zero in our simulations. Doing so does not change our analysis significantly, since we only change finite valued end points. We are also aware that the transfer functions we are considering represent idealistic, physically improbable systems. Finally, the main interest is in investigating Javelin's ability to recover time lags for light curves whose transfer functions differ from a top-hat function, a criterion which is satisfied regardless of the exact values of the end points of the transfer function.

Moving on to a system where the BLR is an infinitesimally thin sphere, we can make use of the result of the edge-on ring. However, what used to be points along a circle now need to be expanded into full rings to obtain a sphere. We do this by multiplying Equation (3.5) by a circular area of emission at each pair of points along the ring. With reference to Figure 3.6 we see that the area of an infinitesimal portion of a sphere is given by

$$\mathrm{d}A = r^2 \sin\theta\ \mathrm{d}\theta\ \mathrm{d}\phi. \tag{3.10}$$

The system is symmetric around the angle ϕ, and we may integrate over this parameter. This yields

$$\mathrm{d}A = r^2 \sin\theta\ \mathrm{d}\theta \int_{\phi=0}^{2\pi} \mathrm{d}\phi = 2\pi r^2 \sin\theta\ \mathrm{d}\theta. \tag{3.11}$$

The area of an annulus will be given by the area between two angles θ and $\theta + \mathrm{d}\theta$, giving

$$\begin{aligned}\mathrm{d}A &= 2\pi r^2 \int_{\theta}^{\theta+\mathrm{d}\theta} \sin\theta\ \mathrm{d}\theta \\ &= 2\pi r^2\ [-\cos\theta]_{\theta}^{\theta+\mathrm{d}\theta} \\ &= 2\pi r^2 [\cos\theta - \cos(\theta + \mathrm{d}\theta)]. \end{aligned} \tag{3.12}$$

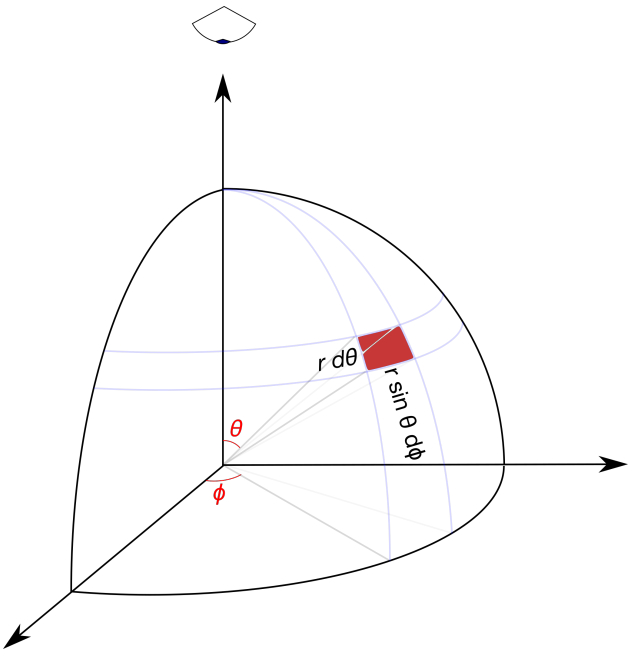

FIGURE 3.6: Geometry of a sphere, where the observer is looking down along the z-axis. Any infinitesimal area on the sphere may be expressed in terms of the angles θ and ϕ. There is a rotational symmetry around angle ϕ for the observer, such that any point along a given angle θ is at the same distance from the observer.

Using small angle approximation, the latter cosine term may be written

$$\cos(\theta + \mathrm{d}\theta) = \cos\theta\cos\mathrm{d}\theta - \sin\theta\sin\mathrm{d}\theta = \cos\theta \cdot 1 - \sin\theta\ \mathrm{d}\theta, \tag{3.13}$$

yielding

$$\begin{aligned}
\mathrm{d}A &= 2\pi r^2[\cos\theta + \sin\theta\ \mathrm{d}\theta - \cos\theta] \\
&= 2\pi r^2 \sin\theta\ \mathrm{d}\theta \\
&= 2\pi r^2\sqrt{1-\cos^2\theta}\ \mathrm{d}\theta \\
&= 2\pi r^2\sqrt{1-\left(1-\frac{\tau}{\tau_0}\right)^2}\ \mathrm{d}\theta \\
&= 2\pi r^2\sqrt{1-1+\frac{2\tau}{\tau_0}-\frac{\tau^2}{\tau_0^2}}\ \mathrm{d}\theta \\
&= 2\pi r^2\sqrt{\frac{\tau}{\tau_0}\left(2-\frac{\tau}{\tau_0}\right)}\ \mathrm{d}\theta,
\end{aligned} \tag{3.14}$$

where Equation (3.4) has been inserted to remove the cosine term. Multiplying together Equation (3.5) and Equation (3.14) gives

$$\Psi(\tau) = 2\pi\tau_0^2\sqrt{\frac{\tau}{\tau_0}\left(2-\frac{\tau}{\tau_0}\right)}\frac{1}{\sqrt{\tau(2\tau_0-\tau)}} = 2\pi\tau_0\frac{\sqrt{\tau(2\tau_0-\tau)}}{\sqrt{\tau(2\tau_0-\tau)}} = 2\pi\tau_0. \tag{3.15}$$

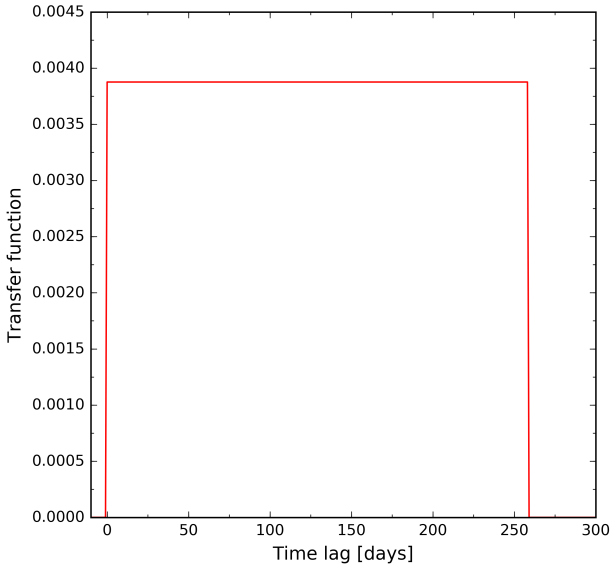

Figure 3.7: Transfer function for an infinitesimally thin spherical BLR distribution, centred at $\tau_0 = 129$ days. We recognise this transfer function as a top-hat transfer function of width $2\tau_0$.

In other words, the transfer function has a constant value of $2\pi\tau_0$ for all lags corresponding to the extent of the sphere, and equals to zero all other places. We recognise this as a top-hat transfer function with width twice the radius of the sphere, as shown in Figure 3.7. In performing the multiplication in Equation (3.15), we also recognise that the true expression for the transfer function is

$$\Psi(\tau) = \frac{\mathrm{d}A}{\mathrm{d}\tau}, \tag{3.16}$$

where we used the chain rule

$$\Psi(\tau) = \frac{\mathrm{d}A}{\mathrm{d}\theta}\frac{\mathrm{d}\theta}{\mathrm{d}\tau}. \tag{3.17}$$

This also agrees with $\Psi = \mathrm{d}\theta/\mathrm{d}\tau$ for the case of the rings, as $\mathrm{d}A/\mathrm{d}\theta = 1$ for the infinitesimally thin rings.

In addition to the geometrically motivated transfer functions, we also consider transfer functions based on the normal, or Gaussian, and Gamma distributions. These are shown in Figure 3.8. The Gaussian distribution is given by

$$\Psi(\tau) = \frac{1}{\sqrt{2\pi\sigma^2}} \exp\left\{-\frac{(\tau-\tau_0)^2}{2\sigma^2}\right\}, \tag{3.18}$$

and the Gamma distribution by

$$\Psi(\tau) = \frac{\beta^\alpha}{\Gamma(\alpha)}\tau^{\alpha-1}e^{-\beta\tau}, \tag{3.19}$$

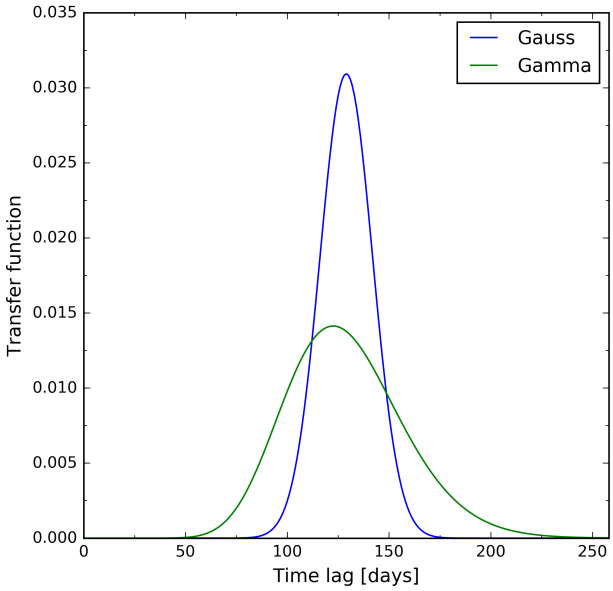

FIGURE 3.8: Transfer functions based on the Gauss and Gamma distributions. The defining parameters of the distributions are chosen to have values of $\sigma = \tau_0/10$ for the normal distribution, and $\alpha = 20$ and $\beta = \alpha/\tau_0$ for the Gamma distribution.

where $\Gamma(\alpha)$ is the gamma function

$$\Gamma(n) = (n-1)! \tag{3.20}$$

for a positive integer n, or

$$\Gamma(t) = \int_0^\infty x^{t-1} e^{-x}\, \mathrm{d}x \tag{3.21}$$

more generally.

3.2 JAVELIN's Response to Various Transfer Functions

One of the concerns about using JAVELIN to estimate AGN time lags is the fact that it assumes that the emission line light curve is obtained by convolving the continuum light curve with a top-hat transfer function, when the true shape of the transfer function is unknown. To test the robustness of JAVELIN, we create emission line light curves using a number of different transfer functions, and inspect the time lag estimates obtained by JAVELIN. Only if the estimates are reliable despite the transfer function taking other shapes can we be sure that JAVELIN is a good tool for time lag estimation of true data, for which transfer function is unknown.

We make use of all transfer functions described in Section 3.1, except for that based on a face-on ring with infinitesimal width, and create emission line light curves by convolving continuum line light curves with the various transfer functions. This process is performed 1000 times for each transfer function, using the same parameters to describe the AGN each

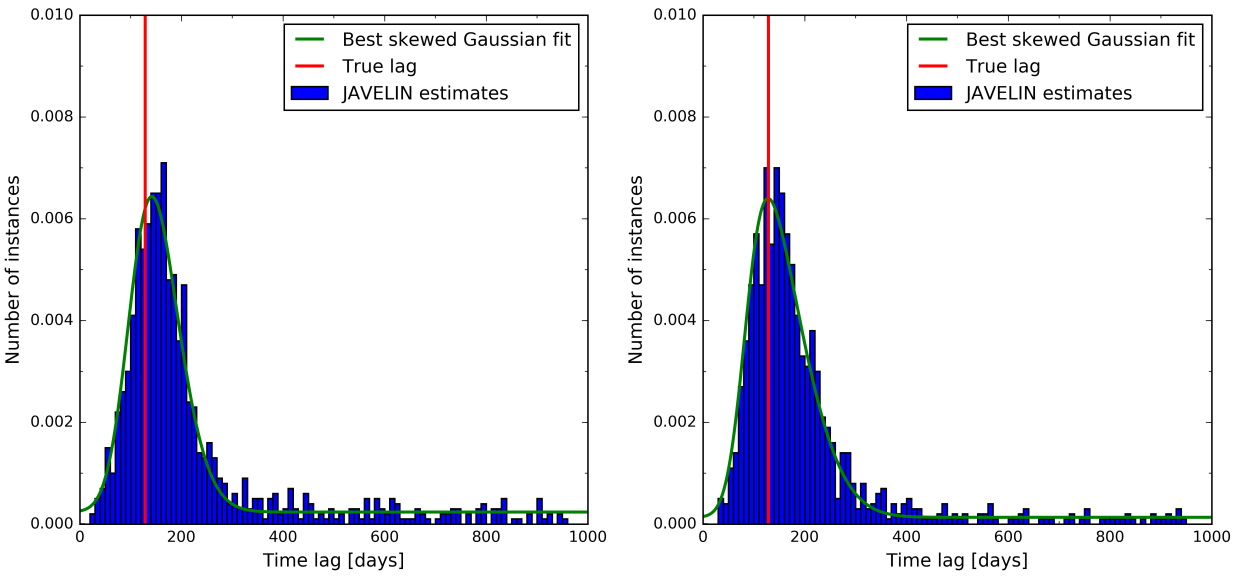

(a) Face-on disk.

(b) Sphere.

Figure 3.9: Normalised histograms showing the distributions of the best time lag estimates Javelin finds for 1000 different realisations of the same AGN, whose time lag is $\tau_0 = 129$ days. The figures are different in that they represent systems where two different transfer functions have been used; the left being based on a face-on disk extending 12.9 light days to each side of the 129 light day mark, the right based on an infinitesimally thin, spherical distribution of clouds 129 light days from the BH. The histograms clearly show that Javelin prefers time lags close to the true, underlying value most of the time for both systems.

time. We choose an AGN with an observed time lag of $\tau_0 = 129$ days, and the remaining parameter values chosen such that the AGN is one we realistically could observe with DES/OzDES. We record the time lag estimates provided by Javelin for each realisation, and estimate a time lag for the AGN described by a given transfer function based on all the individual realisations. The estimates were found in two separate ways. For the first, we binned all the estimates in terms of time lag, fitted a skewed Gaussian to the histograms, and used this distribution as a likelihood function to find the maximum likelihood time lag estimate with uncertainties. For the second procedure, we simply calculated the median with its uncertainty estimates based on the Javelin time lag estimates.

In Section 3.1 we showed how a face-on disk and an infinitesimally thin, spherical distribution of BLR clouds both result in top-hat transfer functions. We start by analysing Javelin's abilities using these transfer functions, as they represent the expectations of the program. The width of the face-on disk top-hat transfer function is chosen to be 20% of the time lag, so the BLR extends 12.9 light days on each of the side of the 129 light day mark. As for the sphere, the top-hat transfer function has a width of two times the time lag, according to the calculations in Section 3.1. Figure 3.9 shows the normalised distributions of time lags as estimated by Javelin for the face-on disk and infinitesimally thin sphere. The solid, green curves show the skewed Gaussian fit to the distributions, and the true time lag of the simulated AGN is indicated by the red, vertical line. For the face-on disk, the time

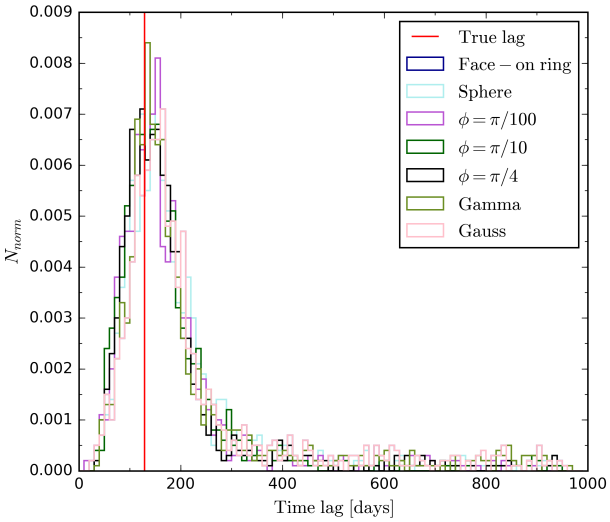

FIGURE 3.10: We present here the normalised histograms showing the distribution of time lags for all the transfer functions we have considered in our analysis. The normalisation is performed such that the area under each curve equals to one. The transfer functions we used for this analysis included simple, geometrically motivated distributions of clouds, as well as transfer functions simply based on known probability distributions. Despite the shape of the transfer functions varying significantly, we see in this Figure that the estimates provided by JAVELIN are all very similar, suggesting that JAVELIN is not very sensitive to the transfer function. This is a very good quality of the program, as it will be used for data whose underlying transfer function is unknown.

lag is estimated to be

$$\tau_{\mathrm{ML}} = 142^{+79}_{-65} \text{ days} \qquad \text{and} \qquad \tau_{\mathrm{med}} = 165^{+147}_{-53} \text{ days}$$

using the maximum likelihood and median estimation methods, respectively. The corresponding estimates are

$$\tau_{\mathrm{ML}} = 128^{+83}_{-53} \text{ days} \qquad \text{and} \qquad \tau_{\mathrm{med}} = 158^{+102}_{-55} \text{ days}$$

for the sphere. Clearly, the true time lag value lies well within the uncertainties for these estimates. In other words, JAVELIN performs well for these transfer functions, even with the strong smoothing occurring when the transfer function is twice the width of the lag.

In our analysis we find that JAVELIN performs well not only for the top-hat transfer function based light curves, but for all of them. To illustrate this we plot all histograms, including those shown in Figure 3.9, together. The complete set of time lag estimate histograms is shown in Figure 3.10.

In addition to the top-hat transfer functions, the other geometrically motivated transfer functions are those based on infinitesimally thin rings of various inclinations. We consider four special cases; $\phi = \pi/4$, $\phi = \pi/10$, $\phi = \pi/100$, and the edge-on ring ($\phi = 0$). The transfer function based on the edge-on ring leads to numerical issues for JAVELIN, and we choose to instead focus on the results for the other inclinations. This is because the

results for the edge-on ring do not represent the physical conditions of the system, and we are able to see the limiting behaviour of such as system by allowing the inclination of the ring to approach $\phi = 0$, without actually reaching this value. Moreover, the probability of observing an AGN with a disk which is exactly edge-on is obviously low. In fact, it is actually impossible to observe such a system in real life, because the AGN will be obscured by the torus if viewed edge-on (recall AGN anatomy illustrated in Figure 1.2). The distributions of time lag estimates by Javelin for the physically relevant cases are to be seen in Figure 3.10. They are all similar to each other, centring around the the true value of the time lag. The estimates for the $\phi = \pi/4$, $\phi = \pi/10$, and $\phi = \pi/100$ cases are

$$\tau_{\mathrm{ML}} = 129^{+72}_{-56} \text{ days} \qquad \text{and} \qquad \tau_{\mathrm{med}} = 151^{+83}_{-56} \text{ days},$$
$$\tau_{\mathrm{ML}} = 129^{+70}_{-57} \text{ days} \qquad \text{and} \qquad \tau_{\mathrm{med}} = 151^{+84}_{-55} \text{ days},$$

and

$$\tau_{\mathrm{ML}} = 127^{+69}_{-54} \text{ days} \qquad \text{and} \qquad \tau_{\mathrm{med}} = 151^{+82}_{-52} \text{ days},$$

respectively. Obviously, the maximum likelihood estimates are completely on point, and while the median overestimates the time lag, the true value is still contained within the median uncertainties.

Finally, we also make use of the Gauss and Gamma distributions for our transfer functions. We choose to define the normal distribution by a mean of $\tau_0 = 129$ days and a standard deviation of 10% of the lag; $\sigma = 12.9$ days. For the Gamma distribution we choose $\alpha = 20$, and $\beta = \alpha/\tau_0$, knowing that the mean of the distribution is given by $E\{\tau\} = \alpha/\beta$. The distributions of Javelin's time lag estimates for these non-geometrically inspired transfer functions are also to be seen in Figure 3.10. For the transfer function based on the normal distribution, the estimates for the 1000 realisations are

$$\tau_{\mathrm{ML}} = 138^{+84}_{-59} \text{ days} \qquad \text{and} \qquad \tau_{\mathrm{med}} = 166^{+147}_{-54} \text{ days},$$

and for the Gamma distribution

$$\tau_{\mathrm{ML}} = 133^{+75}_{-56} \text{ days} \qquad \text{and} \qquad \tau_{\mathrm{med}} = 158^{+135}_{-50} \text{ days}.$$

Again the estimates are good, and the true value is well within the uncertainties of the estimates.

Figure 3.11 summarises the estimates for the different transfer functions we have discussed. Both the maximum likelihood and the median allow us to estimate the time lag with a precision covering the underlying AGN time lag. The maximum likelihood turns out to be the most accurate method of estimating the time lags in this case. This is understandable when considering Figure 3.10 and the algorithm inside Javelin. Javelin is allowed to explore time lags ranging between $\tau = 0$ days to $\tau = 1000$ days. While the majority of the program's estimates will be close to the true time lag value when the program is working well, sometimes choosing incorrect values is unavoidable, especially with a large number of experiments. In this case, the number of experiments was 1000, allowing the program to sometimes end up deciding on time lags deviating from the true value. Since the true time

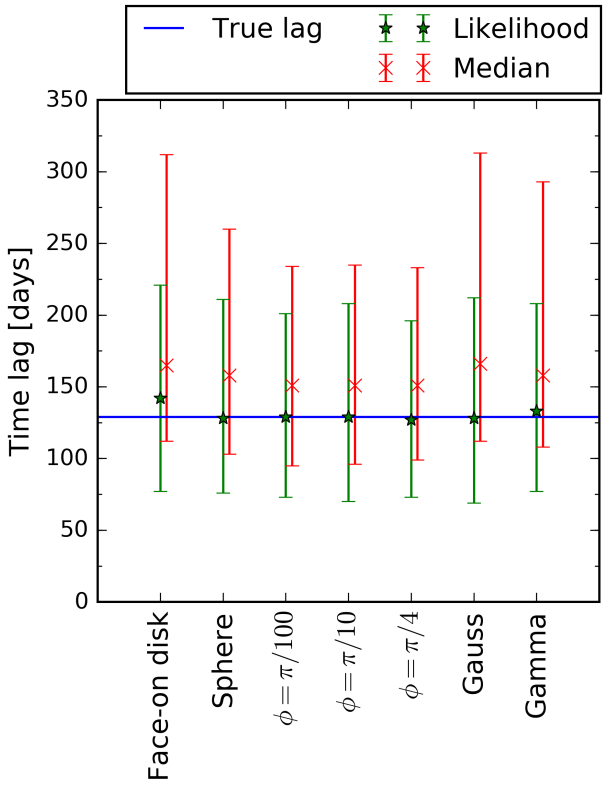

FIGURE 3.11: Collection of time lag estimates based on 1000 realisations of a single AGN with time lag $\tau_0 = 129$ days. Seven different transfer functions are been applied to the continuum light curve to obtain an emission line light curve to compare with; five of them based on geometric arguments. The geometric system (face-on disk with width 20% of the BLR size, infinitesimally thin sphere, and infinitesimally thin rings of three different inclinations) or distribution on which the transfer function is based is indicated along the x-axis.

lag is $\tau = 129$ days, there is a much larger area to explore and mistakenly choose on the higher lag range, thus dragging the value of the median in that direction.

The time lag estimate with the lowest precision is based on the face-on disk; a top-hat transfer function with a width equalling to 20% of the AGN time lag. This may look like a surprising result, since JAVELIN assumes a top-hat transfer function. However, when considering Figure 3.9a, we see that the distribution centres very well around the true value; indeed, the true value is within the uncertainty of the estimate. This suggests that there is no need for reading into the poorness of the estimate for this particular transfer function. The lower accuracy is more likely to be due to a statistical anomaly than to real, physical or numerical effects. Considering the estimates in Figure 3.11 we can draw the conclusion that JAVELIN is a robust program, capable of estimating time lag values well, even when the emission line light curve, to which the continuum light curve is compared, must be described by a transfer function different from the top-hat function assumed by the program.

4 Stacking

We have established reverberation mapping as a method of probing the innermost regions of AGN, and that JAVELIN is a useful tool for this purpose. However, in order perform reverberation mapping, observational data first need to be gathered. It is the observational process which is especially expensive and time consuming, both due to the intrinsic length of the lags we are attempting to measure, as well as the time dilation of the lags due to the expansion of the universe. Not surprisingly, there has been interest in finding alternative, more efficient ways of performing reverberation mapping observations. In this Chapter we present some of the previous work in this field, as well as the procedure we have developed for DES/OzDES.

4.1 Stacked Reverberation Mapping

Making use of the progress in technology allows for time-resolved photometric surveys and multi-object spectrographs. This allows for reverberation mapping data to be collected for a number of AGN simultaneously instead of individual objects only. Still, the number of observations often needs to be very large in order to reliably recover AGN time lags by reverberation mapping. We expect to obtain similar time lag estimates for AGN with similar properties. More specifically, AGN with similar luminosities are expected to have similar time lags, based on the $R-L$ relationships. If should hence be possible to put together noisy, individual time lag estimates for similar AGN in order to increase the signal to noise ratio, and thus obtain a single statistically significant time lag estimate for said AGN sample.

Fine et al. (2012) made an important step forward for reverberation mapping when introducing the idea of utilising stacking to perform reverberation mapping in a statistical way. By making use of the cross-correlation between continuum and emission line light curves they showed that even an extremely low number of observations can be used for inferring AGN time lags if stacking is used. In particular, Fine et al. (2012) considered a case where

an AGN was observed for a year with 61 continuum measurements, and the number of emission line measurements were either 61 or two. When stacking the cross-covariance of 30 AGN with only two spectroscopic measurements in order to obtain a sample cross-covariance function, they found that the peak in the stacked cross-covariance function was located at the same time lag as the peak in the cross-covariance function for the well-sampled AGN scenario.

A year later, Fine et al. (2013) showed the first results of stacking analysis utilised on observed reverberation mapping data, obtained by the Panoramic Survey Telescope & Rapid Response System 1 (Pan-STARRS1) medium-deep survey. The Fine et al. (2012) method proved to be very useful, despite the concerns addressed in the article. Indeed, Fine et al. (2013) recognise peaks in the stacked cross-correlation function which are consistent with established reverberation mapping results performed on individual AGN. While the method and the results are still at an early stage, they clearly show good potential, waiting only to be implemented and further improved.

In an attempt to refine the method of Fine et al. (2012, 2013), Brewer & Elliott (2014) make use of Bayesian analysis whilst stacking simulated reverberation mapping data. They point out some of the weaknesses of the simple method presented by Fine et al. (2012), such as the lack of meaning of the width of the peak in the cross-correlation function. Brewer & Elliott (2014) choose to take a step away from the cross-correlation function, writing their own code based on similar assumptions as JAVELIN. In their stacking analysis they implement hyperparameters describing the distribution of the parameters deciding the value of the AGN lags. In mathematical terms, this is the special case of Bayesian analysis named hierarchical modelling. The hierarchical modelling allowed to estimate time lags in a way that the lag uncertainty could be separated from the intrinsic uncertainty due to lag diversity within the AGN sample.

4.2 Stacking with JAVELIN

It is important to note that stacking the light curves of individual AGN will not allow for sample analysis, even if the light curves are modified to be in the rest frame of each AGN. This is because the light curves are described by a (damped) random process, so even though every AGN was described by completely identical parameters, the light curves would still differ from each other. Indeed, if one was to monitor a single AGN over an extended period of time, the same variation patterns would not be found. For this reason it is necessary to stack the individual estimates obtained from the light curves, rather than the light curves themselves. In our work we have chosen to use JAVELIN as our tool for estimating AGN time lags, so we have needed to change the stacking procedure to suit our method. JAVELIN does not provide us with a cross-correlation function, and we have to instead think through what kind of input we give JAVELIN, and how the output should be used and interpreted.

While the cross-correlation method does not make any assumptions about the nature of the continuum or emission lines, it does not provide much statistical information. JAVELIN, on the other hand, assumes a damped random walk, and uses MCMC to estimate time lags. We are able to access the information used for the MCMC, giving us information about the time lags evaluated in the process, as well as the likelihoods for each step of each walker's

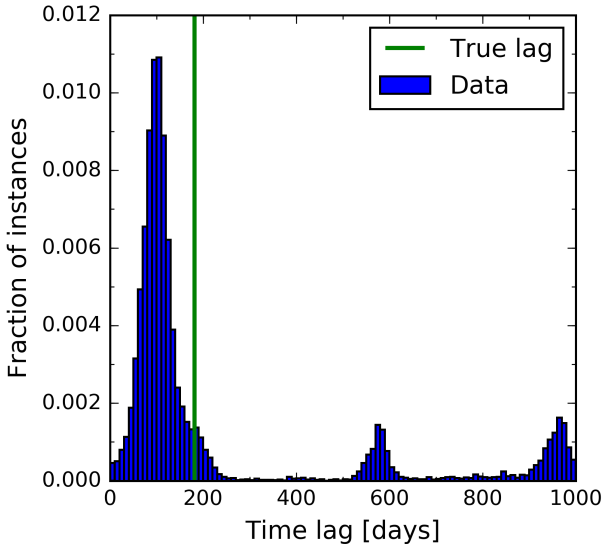

Figure 4.1: Example histogram showing the distribution of lags considered by Javelin for one run of the program. The histogram has several peaks, but the most significant one is somewhat close to the true value of the lag for the AGN in question. The strong peak shows that the MCMC section of Javelin in this case successfully has converged towards fluctuating around one time lag value, although somewhat offest from the true value of the lag.

chain. If one bins the time lags considered by Javelin during the MCMC according to their length, one can obtain a distribution showing how many times the different values are considered. If the MCMC process is successful, the chains should fluctuate around the correct value, so the time lag of the AGN should be close to the peak of this kind of histogram. In Figure 4.1 we present a normalised histogram of the time lags considered by Javelin for one run of the program. The peak of the histogram is somewhat close to the true lag value of the AGN. It is tempting to attempt stacking by averaging over the individual histograms of each AGN. However, such a procedure does not result in particularly good time lag estimates, nor is it statistically valid.

4.2.1 A Good Stacking Procedure

A good outline of a statistically valid stacking procedure is presented by Brewer & Elliott (2014). We make use of their method for our stacking purposes, but stick to the simpler Bayesian method without implementing hierarchical modelling. In general, Bayesian statistics dictates we have a sample of N objects, each of which may be described by a parameter θ_i. In our case, the sample is of AGN, and the describing parameter is the lag τ_i of the AGN. Given a set of data $\{x_i\}$, the posterior distribution describing each of the parameters θ_i is given by

$$p(\theta_i|x_i) \propto p(\theta_i)p(x_i|\theta_i), \tag{4.1}$$

where $p(\theta_i)$ is the prior distribution, and $p(x_i|\theta_i)$ is the likelihood function. Brewer & Elliott (2014) move on by introducing hyperparameters α which describe the distribution of the

parameters $\{\theta_i\}$. The joint probability distribution of α and $\{\theta_i\}$ is

$$p(\alpha, \{\theta_i\}) = p(\alpha) \prod_{i=1}^{N} p(\theta_i|\alpha). \tag{4.2}$$

For the sake of simplicity, we have chosen to assume that the lags of all the AGN we stack are identical, despite knowing that this will not be the case for real AGN. Assuming identical time lags is equivalent to setting the probability distribution of the hyperparameters to a δ-function, leading to the joint probability distribution to simply be a product of the prior probability distributions of the lags. By choosing the probability distribution of the hyperparameters to be a δ-function, we also reduce the hierarchical modelling to the simpler case of the "regular" Bayesian method. The posterior distribution for all the lags (and hyperparameters, if you wish) is

$$p(\alpha, \{\theta_i\}|\{x_i\}) \propto p(\alpha, \{\theta_i\}) p(\{x_i\}|\alpha, \{\theta_i\}) \tag{4.3}$$

$$p(\{\theta_i\}|\{x_i\}) \propto \prod_{i=1}^{N} p(\theta_i) p(x_i|\theta_i), \tag{4.4}$$

where we have simplified the notation by removing the hyperparameters in Equation (4.4), as they do not apply in our model. We have chosen to work with a simpler model merely due to its easier implementation, and because this research is at a very early stage. This limits our results in the sense that our estimates can only predict one time lag value with an uncertainty which does not reflect the variation within sample in question. Such an estimate is less informative than one which would be able to provide information about the intrinsic sample variance, which would be possible with a full hierarchical modelling analysis. In forthcoming research we will make use of the extensive analysis method.

It is worth spending some time understanding how the mathematics presented in this Section relates to what we actually do. We have already mentioned that we have set the distribution of the hyperparameters to be a δ-function, and that the parameters $\{\theta_i\}$ are the lags of each AGN. The data $\{x_i\}$ are the light curves of the continuum source and the emission lines. The likelihood function describes the distribution of data given there is a lag. Recall that the likelihood function $\mathcal{L}$ is strongly related to the χ^2 test,

$$\mathcal{L} \propto e^{-\chi^2/2}, \tag{4.5}$$

where χ^2 is calculated by

$$\chi^2 = \sum \left(\frac{\text{observation} - \text{theory}}{\text{error}} \right)^2. \tag{4.6}$$

In our case, JAVELIN gets information about the continuum light curve and emission line light curve. The combination of the two are the observations used by JAVELIN, and the theory they are being compared to is the fitted, continuous continuum light curve and an emission line light curve calculated by convolving the continuum light with a top-hat transfer function. JAVELIN computes the likelihood at each MCMC step, taking into account not

only the lag, but also the remaining parameters it is fitting for. The result is a distribution of likelihood values we may bin according to the time lag they correspond to. We have chosen to use the average value of the likelihood in every bin to represent the likelihood of that time lag. In addition, we require that the likelihood function should be smooth, and thus interpolate between lags where the bins ended up being empty. It is important to notice that when the likelihoods are computed, the prior distribution $p(\theta_i)$ has already been applied; we specify for Javelin boundaries within which the software is allowed to search for a time lag. This implies that the likelihoods will go to zero at the end points of the range we specified. Thus, what seemed to look like the likelihood function is actually the posterior probability distribution for each AGN, easily allowing to estimate the AGN's time lag.

For stacking purposes, the goal is of course to move past Equation (4.1), and compute the posterior distribution for all lags by Equation (4.4). We make use of the individual posterior distributions for each AGN, and multiply them by each other. To reduce the influence of outliers, we utilise bootstrapping (see e.g. Efron & Tibshirani, 1993) of the posterior distributions. In order to achieve a smooth posterior distribution of the lag for the AGN sample, we fit a polynomial to each of the individual posterior distributions in the region they are defined. We have found that a polynomial with a degree of 20 gives a good representation of the data, and results in final posterior distributions we can easily work with. The advantage of fitting a polynomial to the data is that it is defined at all points, making it easy to use the resulting function to compute the maximum likelihood, or median, with corresponding uncertainties for the time lag.

4.2.2 Choosing AGN With Similar Properties

It is important for us to stack the results of AGN with similar time lags. DES/OzDES consider a very large sample of AGN, varying over more than five magnitudes and over redshifts from $z \sim 0$ to $z = 4$ (King et al., 2015; Yuan et al., 2015), something which implies that a wide variety of AGN will be observed. As we will see, the time lags of the AGN in our sample can range from just a couple of weeks to more than a year in the rest frames of the AGN. It is therefore crucial to decide exactly which AGN should be binned together, so as to extract new knowledge from our observations. To treat several AGN as one, we obviously want the AGN in question to be as similar as possible to each other. In particular, we want the intrinsic lags of the AGN to be similar.

From the $R - L$ relationship we know that AGN of similar lags will have similar luminosities. One possible way to find such AGN is to group them according to similar redshift and apparent magnitude; if they appear to have the same brightness, and they are at similar distances, they must have a similar intrinsic brightness. This would be a very good way of grouping AGN, especially because it does not rely on any particular cosmology. However, it is uncertain whether DES/OzDES would have enough AGN measurements to allow for grouping like this. Moreover, the process of optimising the bin sizes would become difficult, as there would be a large number of parameters to change; the size of the redshift bin, the size of the apparent magnitude bin, and the number of AGN in each bin. Instead, we have chosen to instead look for AGN which have the same absolute magnitude. This removes the dependence on redshift, and simplifies the optimisation in two ways;

1. It is no longer necessary to vary the redshift as one of the parameters; a reduction in the number of free parameters to be constrained reduces the difficulty of any problem, and

2. We can make use of AGN with different redshifts within the same bin, allowing for a larger number of AGN to be stacked, and thus for better constraints on our recovered time lags.

The downside about using absolute magnitudes for grouping AGN is that it is not an observable value; it needs to be computed from the apparent magnitude and the redshift, with a certain cosmology assumed. A procedure where a cosmology is already assumed may seem counter-intuitive if the goal is to obtain results which are to teach us more about the cosmology of the Universe. However, this step is necessary to ease the grouping of AGN. In addition, if the assumed cosmology is incorrect, it should impact the results such that stacking will be less successful, since an incorrect cosmology will result in a wider variation of AGN time lags to be grouped together, thus resulting in poorer lag estimates.

It is necessary to remember that we want the AGN time lags to be similar in the rest frame of each AGN. To do so, we must reverse the time dilation due to the expansion of the universe. We do this by dividing the time intervals between all light curve measurements by said time dilation before using the light curves for anything. This way, JAVELIN can estimate the intrinsic time lags instead of the observed ones.

5
Perfect Scenario Stacking

To begin the stacking investigation we chose to look at some unrealistically good scenarios. We use JAVELIN to obtain time lag estimates for ten AGN at a time, and then utilise stacking of likelihoods to obtain time lag estimates for the AGN samples. We do this for two types of datasets, each with different subcategories. For the first dataset type we only make use of one light curve, but add in errors randomly to represent ten different measurements of the same light curve. To clarify, each light curve is created as a continuous function based on a damped random walk. We then pick out a number of points along the light curve according to the observation dates of DES/OzDES. We define a measurement uncertainty, and add in Gaussian errors to each measurement point. Adding in different errors for each realisation is physically equivalent to observing one AGN with ten different instruments. In the second case, we still make use of only one AGN, but allow the intrinsic light curves to vary. The second case thus represents several measurements of one AGN at different points in time. The errors added to the light curves to simulate measurement errors come in two flavours. In one case, we use errors of the size estimated for DES/OzDES measurements, and we refer to these as single errors. We also produce data with errors which on average are twice the size of the expected DES/OzDES errors, and refer to these as double errors. Mostly, we make use of sampling which is going to resemble that of DES/OzDES. At the end of this Chapter we do, however, also consider a good sampling scenario, in which we increase the number of measurements by a factor of ten, and allow the observations to be evenly spread throughout the duration of the survey, without introducing seasonal gaps. Finally, we make use of three types of AGN. Recall that any AGN is described by a small number of parameters; it's redshift z and magnitude (we use the apparent magnitude in the r-band, m_r), its lag, and the damped random walk parameters τ_D and SF_∞ described in Section 2.1.2. The first AGN was defined by

$$z = 0.1, \quad m_r = 18.53 \text{ mag}, \quad \tau_D = 618.0 \text{ days}, \quad S_F(\infty) = 0.28 \text{ mag}$$

with a time lag of

$$\tau_0 = 129.0 \text{ days},$$

the second with all parameters as above, except for

$$\tau_0 = 375.0 \text{ days},$$

and the last by

$$z = 3.1, \quad m_r = 19.1 \text{ mag}, \quad \tau_D = 850.0 \text{ days}, \quad S_F(\infty) = 0.145 \text{ mag}$$

with a time lag of

$$\tau_0 = 375.0 \text{ days}.$$

We choose an AGN with a time lag close to 365 days because King et al. (2015) show that we expect the most successful time lag recoveries for DES/OzDES to be for AGN with lags of approximately a year. For comparison purposes we also choose a shorter time lag, as well as the physically unrealistic AGN with a long time lag, but with the other parameters more representative of an AGN with a short time lag.

For each AGN, measurement type (intrinsically identical or different light curves), and measurement uncertainty flavour (single or double errors), we create ten measured light curve realisations, each of which is analysed by JAVELIN to find a time lag estimate. We make use of the likelihoods, or posterior distributions, obtained from JAVELIN as described in Section 4.2.1, and estimate time lags with corresponding uncertainties for each AGN using the posterior distribution to compute the maximum likelihood and the median. We stack the ten realisations from each subcategory to find the time lag estimate for each AGN sample. We create a single realisation with a good sampling for each measurement uncertainty flavour, to which the stacked estimates are compared. We hypothesise that:

1. The stacked time lag recoveries will be superior to the individual estimates,
2. The stacked time lag estimate for measurements with double errors will be comparable to, or better than, individual time lag recoveries with single errors, and
3. The stacked time lag estimates will be comparable to an individual time lag recovery with a similar number of spectroscopic epochs; for instance, stacking ten time lag recoveries based on 25 spectroscopic epochs will be equivalent to an individual time lag recovery based on 250 spectroscopic epochs.

5.1 Stacking of Intrinsically Identical Light Curves

We created data based on intrinsically identical light curves to which different random errors were added at each point in time. By adding different errors to each realisation, we obtained data which could represent different light curve measurements, even when the light curves we used were intrinsically identical. An example of the measured light curves for both

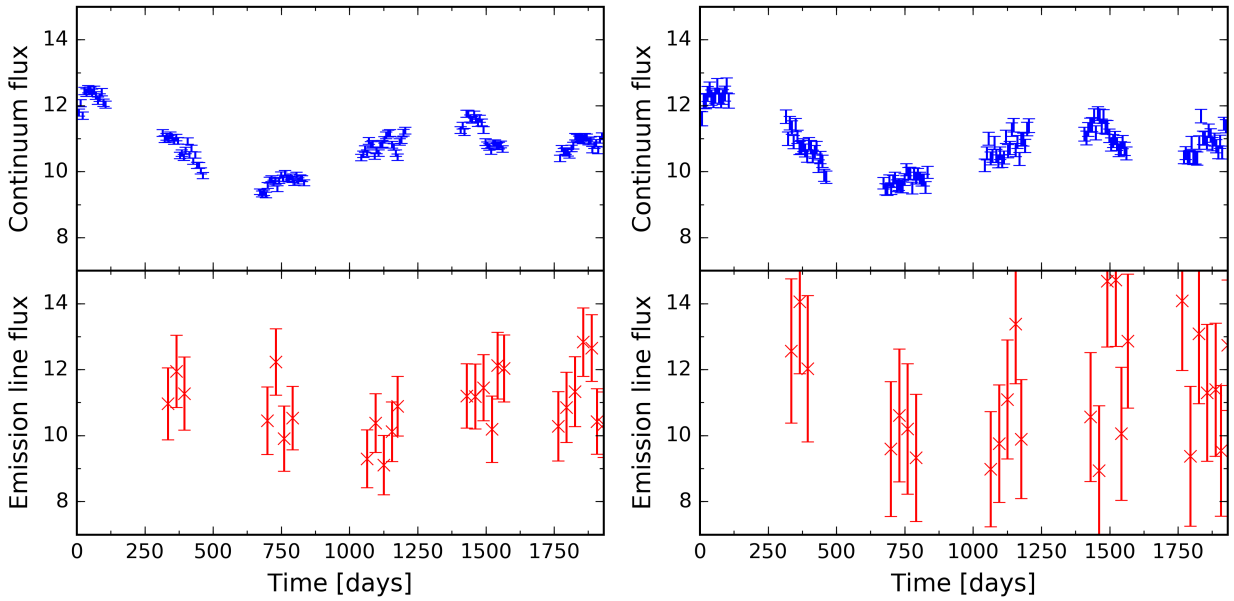

(a) Single errors.

(b) Double errors.

Figure 5.1: "Observed" light curves over the duration of DES/OzDES used for estimating time lags in the perfect stacking scenario where all light curves are identical. The underlying light curve is the same for both sub-figures, and the lag between the continuum and emission line light curve is 375 days. The left hand sub-figure has measurement errors the size we expect for DES/OzDES ("single errors"), the other errors which have twice as large a magnitude as what we expect ("double errors"). In the single error case, we recognise the same kind of trends in the continuum and emission line light curves by eye. For the double error case, the uncertainties are large enough that such a trend is difficult to spot.

measurement error sizes is to be seen in figure 5.1. The photometric light curve shows good variability, which is helpful for recovering time lags well. In the single error case, where the errors are based on DES/OzDES measurements, the same kind of variability is also seen in the spectroscopic measurements, although the uncertainties obviously are larger. When the errors are doubled, however, the photometric measurements still show a good light curve, whereas the spectroscopic data look more random, and it is harder to see the relationship to the photometric light curve.

Figure 5.2 shows examples of what the likelihood function, or posterior distribution (see Section 4.2.1), may look like; Figure 5.2a showing one example of the likelihood function for an individual AGN when investigated by Javelin, and Figure 5.2b when the likelihoods of ten AGN have been stacked to form the likelihood function for a group of similar AGN. Figure 5.2a shows that a 20 degree polynomial does fit the likelihood data obtained from Javelin well, but the time lag recovery is not particularly precise. When we stack the likelihoods of ten AGN, Figure 5.2b shows that the uncertainty decreases significantly.

The time recoveries for the intrinsically identical light curve scenario are shown in Figures 5.3 and 5.4. The plots on the left hand side of the Figures are based on single errors, and the ones on the right hand side on double errors. In addition to the results of ten

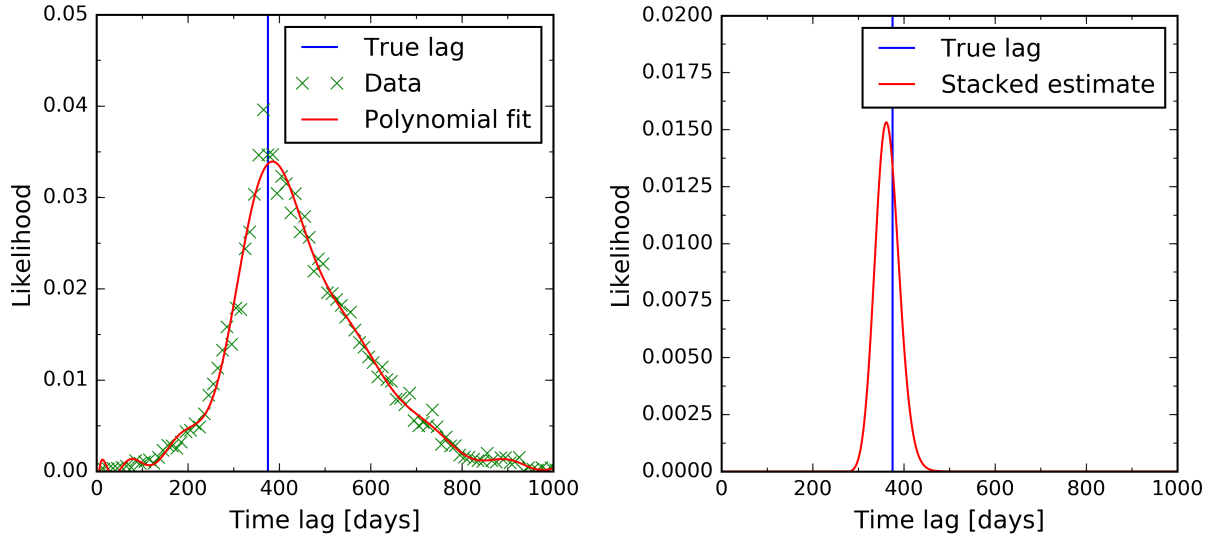

(a) Individual estimate.

(b) Stacked estimate.

FIGURE 5.2: Examples of likelihood function for time lag recoveries by JAVELIN, where the left hand sub-figure is based on a single AGN, and the right hand sub-figure is based on a stacking of ten noisy time lag recoveries. We stack the polynomial fits, rather than the data, as they are smoother, and the result becomes more stable. Clearly, stacking improves the estimate, leaving us with a more precise and hopefully also an overall more accurate estimate.

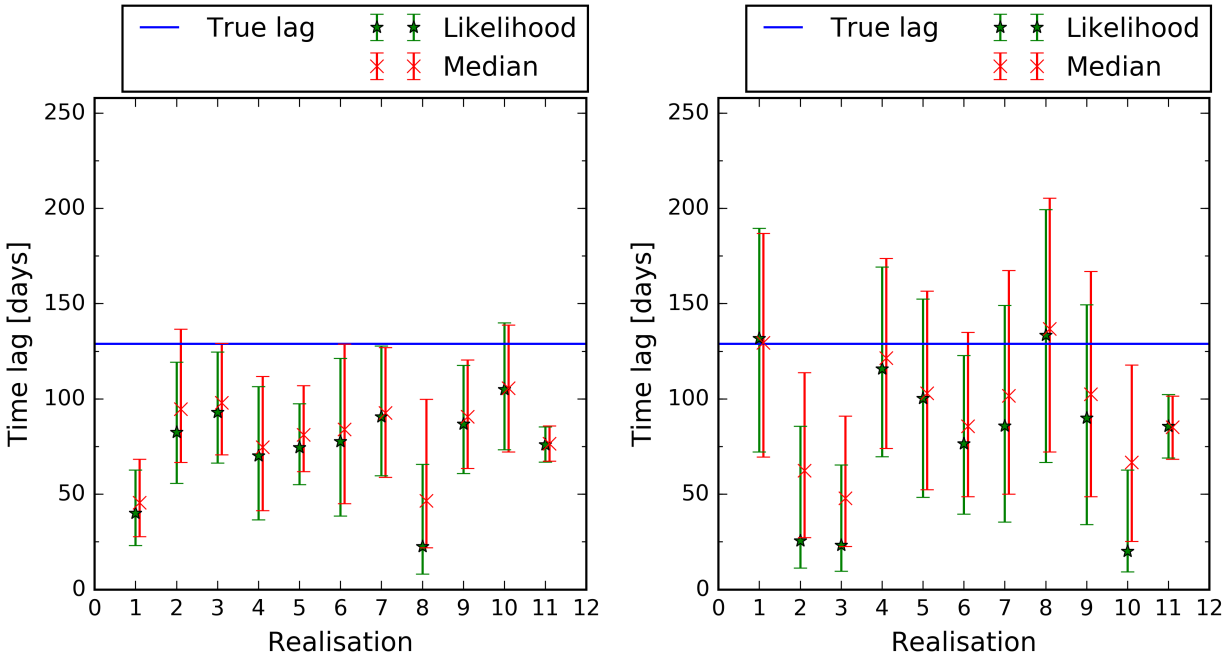

(a) Single errors.

(b) Double errors.

FIGURE 5.3: Time lag estimates for a perfect stacking scenario with ten intrinsically identical light curves. The time lag in this case was $\tau_0 = 129$ days. The eleventh point in each sub-figure represents the stacked time lag estimate. While the stacking clearly helps reducing the estimate uncertainty, both sub-figures show a tendency to underestimate the time lag. However, as we will see, this effect goes away when intrinsically different light curves are used.

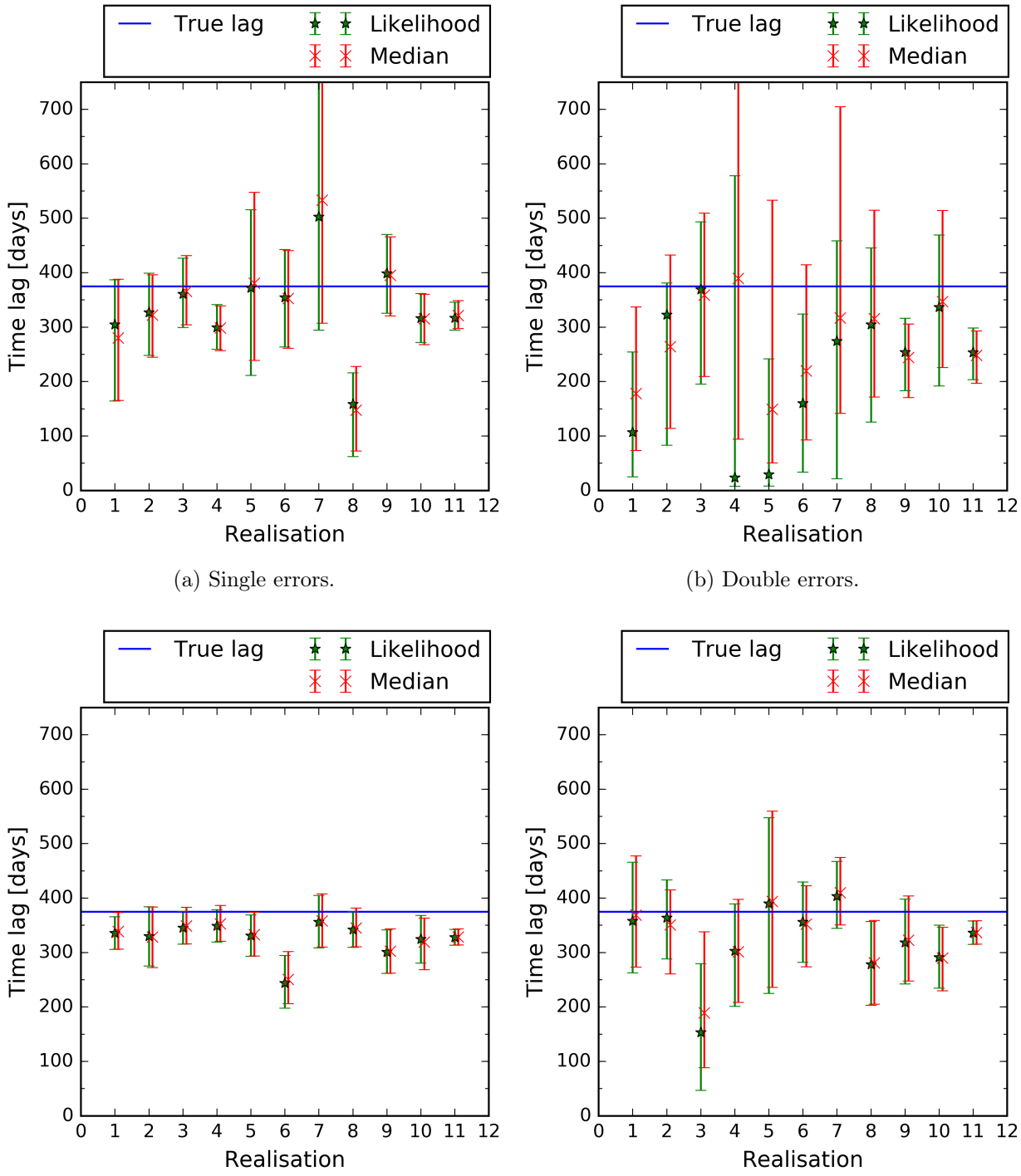

(a) Single errors.

(b) Double errors.

(c) Unrealistic AGN, single errors.

(d) Unrealistic AGN, double errors.

Figure 5.4: Time lag estimates for a perfect stacking scenario with ten intrinsically identical light curves. The time lag in this case was $\tau_0 = 375$ days. The eleventh point in each sub-figure represents the stacked time lag estimate. While the stacking clearly helps reducing the estimate uncertainty, both sub-figures show a tendency to underestimate the time lag, an effect which, as we will see, goes away when intrinsically different light curves are used.

individual realisations, an eleventh point is included. This point represents the stacked time lag recovery of the individual estimates. Both estimation types, the maximum likelihood and the median, are shown in the plots. The uncertainties in the plots represent the 1σ uncertainties of the estimates.

Figures 5.3 and 5.4 both show a trend for the time lags to be underestimated, rather than overestimated. This is particularly the case for Figure 5.3, where the underlying AGN time lag is $\tau_0 = 129$ days. We expect the reason for this bias to be the underlying light curve, which is the same for all of these estimates. This is because the underestimation is systematic, and the estimates all seem to fluctuate around one time lag, which simply is very roughly 1 or 2σ shorter than the one used in the simulation. Particular light curves will be prone to over- or underestimation of the lags, an effect which, as we will see, can be lowered. In Section 5.2 we show that the underestimation bias goes away when different light curves are used, and in Section 5.3 the time lag recovery is also more accurate when the light curves have a better sampling.

Figure 5.4 shows the recovery of time lag for AGN with longer lags; $\tau_0 = 375$ days. According to our expectations, the time lags are recovered best in the physically unrealistic scenario, something which can be seen when comparing Figures 5.4c and 5.4d to Figures 5.4a and 5.4b, as well as to Figure 5.3. The physically unrealistic scenario is that where the time lag is set to $\tau_0 = 375$ days, but the rest of the parameters describe an AGN which is physically more inclined to have a short – for instance $\tau_0 = 129$ days – time lag. This is certainly unfortunate, since it obviously would have been good to recover time lags with a precision like this, but the probability of finding such an AGN is very slim indeed. The reason why this unrealistic scenario recovers the time lags best can be summarised as follows: Recalling that the variability of an AGN is described by Equation (2.11), it follows that smaller values of τ_D and higher values of SF_∞ lead to more variable AGN. A more variable source allows for easier time lag estimation, giving the unrealistic AGN an advantage over the realistic 375 day time lag AGN. On the other hand, time lags closer to a year are the easiest to estimate, this time giving the unrealistic AGN advantage over that with a 129 day time lag. Combined, this allows for the physically unrealistic AGN to recover its time lag far better than the physically realistic AGN.

It is natural to expect that higher noise levels will complicate an estimation process, resulting in poorer time lag recoveries for the double error scenarios compared to the single error scenarios. It also seems intuitive that more measurements will allow to increase the signal-to-noise ratio. To see whether this hypothesis upholds, we stack the individual posterior distributions obtained from JAVELIN to obtain a time lag recovery for a group of AGN. We expect the stacked time lag recovery for a double error scenario to be better than the individual double error time lag recoveries, and that it will be comparable to, or better than, the individual time lag recoveries for a single error scenario. Based on Figures 5.3 and 5.4, it seems that the expected improvement due to stacking is achieved. The stacked time lag recoveries are generally a clear improvement to the individual estimates. For the double error data sets, the stacked time lag recoveries are mostly comparable to, or even better than, some of the individual results for the single error dataset. A positive stacking effect like this is very promising for the future of DES and OzDES.

5.2 Stacking of Intrinsically Different Light Curves

To further investigate the effects of applying stacking analysis to groups of similar AGN, we move on from stacking intrinsically identical light curves to light curves which are intrinsically different, but can potentially be observed for the same AGN at different points in time. We make use of the two physically realistic AGN mentioned previously, and make ten different light curves for each AGN and each noise level. The individual and stacked time lag recoveries are to be seen in Figure 5.5. We observe that when we make use of different light curves, many of the individual time lag estimates have larger uncertainties compared to the recovered time lags for various measurements of a single light curve. The decrease in precision can be explained by the fact that a good intrinsic light curve was intentionally chosen for the scenario with intrinsically identical light curves. When considering a number of different light curves, however, we accept light curves with various qualities, some of which result in poorer time lag recoveries.

Although the individual recovered time lags are poorer than in the intrinsically identical light curve scenario, the stacked results look promising when different light curves have been used. Compared to Figures 5.3 and 5.4 we see that Figure 5.5 shows a lower degree of bias towards underestimating (or overestimating) the lags. The lack of bias for the individual time lag recoveries also allows for the stacked time lag recovery to be more reliable. The reason for the bias reduction is most likely due to the variety of the underlying light curves, each of which can be prone to over- or underestimation of the time lag if the sampling is as sparse as for the DES/OzDES surveys. By stacking individual time lag recoveries which are scattered on both sides of the true time lag, a more reliable time lag can be recovered.

In our investigation of individual and stacked time lag recoveries based on light curves which have been both intrinsically different and identical we obtain very important results. First, we see that stacking of individual estimates yields time lag recoveries which are more precise than the individual estimates. This satisfies the first or the hypotheses we had at the beginning of this Chapter. Next, we see that by stacking time lag estimates based on light curves with large measurement errors and uncertainties we obtain a more reliable result, which is comparable to, or better than, an individual time lag recovery based on less noisy data. With this, the second of our hypotheses is satisfied. Finally, we also find that stacking of estimates based on different light curves is preferable to stacking of estimates based on light curves which are very similar. This is a very important result we are very happy to see, since we have developed this stacking analysis to apply it to data measured by DES/OzDES. When we do that, we will have to group together AGN which are somewhat different from each other, meaning that the light curves, too, will be different. Due to the scatter we obtain in individual estimates when using light curves which differ from each other, we can expect to recover time lags for our groups of AGN which are less prone to under- or overestimation bias.

5.3 Comparison to a Good Sampling Scenario

Fine et al. (2012) investigated the possibility of using stacking of correlation functions in order to make up for a poor sampling of light curves, finding stacking to be a successful

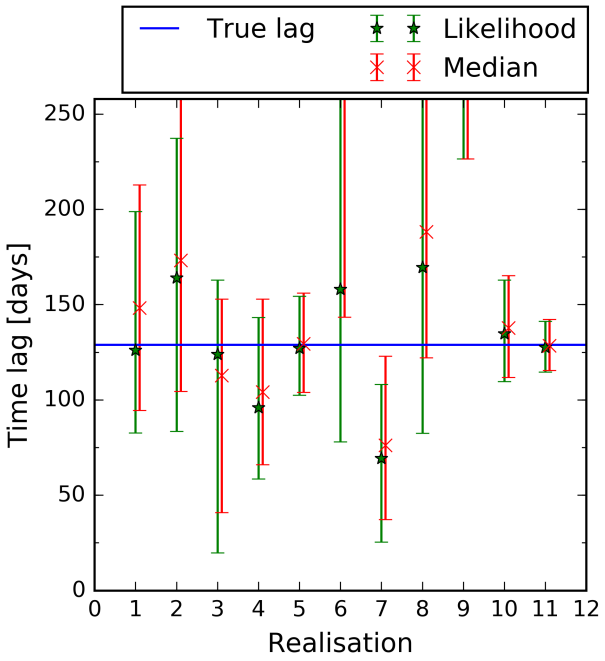

(a) Time lag $\tau_0 = 129$ days, single errors.

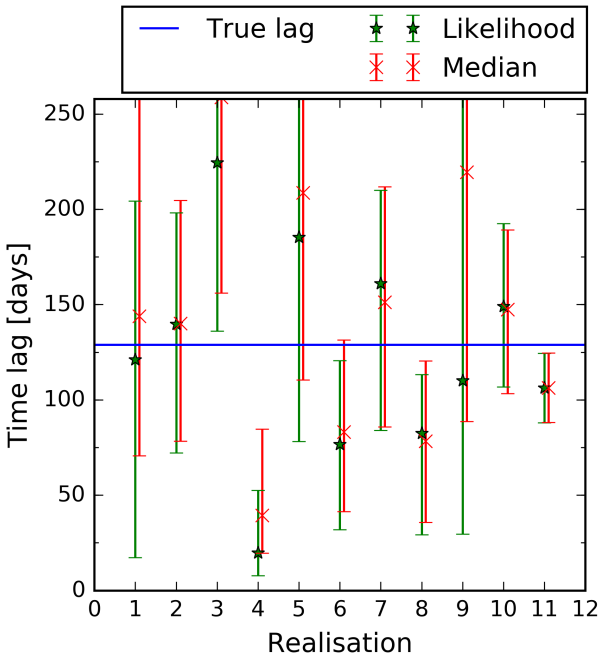

(b) Time lag $\tau_0 = 129$ days, double errors.

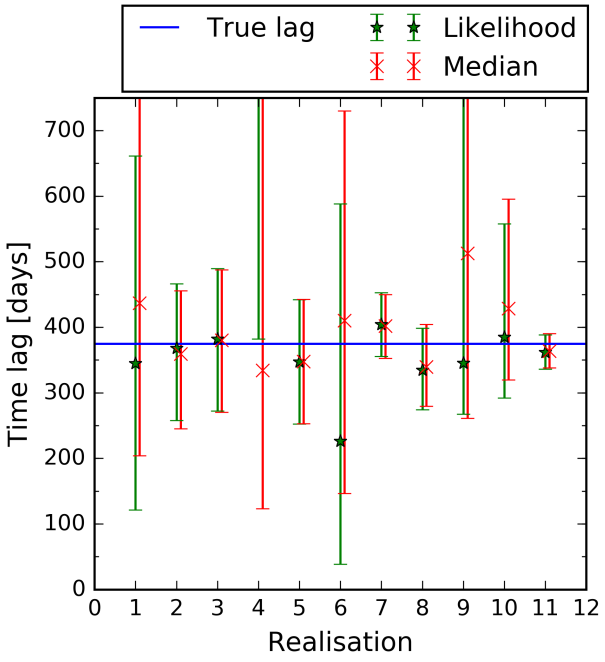

(c) Time lag $\tau_0 = 375$ days, single errors.

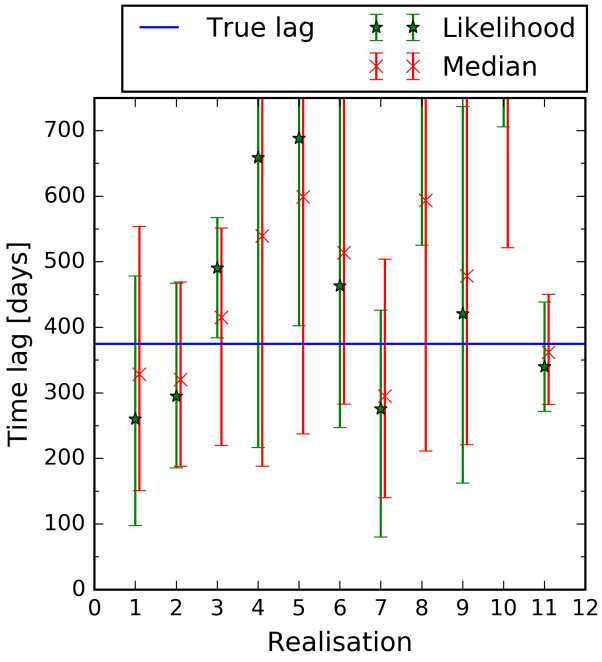

(d) Time lag $\tau_0 = 375$ days, double errors.

FIGURE 5.5: Time lag estimates for a perfect stacking scenario where ten different intrinsic light curves have been used. The eleventh point in each sub-figure represents the time lag estimate after stacking has been performed. Compared to Figures 5.3 and 5.4 the underestimation bias has disappeared, such that the lag estimates are more accurate in addition to being precise.

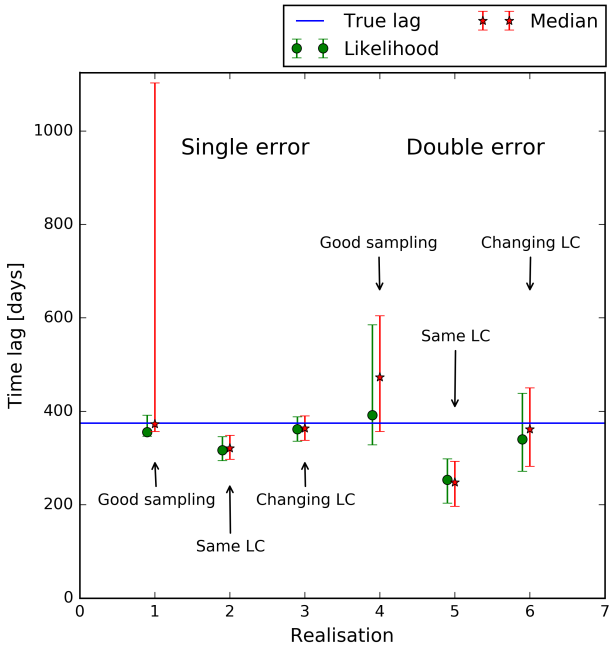

Figure 5.6: Comparison of a good sampling scenario with stacking results, inspired by Fine et al. (2012). The three leftmost realisations are based on "single errors"; the kind of measurements uncertainties of the light curve we expect based on DES/OzDES measurements. The three realisations to the right have been applied uncertainties which are twice the size we expect from DES/OzDES. Clearly, the single error case obtains more precise and accurate estimates than the double error case. The first realisation for each case is based on a single estimate with a sampling which is ten times what we can achieve with DES/OzDES. The two following realisations are based on the expected sampling for DES/OzDES. For the second realisation in each case we have made use of intrinsically identical light curves, and only changed the uncertainties for each measurement. The last realisation makes use of light curves which are intrinsically different, but still describing the same AGN. The stacking results are certainly comparable to the good sampling scenario, the latter of which is not possible to obtain for DES/OzDES. The good stacking results are very promising for our surveys.

tool. We now attempt recreating such positive stacking results, only using the Javelin method presented in Section 4.2 instead of correlation functions to recover the time lags. The scenario we consider is less extreme than that of Fine et al. (2012), who only used two measurements in each emission line light curve. We make use of the data already presented in this Chapter, and compare them to a sampling too frequent to be possible to achieve for DES/OzDES. In the good sampling scenario we have ten times as many photometric and spectroscopic measurements as DES/OzDES, and these are spread out evenly over the survey duration. The good sampling scenario cases are created for a realistic 375 day lag AGN, and compared to stacked estimates of corresponding time lag recoveries based on DES/OzDES sampling, presented in Sections 5.1 and 5.2.

In figure 5.6 we present the results of time lag estimates for well sampled light curves together with the stacked results discussed in Sections 5.1 and 5.2. We see that the stacking method is very successful, and very much comparable to, or even better than, the individual

time lag recoveries for good sampling scenarios. We are again reminded that the sample estimates are more accurate when the intrinsic light curves are different, a very promising result for DES/OzDES. The excellent time lag recoveries obtained by stacking represent an extremely important result, as they imply that we should be able to utilise stacking to make up for the poor sampling of DES/OzDES, yet still achieve results of high quality.

6 Realistic Scenario Stacking

In Chapter 5 we presented the results of utilising stacking of individual AGN time lag estimates to obtain a time lag recovery for a group of identical AGN; a perfect scenario. While such results are instructive, it is obviously of great importance to know how to best apply such a technique to observations from a specific survey. Our wish is to optimise the binning of AGN to suit the DES/OzDES data. We also wish to see whether we can make use of the three years' worth of data we already have. King et al. (2015) show that the number of successful individual time lag estimates at such an early stage will be limited. However, knowing that a stacked analysis is more likely too achieve reliable time lag recoveries than individual estimates, we see the potential of early time reverberation mapping results if optimised stacking can be applied to our data. In this Chapter, we therefore present the results of optimising binning of DES/OzDES AGN data for reverberation mapping purposes.

6.1 Binning AGN

As mentioned in Section 4.2, we bin AGN by their absolute magnitudes. As discussed in the same Section, working with absolute magnitudes forces us to make certain assumptions, more specifically about the cosmology of our Universe. We make use of the same cosmology as MacLeod et al. (2010) – ΛCDM with $\Omega_M = 0.30$, $\Omega_\Lambda = 0.70$, and $H_0 = 70$ km/s/Mpc – to utilise their method of defining τ_D and SF_∞. To simplify the computational process, we create AGN with their i-band absolute magnitude and redshift predefined, and use the assumed cosmology to calculate the apparent magnitude from them. When applying the stacking method to observational data, the code will have to be slightly modified, since the absolute magnitude of any object will be unknown. Instead, we will need to take in apparent magnitude and redshift as the observables, and calculate the absolute magnitude from them before assigning each AGN into their correct bins. Such a modification will, however, only be minor, and most of the programming to allow for it is already written and ready to be

implemented.

There are a number of ways one could go about optimising the binning of AGN. Regardless of method, it is important to consider the fact that the optimal bin sizes could change with the magnitude of the objects considered, due to the nature of the $R - L$ relationship. The $R - L$ relationship dictates

$$\tau_0 \propto \sqrt{L}, \tag{6.1}$$

which we equivalently may write as

$$\tau_0^2 = CL, \tag{6.2}$$

where C is a constant. We find C utilising the relationship between flux and luminosity presented in Equation (2.2), where we let the distance be the BLR radius;

$$r_{\text{BLR}}^2 = \frac{L}{4\pi F_c} \tag{6.3}$$

$$\tau_0^2 = \frac{L}{4\pi c^2 F_c} \equiv CL, \tag{6.4}$$

where c is the speed of light, and F_c is the flux necessary to ionise the BLR gas. Inserting this into the definition of absolute magnitude, we obtain

$$M - M_\odot = -2.5(\log L - \log L_\odot) \tag{6.5}$$

$$\log \frac{\tau_0^2}{C} = \log L_\odot + 0.4M_\odot - 0.4M \tag{6.6}$$

$$\tau_0 = \sqrt{\frac{L_\odot}{4\pi c^2 F_c}} e^{0.2M_\odot} e^{-0.2M} \equiv A e^{-0.2M}. \tag{6.7}$$

Here A is a value which is not necessarily constant, but is not going to vary such as to counteract the influence of the exponential in Equation (6.7). The nature of the time lag's dependency on the magnitude indicates that a change in the absolute magnitude will have a varying effect on the change in the time lag, depending on what the initial magnitude was. For this reason, optimisation of the AGN binning should be done as a function of the absolute magnitude, to the extent it is possible.

For a real life survey with a fixed number of objects, we know that there will be two opposing effects contributing to the goodness of time lag recoveries obtained by stacking. One the one hand, adding more objects to stack together should increase the signal-to-noise ratio, allowing for more precise estimates. It would hence be interesting to see how many objects are needed in order to obtain an uncertainty satisfying a predetermined criterion. On the other hand, we know that in order to obtain a greater number of objects in reality, we need to expand the size of our bins. Larger bins means more different AGN will be grouped together, something which inevitably will lead to poorer constraints on the time lag due to the intrinsic variation of time lags within the sample itself becoming larger. To test the optimal bin size on its own, one could keep the number of AGN constant, and increase the bin size until the intrinsic diversity becomes too large.

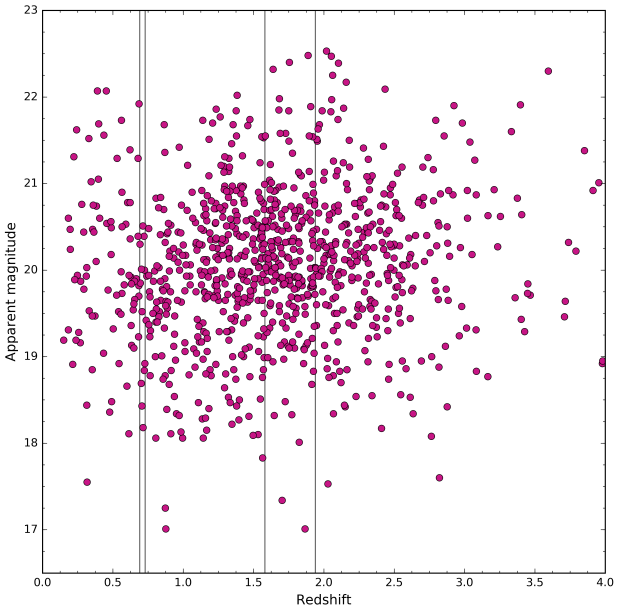

Figure 6.1: Distribution of AGN monitored by DES/OzDES for the reverberation mapping project. The vertical lines mark the redshifts at which a new emission line can be used, or can no longer be used. The distribution is here shown in terms of redshift and apparent magnitude, the observables for DES/OzDES. When performing stacking analysis, we instead consider the distribution in terms of absolute magnitude.

6.2 Optimising for the DES/OzDES Sample

Learning about the intrinsic optimal AGN binning for stacking analysis would most certainly be interesting. However, because the redshift and magnitude distribution of AGN monitored by DES/OzDES is known, we decide to tailor the optimisation for the AGN in our sample, portrayed in Figure 6.1, directly. Doing so saves a large amount of computational time, since we do not have to worry about whether the bin size or the number of AGN should be optimised first. It simplifies the task, allowing us to directly look at what the best solution for our surveys will be, rather than having to analyse the surveys to find out how to apply the general results.

Considering one emission line at a time, we choose ourselves an absolute magnitude to start at, and create a bin from there. We shift the other end of the magnitude bin to increase and decrease the size of the bin, including or excluding AGN dependent on how many AGN we know there are in such a bin based on the DES/OzDES sample. We calculate the average lag of the AGN in the sample, and analyse the intrinsic lag differences between the AGN. We make use of Javelin to estimate the individual time lag of each AGN based on a simulated three years' worth of observations, and stack the individual estimates in order to obtain a time lag recovery for the sample as a whole. We calculate the time lag estimate with uncertainties for the sample within the current bin, and compare it to the known average lag and intrinsic variation. We calculate the intrinsic variation by finding the standard deviation of the known time lags of the AGN in the bin. The uncertainty of the stacked time lag recovery is calculated using a maximum likelihood method, as well as using the median.

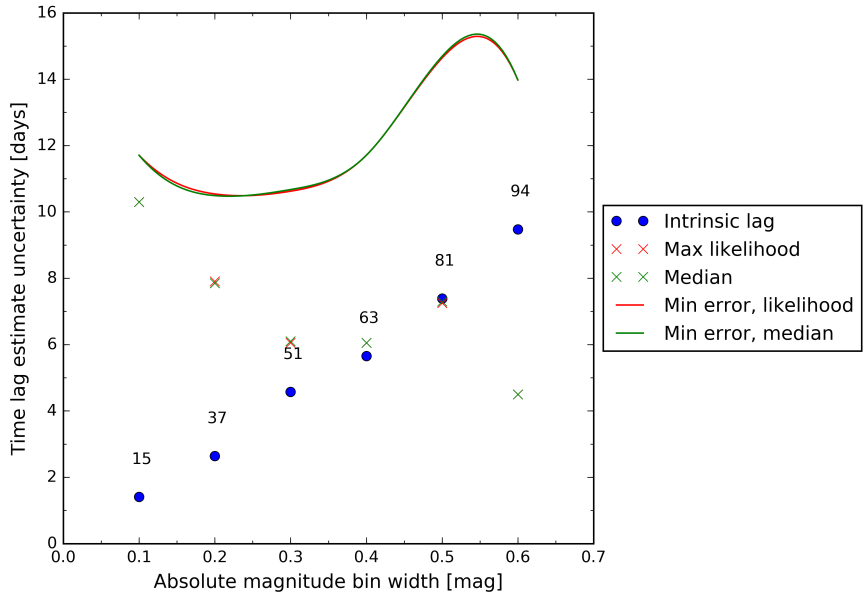

FIGURE 6.2: In this Figure we present the size of the standard deviation between lags in an AGN sample, marked with blue dots, together with the uncertainty of the stacked time lag recovery for the same AGN sample, marked by red and green crosses. By adding together the intrinsic variation and the estimate uncertainty, we can obtain uncertainty curves which we can use to find the bin size for which we can obtain the smallest total uncertainty.

Unlike the intrinsic variation, for which we assume a symmetric distribution of lags, the posterior distribution of the stacked time lag estimate can be asymmetric. This allows for the upper and lower uncertainty bounds to differ in value. We choose to use the average of the upper and lower uncertainty bounds to represent the lag estimate uncertainty within each bin to compare it to the intrinsic lag variation within the corresponding bin sample.

To find the optimal bin size for any sample of AGN, we need to consider both the intrinsic variation within the sample, as well as the uncertainty of the stacked estimate. One way of deciding on the best bin size is to add up the intrinsic variation together with the uncertainty of the stacked estimate, and find the bin size which corresponds to a minimum of the total uncertainty. Figure 6.2 shows an example of this procedure. In it, we show the uncertainty data by points, and overplot a curve obtained by adding together the uncertainties, interpolating between the points, and smoothing the result. Generally, we find that the sum of the uncertainties can fluctuate somewhat as a function of the bin width. More importantly, we find that the sum generally has a minimum at rather small bin widths – more specifically, the minimum occurs for bin widths where the uncertainty of the stacked time lag recovery is larger than the intrinsic variation within the AGN sample of the same bin. We decide to move away from the minimum uncertainty procedure in favour of choosing a bin size where the intrinsic variation and stacked estimate uncertainty are (approximately) the same. If we were to choose a bin width which led to the stacked estimate uncertainties being bigger than the intrinsic variation, then our estimates would be too imprecise to really say anything about the AGN sample. If, on the other hand, the intrinsic variation was to be larger than the uncertainty of the stacked estimate, the estimate would only reflect a sub-sample of the

AGN. By allowing the uncertainties to be the equal in size, the recovered time lag for the AGN sample as a whole reflects the lag of the true sample in the way we believe to be the most realistic.

6.3 Three Year Results

In Figures 6.3 and 6.4 we show examples of the analysis performed to optimise the bin sizes. In each sub-figure there are numbers above each set points, representing the number of AGN within that bin. Figures 6.3a, 6.3c and 6.4a show the average time lags of the AGN within the bins, and the stacked time lag estimates, together with the uncertainties for both. The average time lag value within an AGN bin is not constant as a function of the bin width. This is because a change in the bin size opens up for different time lags to change the mean lag of the sample. If the bin is expanded such that AGN with lower magnitudes are included, the average luminosity of the AGN in the sample increases, leading to a longer average time lag for the sample. Conversely, if AGN with higher magnitude values are included in the sample, the average time lag of the AGN becomes shorter. In Figures 6.3b, 6.3d and 6.4b we plot the magnitude of the uncertainties represented by the error bars in Figures 6.3a, 6.3c and 6.4a. For the stacked time lag recoveries, the error bars can by asymmetric, in which case we have taken the average of the higher and lower uncertainty limit. As expected, the true uncertainty for a sample (or, more correctly: the intrinsic variation of AGN lags within the bin) grows as a function of the bin size. This is because larger bin sizes imply more AGN are included, allowing for larger discrepancies between the AGN lags. The uncertainties for the stacked time lag recoveries also follow the expected behaviour, yielding more precise estimates when more AGN are included.

A surprising result of the optimisation is the size of the optimal bins. Based on Equation (6.7) we expect that the intrinsic lag variation within an AGN sample becomes larger if the magnitudes are lower, even if the bin size remains constant, and thus that the bin size may have to decrease with lower magnitudes. On the other hand, we are aware that if we stack more AGN we expect to obtain more precise estimates, so we could expect the bin sizes to be smaller for magnitudes where the AGN density is higher. However, our analysis shows that the preferred bin size is $\Delta M_i = 0.4$ mag. Only one bin shows a somewhat better result for a different bin size, namely $\Delta M_i = 0.5$ mag. Finding such results allows us to again appreciate the survey specific optimisation method, because general optimisations like those discussed in Section 6.1 would likely not have suggested the same kind of binning to suit our data the best.

Not surprisingly, we experience difficulties when performing stacking with a low number of AGN. Considering Figure 6.5 one can expect that it potentially can be difficult to find bins with enough AGN to recover reliable time lags for magnitudes above $M_i \sim -22.5$ mag and below $M_i \sim -25.5$ mag. This is an effect we indeed find to be true. Figures 6.3a and 6.3b show an example of a stacking attempt for a bin starting at $M_i = -22.35$ mag and continuing towards higher absolute magnitudes. We see that the uncertainties of the stacked time lag recoveries do not continue decreasing in size as a function of the bin width. The uncertainties remain the same due to the lack of AGN in that part of the absolute magnitude space to help with decreasing the estimate uncertainty. We find the same effect when we

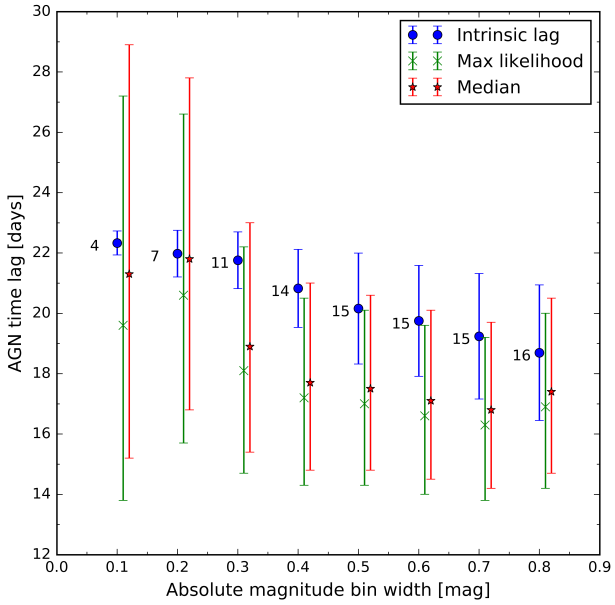

(a) Bins for $M_i = -22.35$ mag and dimmer.

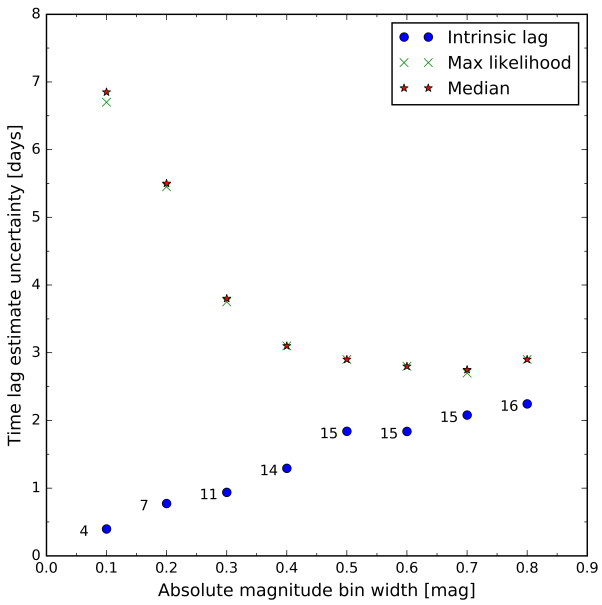

(b) Bins for $M_i = -22.35$ mag and dimmer.

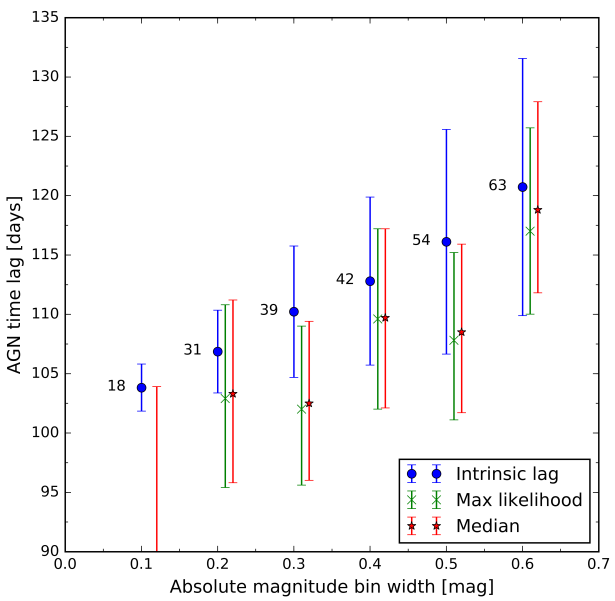

(c) Bins for $M_i = -24.95$ mag and brighter.

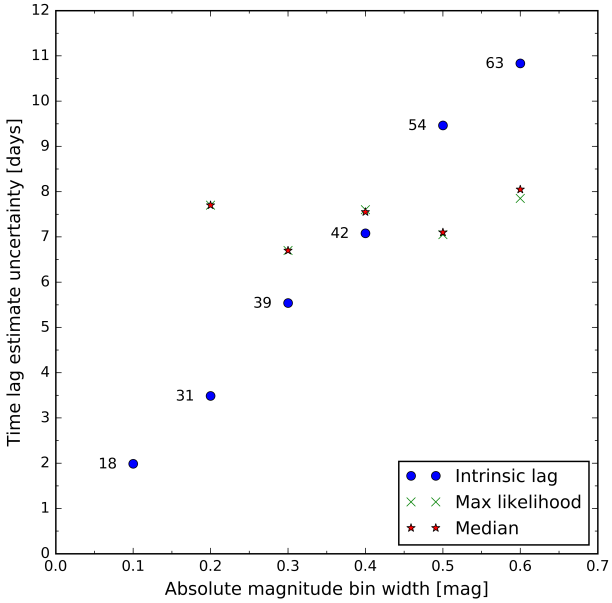

(d) Bins for $M_i = -24.95$ mag and brighter.

FIGURE 6.3: Two examples of bin size optimisation. The plots on the left hand size show the lag of the AGN samples, both in terms of the actual average lag and standard deviation, and the estimate and uncertainty for the sample. As the bin size increases, a larger variation of AGN is included in the sample, thus resulting a changing average and standard deviation. On the other hand, as more AGN are included, the stacking procedure allows for more precise estimates. On the right hand side, the intrinsic variation within the AGN sample is plotted together with the uncertainties of the estimates. The top two plots show the analysis for a bin starting at $M_i = -22.35$ mag, and ending at a higher absolute magnitude. For the two lower plots, the bin started at $M_i = -24.95$ mag, and ending at an even lower absolute magnitude. Because we wish to use a bin size for which the intrinsic variation and estimate uncertainty are approximately equal when applying stacking analysis to observational data, the bin starting at $M_i = -22.35$ mag will not be used for stacking purposes, as an optimal bin size could not be found. While the analysis was successful for the bin starting at $M_i = -24.95$ mag in the sense that it allowed to decide on an optimal bin size of $\Delta M_i = 0.4$ mag, the left hand side figure shows a bias toward underestimating the time lag.

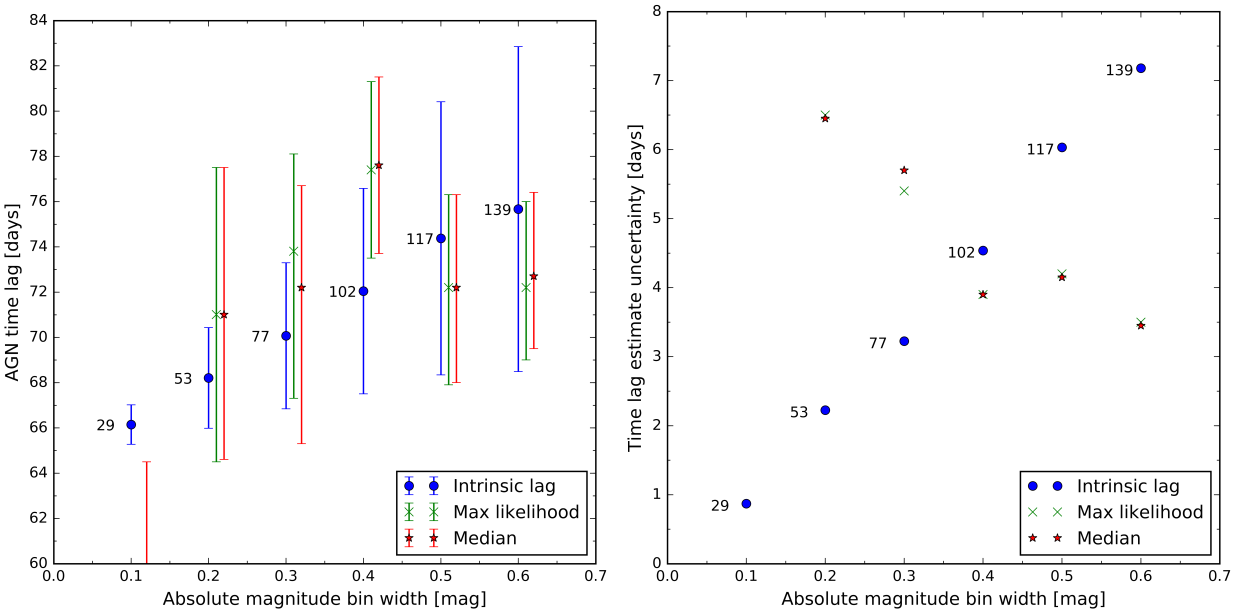

(a) Time lag estimates.

(b) Time lag uncertaintites.

Figure 6.4: Bin size optimisation for a bin starting at $M_i = -24.95$ mag, and ending at an even lower absolute magnitude. The plot on the left hand side shows the lag of the AGN samples, both in terms of the actual average lag and standard deviation, and the estimate and uncertainty for the sample. As the bin size increases, a larger variation of AGN is included in the sample, thus resulting a changing average and standard deviation. On the other hand, as more AGN are included, the stacking procedure allows for more precise estimates. On the right hand side, the intrinsic variation within the AGN sample is plotted together with the uncertainties of the estimates. We will be using the bin size for which the intrinsic variation and estimate uncertainty when applying stacking analysis to observational data. The analysis was very successful for this bin, showing clear trends, no bias, and allowing to easily decide on an optimal bin size of $\Delta M_i = 0.4$ mag.

look for a bin below $M_i = \ -26.15$ mag. The conclusion for these places of the absolute magnitude space is simply that the AGN we observe with DES/OzDES that fall into these categories cannot be used for the purposes of stacked reverberation mapping.

When analysing stacked estimates of time lags for groups of similar AGN, we find that intrinsic time lags shorter than approximately two months seem to be more difficult to constrain than longer lags. This is especially the case for AGN with lags of a month and shorter. We have a number of suggestions for the reason behind this behaviour. Firstly, it could be that the bin sizes for these lags should ideally be somewhat smaller, but the number of AGN in the bins are too small to obtain a good time lag recovery even after stacking has been applied. This effect can easily be tested by repeating the same stacking analysis, but with some more AGN in the bins. The second explanation concerns aliasing. Figure 4.1 shows the distribution of time lags considered by Javelin for an AGN with a time lag of $\tau_0 = 129$ days. Such a histogram will resemble the likelihood function of the time lag. Although there is one very clear peak around $\tau = 129$ days, there are two secondary

peaks for longer time lags, whose presence is due to aliasing that occurs when JAVELIN considers a time lag range much larger than the underlying lag. Because the shortest prior we use in JAVELIN is 1000 days, shorter time lags are likely of suffering from aliasing. When we stack the posterior distributions of a number of AGN with short time lags we may be stacking secondary peaks which are present due to aliasing, thus creating a noisy result, for which it is more difficult to find a good time lag estimate. This, too, can be tested, this time by decreasing the range of time lags JAVELIN is to investigate. Finally, the cadence of the spectroscopic observations by OzDES, and thus the emission line measurements, is approximately a month. Short time lags may thus simply not be sampled well enough to obtain particularly successful estimates. To test this, we can run our simulations with a higher cadence for the observations. In Section 5.3 we showed that stacking of individual time lag estimates yields a better precision of the recovered time lag for an AGN sample, which is comparable to the individual time lag recoveries obtained when increasing the sampling of light curves. This, of course, implies that a higher observation cadence results in better estimates. We expect the two latter explanations to be the most likely, because they are based on effects we already have observed. The first explanation is possible still, but we consider it unlikely, since we struggle finding very good estimates for magnitudes even below $M_i = -23.0$ mag, where there are a large number of AGN whose time lag estimates may be stacked.

Figure 6.4 shows the analysis for the bin which had the best outcome. In contrast to this bin, most other bins show that the stacked time lag recoveries are biased towards underestimating the average time lag of the samples. An example of this is shown in Figures 6.3c and 6.3d. While the bias is concerning, it is an effect we expect to be able to apply the right corrections to in order to extract real physics, given some more investigation time.

We have found the bin sizes for optimal stacked reverberation mapping to be performed with DES/OzDES data for the full extent of the Mg II emission line. Figure 6.5 shows the distribution of AGN monitored by DES/OzDES, with the redshift-magnitude space which should allow for stacking analysis to be successful when applied to three years' worth of DES/OzDES data highlighted in a semi-transparent pink colour. The size of the individual bins can be recognised by a brighter or darker shade of pink, and the optimal bin size is $\Delta M_i = 0.4$ mag for all bins except the uppermost one, which has a preferred bin size of $\Delta M_i = 0.5$ mag. The redshifts corresponding to transitions between various emission lines are given by vertical, dark grey lines. While we will exclude some AGN from the stacking procedure, the majority – 95.9% – of the AGN where the Mg II line is well detected can be used to estimate time lags. A similar analysis may, of course, be made for the Hβ and C IV lines. In addition, we expect it to be very instructive to analyse bins for redshifts where there is an overlap between two emission lines. Further analysis of this kind is the next step for statistical reverberation mapping with DES/OzDES AGN samples, and will be commenced shortly. The reason it is not included in this Thesis, is simply shortness of time.

Although the third year of observations for DES/OzDES has finished, the emission line data we need to perform reverberation mapping have not yet been extracted. A team lead by Gisella de Rosa (Ohio State University, and Space Telescope Science Institute) is working on the line measurements. It is expected that the data will be available shortly after the submission of this Thesis. At that point in time, reverberation mapping in bulk will be

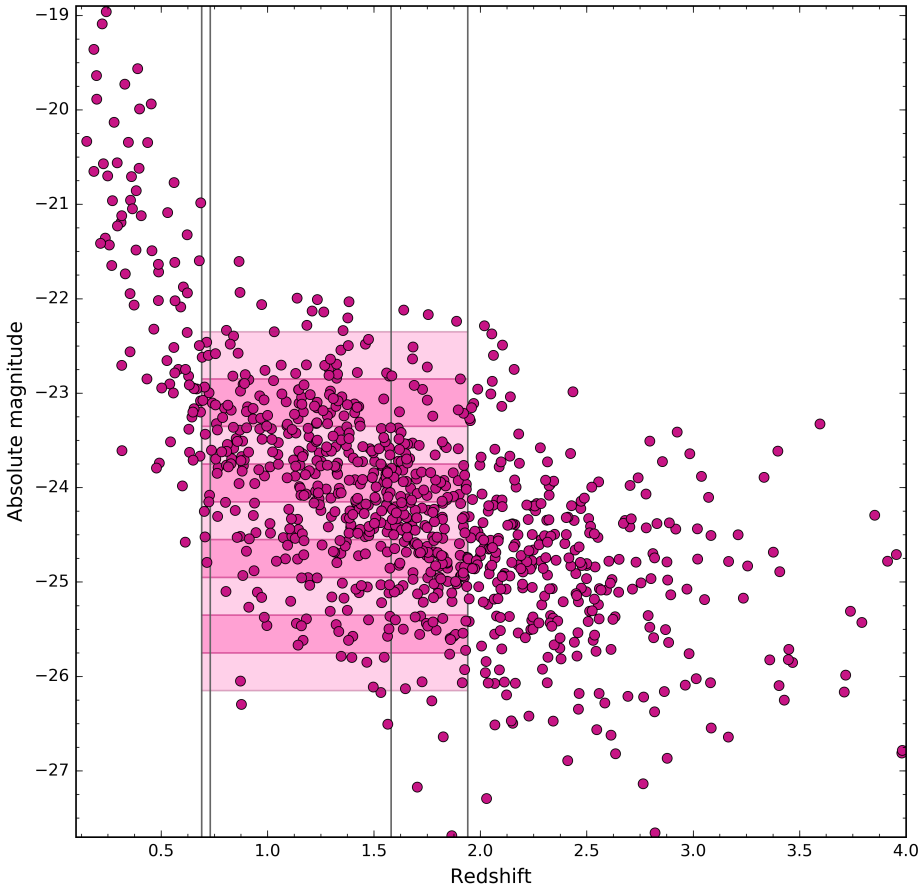

Figure 6.5: Distribution of AGN monitored by DES/OzDES for the reverberation mapping project, together with the area in magnitude-redshift space which we have found can be used for time lag recoveries in bulk. The dark grey, vertical lines mark the redshifts at which a new emission line can be used, or can no longer be used. The light pink area spans all redshifts as which Mg II can be used for reverberation mapping, and shows the magnitudes for which we can expect to obtain useful time lag estimates for AGN samples. Each individual bin is marked by a brighter or darker shade of pink.

started immediately. Figure 6.4 shows an example of a bin for which we expect to obtain a very successful time lag recovery, and we also expect our analysis to have improved by the time the data are made available, allowing to obtain even better time lag recoveries. For the Mg II line, we have found that 95.9% of the AGN will contribute to the stacked reverberation work. This is a great improvement from the 35-45% of AGN King et al. (2015) estimated to allow for successful time lag recoveries.

7 Conclusion

In this Thesis we have focused on one method allowing us to learn more about AGN, namely reverberation mapping. With reverberation mapping we are able to study the innermost regions of AGN, and thus the closest environments of supermassive black holes. Although the method of reverberation mapping has been known for decades, it has become more important after Watson et al. (2011) showed that by utilising this method we may be able to use AGN as standard candles. This is a very promising result, because while current standard candles only can be seen to a redshift of $z \sim 2$ (Jones et al., 2013), AGN can be observed to redshifts of $z \sim 7$ (Mortlock et al., 2011). By establishing AGN as standard candles we will be able to more reliably determine distances that were previously unreachable. Such measurements can help with testing the values of cosmological parameters, and have the potential of teaching us new and surprising things about the Universe. Whenever a new observation or measurement type has become available, more information about the Universe has been unfold. The use of type Ia supernovae as standard candles led to the surprising discovery of an accelerating expansion of the Universe (Riess et al., 1998; Perlmutter et al., 1999), driven by a property we call dark energy. Establishing AGN as standard candles would open up a new window to information not yet available to us, potentially allowing to probe the exotic and poorly understood dark energy, and investigating whether it changes over time.

Progress in technology has allowed for reverberation mapping to become somewhat more effective than it has been before. However, it is still an observationally time consuming process. In an effort to make the most out of available observations, Fine et al. (2012) introduced the method of composite reverberation mapping, in which noisy, individual time lag estimates are stacked to obtain a time lag recovery for the average lag within a group of AGN. Showing promising results, Fine et al. (2013) made use of Panoramic Survey Telescope & Rapid Response System 1 (Pan-STARRS1) medium-deep survey data in such a stacking procedure, and the results they obtained were in agreement with existing knowledge based

on individual time lag recoveries. Brewer & Elliott (2014) presented an alternative stacking method, in which they made use of a Bayesian hierarchical model. For the analysis in this Thesis we implemented a stacking procedure based on standard Bayesian statistics, without making use of a hierarchical model.

7.1 Work in This Thesis

Instead of using the more traditional technique of cross-correlation, we have made use of JAVELIN to recover the time lags of individual AGN. To ensure optimal usage of the program, we tested the various parameters the user of the software can manipulate. We found that the chain length, as well as the burn-in period of the MCMC, had to be increased from the default values set for the program. Wishing to not bias our analysis, we chose to allow JAVELIN to always search for the true time lag within a large range of time lags, without penalising any particular lag values. With simulated data based on what we expect to obtain from DES/OzDES observations, we found that the program was not tuned for data as noisy as ours, and had to be modified slightly to avoid numerical problems.

We have explored the transfer function, deriving its shape based on a small number of idealised cloud distributions. Infinitesimally thin distributions of clouds in the form of a face-on disk or a sphere around the black hole both lead to a top-hat transfer function. A top-hat transfer function is not only a simple function to work with, but it also leads to conservative results. This is because the emission line light curve, to which the continuum light curve is compared, will be smoothed strongly by a transfer function of this shape.

Because the geometric distribution of BLR clouds is unknown, the transfer function, too, is unknown. JAVELIN assumes a top-hat transfer function, and to test the credibility of the program for realistic data, we made use of different transfer functions to produce emission line light curves, and allowed JAVELIN to recover time lags for these. We found that JAVELIN's ability to estimate time lags correctly was not influenced by a change of transfer function.

After careful considerations, we developed a simple stacking method that suits our analysis with JAVELIN. Making use of the likelihoods calculated for each step of the MCMC within JAVELIN, we stacked individual time lag estimates by implementing a Bayesian statistics model. The method resembled that of Brewer & Elliott (2014), but assumed instead that the distribution of time lags within a group of AGN could be described by a δ-function for simplicity, reducing a hierarchical model to a more standard Bayesian analysis.

In order to test the goodness of stacking, we considered a few idealistic cases, where we found and stacked the individual time lag estimates for ten different light curve realisations of a single AGN. We found that stacking allowed to find more precise time lag estimates. When increasing the measurement uncertainty in our simulations to twice the expected size, the stacked time lag estimates were better than the individual time lag recoveries where the measurement uncertainties were kept at the expected size. We also found that by allowing the intrinsic light curves to vary, although still being based on the same AGN, we would obtain time lag recoveries which were less biased than if the underlying light curve was the same for all AGN. We are happy about this result, because we know that when stacking will be applied to observational data, the AGN, and thus the light curves, will differ from each

other. Knowing that the use of different light curves in stacking analysis not only preserves, but also improves, the reliability of the stacked time lag recovery is very reassuring. Finally, we also compared stacked time lag estimates to individual estimates obtained for AGN whose light curves had been sampled more often. Based on Fine et al. (2012), we hoped that the stacked time lag recovery would be comparable to an individual time lag recovery based on better sampled light curves. Indeed, we found that the stacked time lag recoveries were at least as good as the estimates for an individual AGN with well sampled light curves – at least when the underlying light curves were different. If the underlying light curves were identical, the stacked result was in our case biased towards time lag underestimation due to the shape of the light curve.

We applied the stacking method to simulated three years' worth of data to see if time lag estimates could be obtained at this point in time. By changing the sizes of the bins and comparing the intrinsic variation of time lags within an AGN bin to the uncertainty of the stacked time lag estimate, we found the optimal absolute magnitude bin sizes for all of the AGN monitored by DES/OzDES where Mg II will be used as the reverberation mapping emission line. In the majority of the cases, the optimal bin size was $\Delta M_i = 0.4$ mag, the exception being a single bin with an optimal bin size of $\Delta M_i = 0.5$ mag. While we observed a bias towards the stacked time lag recoveries to underestimate the average lag within the bins, we expect that by further exploring the bias we will reach a point where the stacked estimates can be trusted. Even with the bias present, the true value of the average time lag within a group of AGN was mostly found to be contained within the uncertainty of the stacked time lag recovery. Moreover, the 1σ uncertainties of the stacked time lag estimates were found to be of the order of only 10% of the time lag values, which is a very good result.

7.2 Future Work

The analysis performed for this Thesis can, and will, easily be extended to include analysis for other emission lines, as well as recovering time lags for groups of AGN more reliably. The results we have obtained here are preliminary, but of great importance, as they show that we can expect as many as 95% of the AGN monitored by DES/OzDES to contribute to teaching us more about the Universe already this year. We expect to obtain even better results by the end of the survey in two years, and we look forward to seeing the total number of AGN with recovered time lags increase immensely in size from the small number it is today. It is no doubt that the work in this Thesis will be important in the years to come, when more reverberation mapping data will become available, and AGN will contribute to a far more thorough study of the Universe and its evolution than ever before.

An important step in coming analysis will be to extend the bin optimisation to include the other emission lines, and to perform calibration of the $R-L$ relationship between them. This should not be much of a problem for the Mg II and the C IV lines, since there is a big overlap with a large number of AGN in the DES/OzDES catalogue. Calibrating the $R-L$ relationship between the Hβ and Mg II lines will be more difficult because of the small overlap within the DES/OzDES sample, but an attempt will most certainly be made. In analysis to come we plan to advance our methods to a full hierarchical model, which will allow us to obtain better uncertainty estimates capable of describing the intrinsic variation

within each AGN bin. Such information will become very important when taking the step from simulations to observational data.

One of the first steps to take now, will be to extract emission line data from the DES/OzDES observations to make it possible for reverberation mapping to be done, and to and apply the results from this Thesis to real life data. The work on emission line data extraction has already been started, and is led by Gisella de Rosa (Ohio State University, and Space Telescope Science Institute). The working group includes a number of international collaborators, including members of DES and OzDES. De Rosa also recently received a grant which can partially be used to involve a professional software developer in the process, something which will take place in a few months.

If AGN are to be used for distance measurements, a very important calibration to be made is one between AGN and type Ia supernovae. Such a calibration will be extremely important, as it will strengthen the reliability of supernova distance measurements, in addition to fully establishing the role of AGN as standard candles. A calibration like this is likely to happen years from now, however, it is a very important goal to keep in mind.

The prospect of using AGN as standard candles is, of course, very exciting. A very fortunate aspect of the analysis performed for this Thesis is, however, that our work will be useful even in the event where AGN should turn out to not be useful for distance measurements. Reverberation mapping is also important for black hole mass measurements beyond the local universe. The results from this Thesis are thus also applicable for learning more about black hole growth – a topic for which there are not many observational measurements. It is likely that the methods and code developed for this Thesis will be useful in the future to study black hole evolution, by current or future collaborators.

References

Abramowicz M. A., Calvani M., Nobili L., 1980, ApJ, 242, 772

Allen D. A., 1987, in Exercises in Astronomy, Kleczek J., ed., Springer, pp. 251–254

Baldwin J., Ferland G., Korista K., Verner D., 1995, ApJ Lett., 455, L119

Baldwin J. A., 1977, ApJ, 214, 679

Bentz M. C. et al., 2013, ApJ, 767, 149

Bentz M. C., Katz S., 2015, PASP, 127, 67

Bentz M. C., Peterson B. M., Netzer H., Pogge R. W., Vestergaard M., 2009, ApJ, 697, 160

Blandford R. D., McKee C. F., 1982, ApJ, 255, 419

Brewer B. J., Elliott T. M., 2014, MNRAS, 439, L31

Cherepashchuk A. M., Lyutyi V. M., 1973, Astrophys. Lett., 13, 165

Denney K. D. et al., 2010, ApJ, 721, 715

Diehl H. T. et al., 2014, in Proc. SPIE, Vol. 9149, Observatory Operations: Strategies, Processes, and Systems V, p. 91490V

Docobo J. A., Andrade M., 2015, AJ, 149, 45

Doppler C., 1843, Abhandlungen dk Böhmischen Gesell. d. Wiss, 2, 467

Eden A., 1992, Search for Christian Doppler. Springer Vienna, Vienna

Efron B., Tibshirani R., 1993, An introduction to the bootstrap, Monographs on Statistics and Applied Probability; 57. Chapman & Hall/CRC, New York

Fan X. et al., 2001, AJ, 122, 2833

Fine S. et al., 2012, MNRAS, 427, 2701

Fine S. et al., 2013, MNRAS, 434, L16

Flaugher B., 2005, International Journal of Modern Physics A, 20, 3121

Flaugher B. L. et al., 2012, in Proc. SPIE, Vol. 8446, Ground-based and Airborne Instrumentation for Astronomy IV, p. 844611

Foreman-Mackey D., Hogg D. W., Lang D., Goodman J., 2013, PASP, 125, 306

Freedman W. L., Madore B. F., 2010, ARA&A, 48, 673

Gaskell C. M., Sparke L. S., 1986, ApJ, 305, 175

Goodman J., Weare J., 2010, Comm. App. Math. Comp., 5, 65

Grier C. J. et al., 2012a, ApJ, 755, 60

Grier C. J. et al., 2012b, ApJ Lett., 744, L4

Hastings W. K., 1970, Biometrika, 57, 97

Hogg D. W., Baldry I. K., Blanton M. R., Eisenstein D. J., 2002, ArXiv Astrophysics e-prints

Horne K., Peterson B. M., Collier S. J., Netzer H., 2004, PASP, 116, 465

Hubble E., 1929, Proceedings of the National Academy of Science, 15, 168

Hubble E., 1936, ApJ, 84, 517

Hughes P. A., Aller H. D., Aller M. F., 1992, ApJ, 396, 469

Jones D. O. et al., 2013, ApJ, 768, 166

Kaspi S., Brandt W. N., Maoz D., Netzer H., Schneider D. P., Shemmer O., 2007, ApJ, 659, 997

Kaspi S., Smith P. S., Netzer H., Maoz D., Jannuzi B. T., Giveon U., 2000, ApJ, 533, 631

Kelly B. C., Bechtold J., Siemiginowska A., 2009, The Astrophysical Journal, 698, 895

Kilerci Eser E., Vestergaard M., Peterson B. M., Denney K. D., Bentz M. C., 2015, ApJ, 801, 8

Kim B., An D., Stauffer J. R., Lee Y. S., Terndrup D. M., Johnson J. A., 2016, ApJS, 222, 19

King A. L. et al., 2015, MNRAS, 453, 1701

Kollatschny W., Bischoff K., 2002, A&A, 386, L19

Kollmeier J. A. et al., 2006, ApJ, 648, 128

Kozłowski S. et al., 2010, ApJ, 708, 927

Leavitt H. S., 1908, Annals of Harvard College Observatory, 60, 87

Leavitt H. S., Pickering E. C., 1912, Harvard College Observatory Circular, 173, 1

Lemaître G., 1927, Annales de la Société Scientifique de Bruxelles, 47, 49

Lemaître G., 1931, MNRAS, 91, 483

Liu H. T., Feng H. C., Bai J. M., 2015, ArXiv e-prints

MacLeod C. L. et al., 2010, ApJ, 721, 1014

Marziani P., Sulentic J. W., Zamanov R., Calvani M., Della Valle M., Stirpe G., Dultzin-Hacyan D., 2003, Memorie della Societa Astronomica Italiana Supplementi, 3, 218

Metropolis N., Rosenbluth A. W., Rosenbluth M. N., Teller A. H., Teller E., 1953, The Journal of Chemical Physics, 21, 1087

Mortlock D. J. et al., 2011, Nature, 474, 616

Ngeow C.-C., Sarkar S., Bhardwaj A., Kanbur S. M., Singh H. P., 2015, ApJ, 813, 57

Okuda T., 2002, PASJ, 54, 253

Onken C. A., Ferrarese L., Merritt D., Peterson B. M., Pogge R. W., Vestergaard M., Wandel A., 2004, in IAU Symposium, Vol. 222, The Interplay Among Black Holes, Stars and ISM in Galactic Nuclei, Storchi-Bergmann T., Ho L. C., Schmitt H. R., eds., pp. 109–110

Paczyński B., Wiita P. J., 1980, A&A, 88, 23

Pancoast A., Brewer B. J., Treu T., 2014, MNRAS, 445, 3055

Perlmutter S. et al., 1999, ApJ, 517, 565

Peterson B. M., 1988, PASP, 100, 18

Peterson B. M., 1993, PASP, 105, 247

Peterson B. M., 1997, An Introduction to Active Galactic Nuclei

Peterson B. M., 2001, in Advanced Lectures on the Starburst-AGN, Aretxaga I., Kunth D., Mújica R., eds., p. 3

Peterson B. M., 2006, in Lecture Notes in Physics, Berlin Springer Verlag, Vol. 693, Physics of Active Galactic Nuclei at all Scales, Alloin D., ed., p. 77

Peterson B. M., 2014, Space Sci. Rev., 183, 253

Peterson B. M. et al., 2004, ApJ, 613, 682

Peterson B. M. et al., 2014, ApJ, 795, 149

Peterson B. M., Horne K., 2004, Astronomische Nachrichten, 325, 248

Pozo Nuñez F. et al., 2013, A&A, 552, A1

Reid M. J., McClintock J. E., Steiner J. F., Steeghs D., Remillard R. A., Dhawan V., Narayan R., 2014, ApJ, 796, 2

Riess A. G. et al., 1998, AJ, 116, 1009

Riess A. G. et al., 2009, ApJS, 183, 109

Ryden B. S., Peterson B. M., 2010, Foundations of Astrophysics. Addison-Wesley

Saunders W. et al., 2004, in Proc. SPIE, Vol. 5492, Ground-based Instrumentation for Astronomy, Moorwood A. F. M., Iye M., eds., pp. 389–400

Shen Y. et al., 2015, ApJS, 216, 4

Shen Y. et al., 2016, ApJ, 818, 30

Skielboe A., Pancoast A., Treu T., Park D., Barth A. J., Bentz M. C., 2015, MNRAS, 454, 144

Smith G. A. et al., 2004, in Proc. SPIE, Vol. 5492, Ground-based Instrumentation for Astronomy, Moorwood A. F. M., Iye M., eds., pp. 410–420

Soszynski I. et al., 2008, Acta Astron., 58, 163

Tammann G. A., Sandage A., Reindl B., 2008, A&A Rev. , 15, 289

Trakhtenbrot B., Netzer H., 2012, MNRAS, 427, 3081

Urry C. M., Padovani P., 1995, Publications of the Astronomical Society of the Pacific, 803

Véron-Cetty M. P., Véron P., 2000, A&A Rev. , 10, 81

Vestergaard M., Wilkes B. J., Barthel P. D., 2000, ApJ Lett., 538, L103

Watson D., Denney K. D., Vestergaard M., Davis T. M., 2011, ApJ Lett., 740, L49

Woltjer L., 1959, ApJ, 130, 38

Yuan F. et al., 2015, MNRAS, 452, 3047

Zu Y., Kochanek C. S., Peterson B. M., 2011, The Astrophysical Journal, 735, 80

Appendices

A

Choice of MCMC Parameters for JAVELIN

When we started our analysis, we based the value of the MCMC parameters in JAVELIN – the number of walkers w, burn-in period b, and chain length (number of steps after the burn in period) c – on those used by King et al. (2015). By default, JAVELIN uses $w = 100$, $b = 50$, and $c = 50$. King et al. (2015) used $w = 100$, $b = 150$, and $c = 150$, obtaining very reasonable results. Knowing that a large amount of simulations would be required for this project, we wished to investigate whether these numbers could be made smaller to shorten the computational time, without the results suffering notably statistically.

A.1 Convergence Analysis

We performed a careful study of the behaviour of the MCMC chains for a number of combinations of MCMC parameters. Finding unexpected behaviour, we contacted the developer of JAVELIN, learning that the program had changed since being described in Zu, Kochanek & Peterson (2011). Users of JAVELIN are now encouraged to use MCMC parameter values larger than the defaults of the program. The MCMC routine has also been changed. In the older version of the software, SPEAR, the standard Metropolis-Hastings algorithm (Metropolis et al., 1953; Hastings, 1970) was used, whereas JAVELIN makes use of the newer `emcee` algorithm, developed specifically for the Python language by Foreman-Mackey et al. (2013). The `emcee` algorithm explained the suspicious behaviour we had seen, but required a different type of analysis to find the optimal MCMC parameters for our use.

Foreman-Mackey et al. (2013) recommend a large number of walkers – preferably hundreds – when utilising the `emcee` algorithm. The need to run the chains for long enough is also stressed. To test whether the chains are run for long enough, Foreman-Mackey et al. (2013) suggest to plot the autocorrelation as a function of time. A chain which has not been run for long enough will be found to have an autocorrelation time which is a sizeable fraction of the chain, so Foreman-Mackey et al. (2013) suggest to run the chains until the

autocorrelation length, the number of steps required for the value of the autocorrelation to drop to zero on average, is at about one tenth of the chain lengths. In Figure A.1 we present the autocorrelation as a function of step number for chains of various lengths. We see that the autocorrelation requirement clearly is not satisfied by $c = 15$ steps in Figure A.1a, but is satisfied in Figure A.1c with $c = 10\ 000$ steps, and potentially also by $c = 1000$ steps in Figure A.1b. A chain length of only a few hundred steps must therefore be rejected, as it is not satisfactory by the standards of the `emcee` algorithm.

When studying the time lag estimates when the chains were chosen to be long (for the $c = 10\ 000$ steps case in particular, but also for the $c = 1000$ steps case), the time lags were found to be hard to estimate due to a much wider likelihood distribution than seen when shorter chain lengths were used. Upon further investigation, we found that JAVELIN had problems estimating the transfer function width and height, searching for suitable values as high as 10^{47} days for transfer function width. The diverging parameters affected the ability to constrain the remaining parameters, including the time lag. Knowing that the transfer function is determined by the distribution of BLR clouds, and we found in Section 3.1 that our worst case scenario, an infinitesimally thin sphere of BLR clouds, results in a top-hat transfer function of width twice the BLR radius, we determined to set an upper limit based on our knowledge about the BLR sizes in the DES/OzDES AGN sample. Not expecting the transfer function to take the worst case scenario, nor to observe many time lags longer than 500 days, we modified the JAVELIN source code to assume an upper limit of 1000 days for the width of the transfer function. We set an somewhat more arbitrary, but consistent with previous results, limit for the height of the transfer function, allowing it only to grow up to a value of 5. Putting upper limits on the parameters describing the transfer function allowed JAVELIN to explore parameter values known to be physically reasonable, resulting in far better time lag estimates.

JAVELIN allows the user to specify boundaries between which is is supposed to look for time lags, and to logarithmically penalise lags larger than a certain fraction of the length of the baseline, which is the total span of the input light curves. The default in JAVELIN is to look for time lags within the full baseline, but to penalise lags longer than 30% of the baseline. Not wanting to impose any bias onto our results, we chose not to penalise any time lags. However, with a baseline of 1931 days we found strong aliasing in our results, leading us to search for alternative boundary limits. King et al. (2015) used a boundary rule of zero to three times the true time lag for their simulations, however, knowing that we can end up looking at time lags shorter than a month, we felt uncomfortable using this rule, as the range within which JAVELIN would be searching for time lags in such a case would be very small. We decided to set the limits to be between 0 and 1000 days, but to rise the upper limit to three times the time lag if this value exceeds 1000 days.

After making sure that JAVELIN was running smoothly with the settings we had chosen, we again investigated the number of walkers, as well as the length of the burn-in period, and the chain length after it, making sure all five of the parameters JAVELIN is fitting for were considered. We found that we needed $w = 100$ walkers to get satisfactory results, and that the burn in length could be set to $b = 500$ steps. When considering chain lengths of $c = 500$ steps, we found that JAVELIN had some difficulties estimating some of the parameters, as shown by the rough, dotted histograms in Figure A.2. Increasing the number of steps to

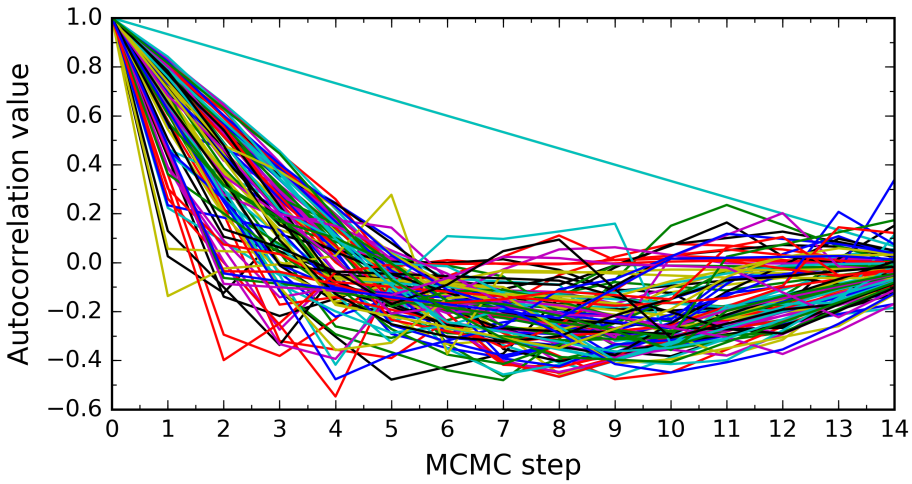

(a) MCMC with chain length 15 steps

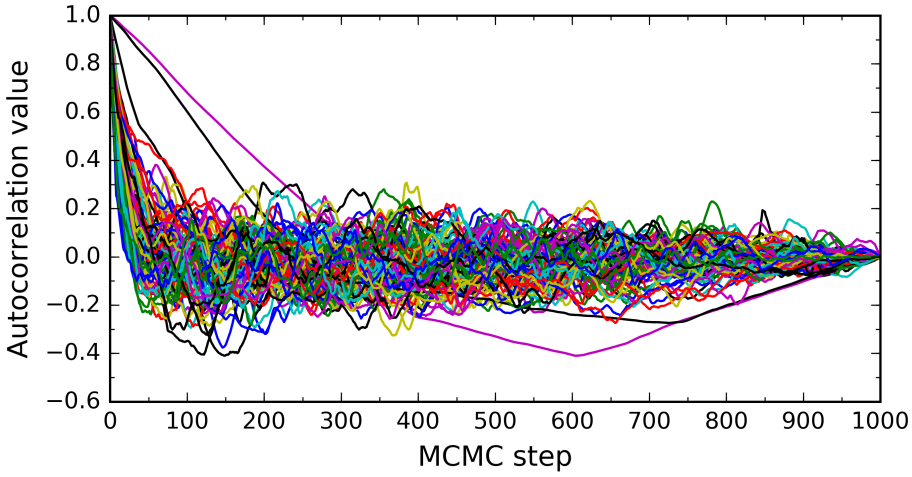

(b) MCMC with chain length 1000 steps

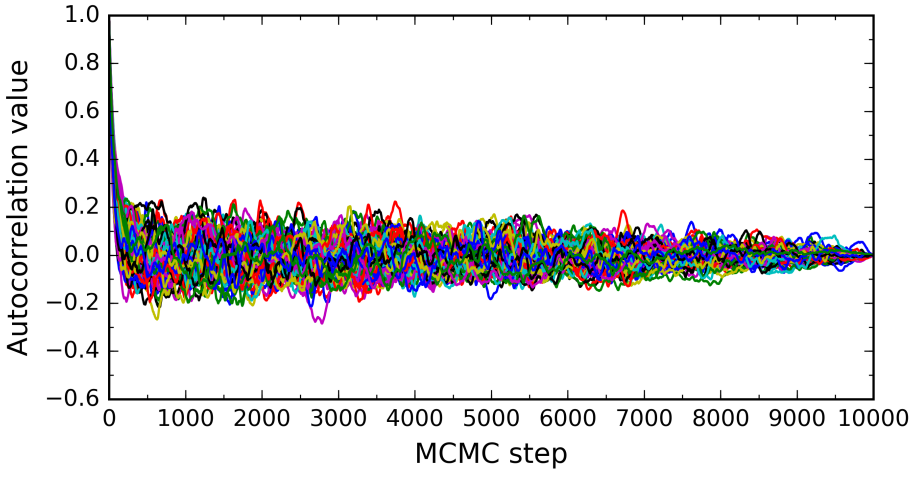

(c) MCMC with chain length 10 000 steps

Figure A.1: The autocorrelation is here plotted as a function of chain step for four different chain lengths. For short chain lengths, such as only 15 steps, the autocorrelation length is a sizeable fraction of the chain length. When 10 000 steps were used, on the other hand, the autocorrelation length is distinctly shorter than the chain length. Based on the 1000 and 10 000 step cases, we can draw the conclusion that the chains need to be 1000 steps long at the very least in order to for the estimate based on the `emcee` MCMC process to be reliable.

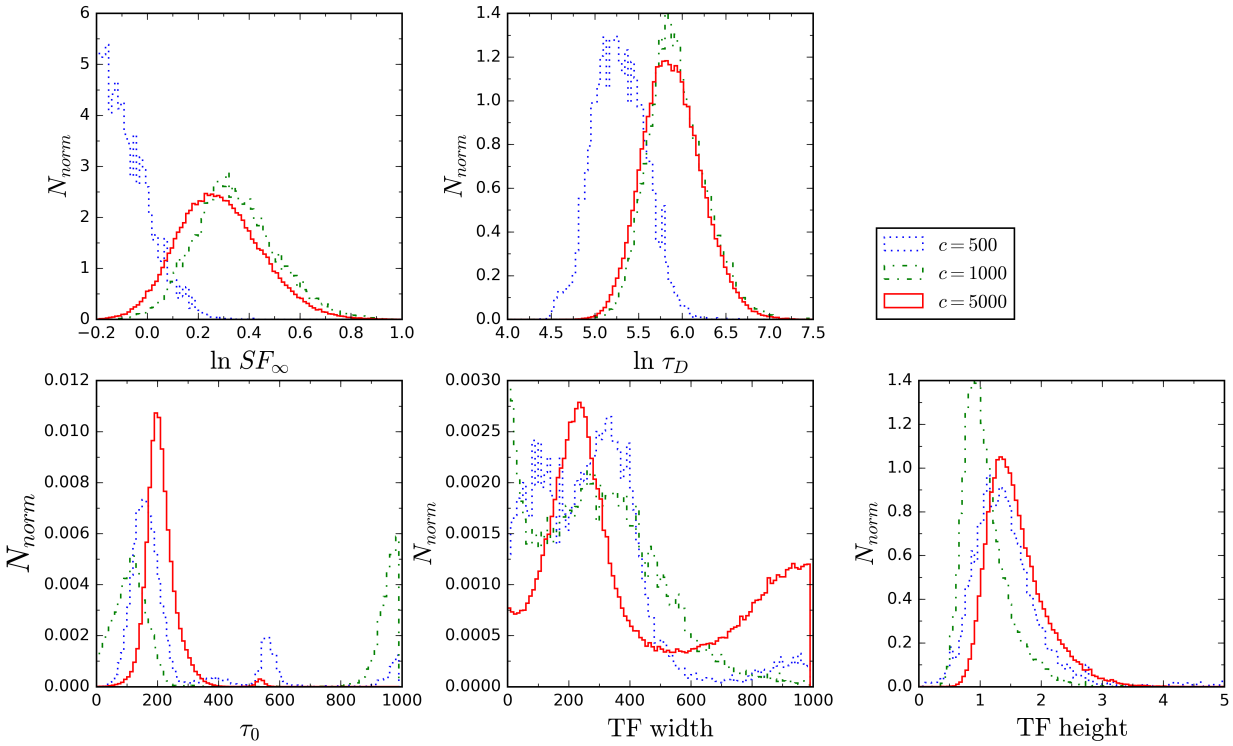

FIGURE A.2: Distributions of values for SF_∞, τ_D, τ, and the width and height of the transfer function considered by JAVELIN for chain lengths $c = 500$, $c = 1000$, and $c = 5000$. The histograms are normalised such that the total areas under the curves equal to unity, and they are close to proportionally related to the final estimate of the values. The lag estimates, shown in the lower left sub-figure, are within 1σ of the true value for all chain lengths. Given that the autocorrelation length being approximately 100 steps, we can therefore decide on a chain length of 1000 steps without worrying about the possibility of it potentially being too short.

$c = 1000$ allowed JAVELIN to better center around a value both for SF_∞ and the transfer function width. All distributions are even smoother if the number of steps is increased to $c = 5000$ steps, as shown in Figure A.2. Note that there are secondary tops in the time lag distribution for lags higher than the underlying lag, $\tau_0 = 129$ days, especially for the $c = 500$ and $c = 1000$ cases. This is due to aliasing, because JAVELIN had to search for time lags along a time segment much longer than the underlying time lag. Although running the chains for $c = 5000$ steps yielded smoother, potentially more reliable distributions than for $c = 1000$, we decided to go for the latter option for our simulations in this project. This was in order to limit the computational time, which would increase significantly by increasing the number of steps by a factor of five, without yielding significantly better time lag estimates.

A.2 Concerns With Parameter Estimates

Considering Figure A.2, one may get somewhat concerned about the parameter values one will estimate from the distributions. While the time lag estimate is not too far off the true

value, $\tau_0 = 129$ days, the width of the transfer function, which is chosen to be 20% of the time lag value in our simulations, seems to have a preferred value of several hundred. We suspect the reason for this to be aliasing, similar to the aliasing we observe when recovering AGN time lags. The transfer function used to create the light curve behind Figure A.2 would have been almost 30 days wide – a number which clearly is much smaller than the 1000 days allowed by the MCMC to explore. If this is the case, a better sampling of the light curve should allow for an estimate closer to 30 days to be found. To investigate this, we created a set of light curves which we sampled such that the total number of photometric and spectroscopic measurements would be ten times the number of measurements we expect to obtain from DES/OzDES. We also created one set of light curves with the same kind of excellent sampling, but excluded the measurements which fell within the seasonal gaps of DES/OzDES. Having decided on a chain length of $c = 1000$ steps, we used the same chain length when analysing the good sampling scenarios, and compared the results to those from the standard DES/OzDES sampling with $c = 1000$ steps. The distributions equivalent to those in Figure A.2, but comparing three different sampling scenarios are shown in Figure A.3. As expected, we see most distributions becoming narrower with better sampling, implying that a more precise estimate can be found for the parameters. Considering the distributions for the transfer function width, we see that a shorter transfer function width becomes favourable if the light curves are sampled well. This suggests that more frequent sampling would be beneficial to our surveys. However, we believe our time lag estimates are still to be trusted with the standard DES/OzDES sampling and chains running for $c = 1000$ days. We have two reasons for this; firstly, the time lag estimates are consistently accurate in our simulations, and secondly, the reason behind a longer preferred transfer function width for poor sampling can be explained by Javelin estimating the lags based on light curve features with long time variations as opposed to short time variations, which it easily could interpret as a wider transfer function.

A second point of concern in Figure A.2 is that the values of SF_∞ and τ_D are both underestimated compared to the underlying values of the parameters we chose when creating the light curves which were analysed by Javelin to create these distributions. However, according to Zu, Kochanek & Peterson (2011), Javelin is set with priors on these parameters, and deviating values are logarithmically penalised. For τ_D, the prior is favouring τ_D values close to the median sampling interval. With the photometric sampling interval being one or two days for the good sampling scenarios, and approximately a week for the real measurements, it is not too surprising that τ_D values of several hundred days can be difficult to estimate correctly. As for SF_∞, we recall that this parameter describes how much an AGN's luminosity is capable of varying, and is only obtained when studying the magnitude over very long periods of time. Even though DES/OzDES represent far longer reverberation mapping surveys than performed before, it can be difficult to correctly estimate this parameter. The fact that both parameters are underestimated can thus be explained by the nature of Javelin, and physical reasons. Because these parameters only assist Javelin in modelling the continuum light curve, and the software still is capable of recovering the time lags well, we conclude that our estimates based on MCMC runs with chain lengths of $c = 1000$ steps can be trusted.

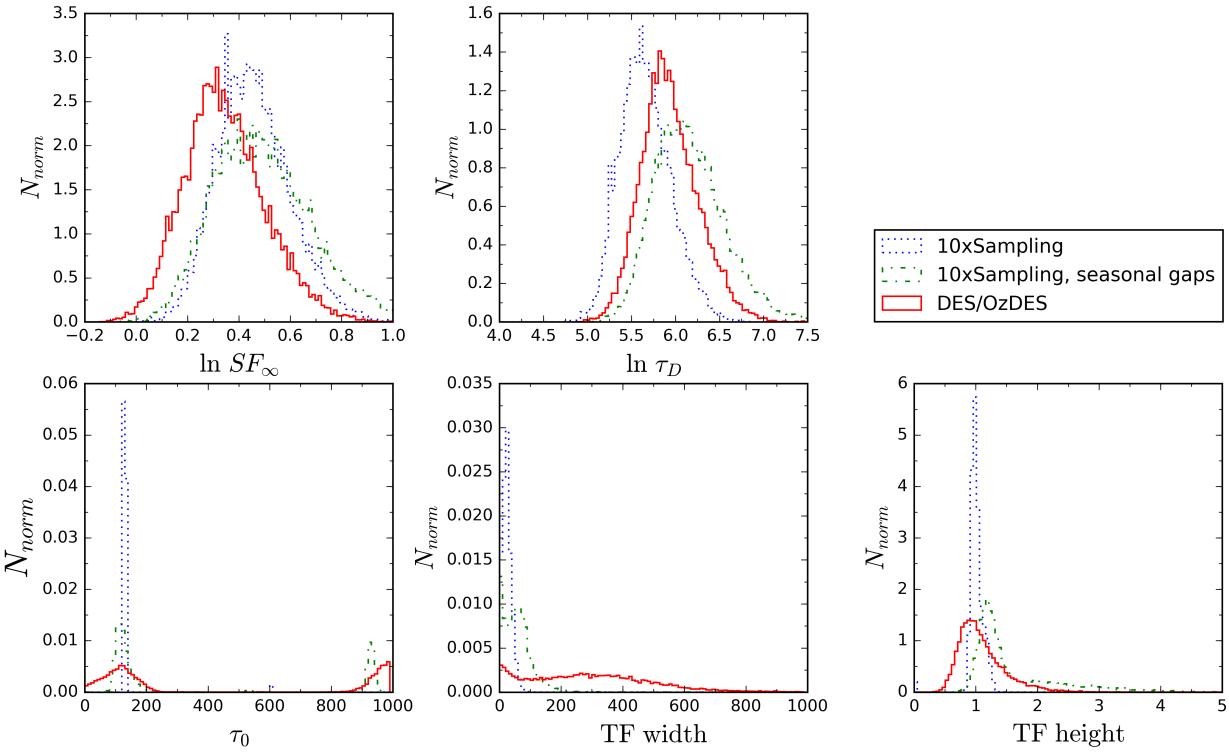

FIGURE A.3: Distributions of values for SF_∞, τ_D, τ, and the width and height of the transfer function considered by JAVELIN for samplings based on the DES/OzDES sampling rate, a sampling with 10 times the number of samplings expected for DES/OzDES spread evenly throughout the the survey lengths, and one with the same same kind of good sampling rate, but with the half year long seasonal gaps of DES/OzDES. The histograms are normalised such that the total areas under the curves equal to unity, and they are close to proportionally related to the final estimate of the values. A higher sampling rate of a light curve allows for better constraints of all parameters, and decreases the aliasing for the time lag recovery.